LBL-37822
UC-400

Lawrence Berkeley Laboratory
UNIVERSITY OF CALIFORNIA

EARTH SCIENCES DIVISION

Characterization and Application of Microearthquake Clusters to Problems of Scaling, Fault Zone Dynamics, and Seismic Monitoring at Parkfield, California

R.M. Nadeau
(Ph.D. Thesis)

October 1995

Prepared for the U.S. Department of Energy under Contract Number DE-AC03-76SF00098

DISCLAIMER

LBL-37822
UC-400

Characterization and Application of Microearthquake Clusters to Problems of Scaling, Fault Zone Dynamics, and Seismic Monitoring at Parkfield, California

Robert Michael Nadeau

(Ph.D. Thesis)

Department of Geology and Geophysics
University of California

and

Earth Sciences Division
Lawrence Berkeley National Laboratory
University of California
Berkeley, CA 94720

October 1995

This work was supported by the U.S. Department of the Interior, U.S. Geological Survey, under NEHRP award 14-08-0001-G2160, through the Director, Office of Energy Research, Office of Basic Energy Sciences, of the U.S. Department of Energy under contract No. DE-AC03-76SF00098, and by Associated Western Universities Incorporated grant No. DE-F607-93ER75912, U.S. Department of Energy, Office of Science Education Program, Laboratory Cooperative, Laboratory Graduate Fellowship. Data processing was done at the Center for Computational Seismology at LBNL, which is operated by the University of California for the U.S. Department of Energy under contract No. DE-AC03-76SF00098.

Characterization and Application of Microearthquake Clusters to Problems of Scaling, Fault Zone Dynamics, and Seismic Monitoring at Parkfield, California

by

Robert Michael Nadeau

B.A. (Gustavus Adolphus College) 1984
B.S. (University of Minnesota - Twin Cities) 1989

A dissertation submitted in partial satisfaction of the

requirements for the degree of

Doctor of Philosophy

in

Geophysics

in the

GRADUATE DIVISION

of the

UNIVERSITY of CALIFORNIA at BERKELEY

Committee in charge:

Professor Thomas V. McEvilly, Chair
Professor Lane R. Johnson
Professor Richard C. Aster
Professor Neville G. W. Cook

1995

Characterization and Application of Microearthquake Clusters to Problems of Scaling, Fault Zone Dynamics, and Seismic Monitoring at Parkfield, California

by

Robert Michael Nadeau

Abstract

Characterization and Application of Microearthquake Clusters to Problems of Scaling, Fault Zone Dynamics, and Seismic Monitoring at Parkfield, California

by

Robert Michael Nadeau

Doctor of Philosophy in Geophysics

University of California at Berkeley

Professor Thomas V. McEvilly, Chair

Analyses of seismograms from the High Resolution Seismographic Network at Parkfield, California provide new observations of microearthquake behavior, with implications for fault-zone dynamics. Most microseismicity is localized at some 300 sites (clusters) having about 20m dimensions, and which cumulatively occupy less than 1% of the seismogenic zone. Recurrence intervals, t, between events in clusters distribute bimodally with a short interval mode peaked at less than 2 minutes falling off as 1/t, and a lognormal mode distributed about $t \cong 0.8$ years. Groups of unique event-types within clusters -- subclusters -- are characteristic and follow the lognormal distribution. Events in clusters but belonging to different subclusters occur sympathetically, and their separations in occurrence time are short and follow the 1/t decay mode. Subclusters can be used as repeating sources for monitoring changes in wave-propagation with a resolution and spatial-temporal coverage previously unattainable. No significant systematic changes in coda Q or velocity anisotropy are observed, although travel-time delays of 1-2ms were detected locally in

response to the Oct. 1992 M4.6+ event. Clusters also provide a means for monitoring change in fault-zone process, through their spatio-temporal patterns of occurrence. Variations seen imply local changes in slip rates of about 10-20%. In clusters, characteristic recurrence and 1/t decay behavior mimics foreshock, aftershock and characteristic behavior of large event sequences, and scales with mainshock moment, suggesting similar physics for recurring microearthquake and large event sequences. Hence, occurrence of large events might be better understood through modeling using numerous small earthquakes with short recurrence-times. Assuming balanced cumulative seismic slip and strain loading, microearthquake source parameters of area, stress drop, and slip can be estimated. Comparison of these to estimates for large events leads to an unconventional interpretation of the physics of earthquakes -- size-dependent stress drops -- that explain puzzling observations of microearthquakes such as unusually high source corner frequencies, near collocation of adjacent rupture, and anomalously long recurrence intervals. It suggests that neither L nor W scaling are correct, and that frequency-size statistics are sensitive to catalogue duration, and non-stationary effects.

To Oblivion

Table of Contents

Acknowledgments

This thesis would not have been possible without the encouragement and assistance of the many concerned and dedicated people who make up the U. C. Berkeley community. I would also like to thank in particular Rose Mota and my brother Jim -- the former for the support and distraction this obsessive author needed to maintain his sanity, and the later for his camaraderie through our "Wilderness Years" together and for guiding me on my way back into Science.

Bill Foxall, Alberto Michelini, and Rick Aster deserve my gratitude for putting me onto microearthquakes -- a path of discovery which is proving to be more stimulating with each passing day. My thanks also to Dr. Lane Johnson and Dr. Bruce Bolt for their patience in and dedication to teaching a corn-fed midwesterner what earthquakes are all about. I am especially indebted to Dr. Thomas McEvilly for providing me with one of the worlds premier microearthquake data sets and the tools and stimulating scientific environment to do first class research with it.

My appreciation also to John Peterson, Roland Gritto, Valerie Korneev, Mike Antolik, Eleni Karageorgi, Ann Kirkpatrick, Arturo Romero, Don Vasco, Rich Clymer, Joel Ita, David Okaya, Ivan Psencick, Don Lippert, Ken Williams, Nick Gregor, Ann Becker, Bob Urhammer and Rick McKenzie and others for their help over the years and for the many free-wheeling and insightful discussions we've had.

Uncertain times brings people together who might otherwise have been only casual acquaintances, perhaps for this reason I feel a special closeness and gratitude to Pat Bronnenberg, Eleni Karageorgi, Mike Antolik and Teresa Williams for their empathy and assistance in getting me through a particularly troublesome period of my graduate experience.

I would also like to express my deep appreciation to the university ombudspersons, Kathleen Dickson and Dr. Angelakos for their sage advice and for giving me the courage and vision to finish my Ph. D. against what appeared to be overwhelming odds.

Finally, (and this is no joke!) I must thank Lawrence Revere (deceased) for his book "Playing Blackjack as a Business" and Nevada's Gambling establishment for providing me a cool $4200.00 (at $5 a crack). My modest success at gambling was the wreckage I so desperately clung to while my good ship "future in geophysics" seemed to be going down with all hands. The existence of this dissertation is testament of my rescue by many of those mentioned above.

This work was supported by the U.S. Department of the Interior, U.S. Geological Survey, under NEHRP award 14-08-0001-G2160, through the Director, Office of Energy Research, Office of Basic Energy Sciences, of the U.S. Department of Energy under contract No. DE-AC0376SF0098, and by Associated Western Universities Incorporated grant No. DE-F607-93ER75912, U.S. Department of Energy, Office of Science Education Program, Laboratory Cooperative, Laboratory Graduate Fellowship.

VITA: ROBERT M. NADEAU

CURRENT POSITION

Graduate Student Research Assistant, University of California - Berkeley and Lawrence Berkeley Laboratory, Berkeley, CA 94720 Phone: (510)-486-7312.

EDUCATION

Ph. D. Geophysics, University of California - Berkeley, 1995.

B.S. with High Distinction, Geophysics, University of Minnesota 1989.

PROFESSIONAL EXPERIENCE

Graduate Student Research Assistant, University of California - Berkeley and Lawrence Berkeley Laboratory, 1989 - 1995.

Geo-Materials Testing Technician, Twin Cities Testing, Minneapolis, Minnesota, 1988-1989.

HONORS

Associated Western Universities - DOE Laboratory Graduate Fellowship, 1991-1994.

Newhouse Fund Fellowship, 1990-1991.

W.A. Tarr Award in Earth Sciences, 1989.

Secretary, Nu Chapter, Sigma Gamma Epsilon Honorary Society for the Earth Sciences 1988-89.

AFFILIATIONS

American Geophysical Union

Seismological Society of America

RESEARCH INTERESTS

Micro-Earthquake Seismology.
Mechanics of Earthquake Faulting.
Earthquake Scaling.
Earthquake Hazards and Prediction.
Seismic Anisotropy.
Seismicity and propagation Monitoring with Micro-Earthquake Sources.

RECENT PUBLICATIONS

Nadeau, R. M., Characterization and Application of Microearthquake Clusters to Problems of Scaling, Fault Zone Dynamics, and Seismic Monitoring at Parkfield, California, Ph.D. dissertation, Univ. Calif., Berkeley, 1995.

Nadeau, R. M., Foxall, W., McEvilly, T.V., Clustering and Periodic Recurrence of Microearthquakes on the San Andreas Fault at Parkfield, California. Science, 267, 503-507, 1995.

Nadeau, R. M., Antolik, M., Johnson, P. A., Foxall, W., McEvilly, T.V., Seismological Studies at Parkfield III: Microearthquake Clusters in the Study of Fault-Zone Dynamics. Bull. Seismol. Soc. Am., 84,247-263, 1994

Antolik, M., Nadeau, R. M., Aster, R. C., McEvilly, T. V., Differential Analysis of Coda Q Using Similar Microearthquakes in Seismic Gaps Part 2: Application to Seismograms Recorded by the Parkfield High Resolution Seismic Network. Bull. Seismol. Soc. Am., in press, 1995.

CONFERENCE PAPERS

Nadeau, R. M., Characteristic Recurrence and Triggering of Microearthquakes at Parkfield, CA, submitted to the 1995 Fall Meeting of the American Geophysical Union, San Francisco, California, 1995.

Nadeau, R. M., Karageorgi, E., McEvilly, T. V., Complementing Vibroseis With Microearthquake Clusters for Monitoring Temporal Change at Parkfield, California, Int. Union Geod. and Geophys. XXI General Assembly, Boulder Colorado, A388, 1995.

Nadeau, R. M., and McEvilly, T. V., Recurrence Scaling From Large Characteristic Earthquakes To Parkfield Microearthquakes, Seismol. Res. Let., 66, No. 2, p.40, 1995.

Nadeau, R. M., Foxall, W., and McEvilly, T. V., Periodic Recurrence and Spatial Clustering in Characteristic Microearthquakes on the San Andreas Fault., Eos, Trans. Am. Geophys. Union Sup., 75, 469, 1994.

Aster, R. C., Antolik, M., Nadeau, R. M., McEvilly, T. V., Differential Analysis of Coda Q Using Similar Microearthquakes in Seismic Gaps, Eos, Trans. Am. Geophys. Union Sup., 75, 454, 1994.

Nadeau, R. M., Karageorgi, E. D. and McEvilly, T. V., Fault-Zone Monitoring with repeating Similar Microearthquakes: A search for the Vibroseis Anomaly at Parkfield, Seismol. Res. Let., 65, 69, 1994.

Aster, R. C., Antolik, M., Slad, G., Nadeau, R. M., and McEvilly, T. V., Quantitative Estimation of Coda Stability in the Anza and Parkfield Seismic Gaps, Seismol. Res. Let., 65, 35, 1994.

Nadeau, R. M., McEvilly, T. V., Foxall, W., Microearthquake Clustering and the Slip Process on the San Andreas Fault at Parkfield California, Chapman Conference on Hydrogeologic Processes: Lincoln, New Hampshire, June 6-9, 1994.

Nadeau, R., Foxall, W., and McEvilly, T. V., Comprehensive Characterization, Redefinition, and Preliminary Analyses of the 1987-1992 Parkfield HRSN Similar Event Clusters, Eos, Trans. Am. Geophys. Union Sup., 74, 416, 1993.

Aster, R. C., Nadeau, R. M., Antolik, M., Slad, G., and McEvilly, T. V., Coda Stability Analysis of Similar Earthquakes in Seismic Gaps. Eos, Trans. Am. Geophys. Union Sup., 74, 397, 1993.

Nadeau, R. M., A Search for Evidence of Large Scale Fault Aligned Seismic Anisotropy at the Parkfield HRSN: Implications for Anisotropic Permeability Structures, Fault Zone Weakness, and Temporal Stability Studies, Seismol. Res. Let., 64, 54, 1993.

Nadeau, R., and McEvilly, T. V., An Assessment of Temporal Changes in P- and S- Coda Polarizations at Parkfield Using Microearthquake Sources, Eos, Trans. Am. Geophys. Union Sup., 73, 397, 1992.

Nadeau, R. M. Antolik, M. and McEvilly, T. V., A Search for Temporal Changes in Travel Times and Polarization at Parkfield Using Earthquake Sources, Seismol. Res. Let., 63, 62, 1992.

Nadeau, R. M., Aster, R. C., McEvilly, T. V., Analysis of P and S Wave Polarizations at the Parkfield High-Resolution Seismic Network (HRSN), Eos, Trans. Am. Geophys. Union Sup., 72, 483, 1991.

Karageorgi, E., Nadeau, R. M., McEvilly, T. V., and Okaya, D., A Search for Mylonite Signature in the Multi-component/Multi-source CALCRUST Whipple Mountain Reflection Line, Eos, Trans. Am. Geophys. Union Sup., 71, 1612, 1990.

CHAPTER I

INTRODUCTION

Understanding the process of nucleation of fatal and damaging earthquakes is important both for society and as a matter of scientific interest. Observations of precursory phenomena for large and moderate sized events have been widely reported, though the observations are inconsistent and the physical processes responsible for them remain largely a mystery (1). The mechanics of these phenomena are of particular interest to investigators involved in earthquake prediction research and hazard analysis. Specifically, are the changes in physical observables during the nucleation phase of damaging earthquakes chaotic or time- and slip-predictable? In a practical sense, the truth seems to lie somewhere between the two extremes, so that researchers have focused their efforts at determining whether the aspects of time- and slip-predictability are systematic enough and can be formulated in such a way as to make them useful for the reduction of earthquake hazards.

To advance our knowledge of the nucleation process, the National Earthquake Hazards Reduction Program (NEHRP) has supported a multiplicity of programs designed to investigate various aspects of earthquake nucleation and to develop and apply models for assessing earthquake hazards. The operation of the High Resolution Seismic Network (HRSN) at Parkfield, California, and the collection and analysis of its recordings represents one such program and is part of the U.S. Geological Survey initiative known as the Parkfield Prediction Experiment

(2).

The work presented in this dissertation focuses specifically on a rather fortuitous and previously unknown feature of the microseismicity recorded on the HRSN -- the spatial clustering of nearly two-thirds of the total microseismicity into < 1% of the active fault surface. The HRSN records exceptionally high quality data owing to its low-noise borehole sensors, its very broadband recordings (0-125 Hz), and its set of closely spaced stations. These features in conjunction with a previously determined 3 dimensional P and S velocity model (3), a location catalogue, the virtual isolation of the Parkfield fault segment, and the pervasive clustering about the Parkfield asperity (4) provide an unprecedented opportunity to use high-resolution techniques in the study of important issues facing the seismological and fault mechanics communities. These issues include: 1) the mechanics of the nucleation process; 2) scaling relationships between laboratory results, microearthquakes, and large damaging earthquakes; 3) 'In situ' testing and refinement of existing models of fault mechanics and earthquake recurrence on a collapsed time scale and 4) the potential of clustered microearthquakes for helping detect changes in seismic wave propagation, microseismicity patterns, and clustering behavior -- all proposed indicators of accumulating stress premonitory to the expected magnitude 6 event at Parkfield (2, 3).

In this dissertation I undertake to describe and quantify the microearthquake clustering process at Parkfield and to demonstrate the usefulness of microearthquake clusters for addressing the issues mentioned above. Chapter II serves as an expanded introduction to this

endeavor. It provides an historical background and significance of the Parkfield Prediction Experiment and the role that microearthquake studies play in it. The chapter provides a detailed description of the high resolution seismic network and an introduction to the seismicity at Parkfield. It also summarizes the velocity models (3), and investigates, with a limited data set, the three main topics of the dissertation -- a characterization of the clustering phenomena at Parkfield, an investigation into the scaling and mechanics of earthquakes and the use of repeating microearthquake sources for monitoring various physical conditions in the fault zone.

Chapters III - V explore these main topics in greater detail and using higher resolution techniques. For example, in chapter III a rigorous characterization of earthquake similarity and clustering is presented and, with a refined algorithm for high precision relative locations, leads to the recognition of the sub-clustering phenomena and its associated patterns in spatial organization, earthquake triggering, size uniformity and quasi-periodic recurrence. The systematics in size and recurrence are strongly suggestive of characteristically repeating earthquakes (3, 5), though this issue is still in contention, a fact which is illustrated in the appendix following the chapter.

Recognition of systematic time dependent features in the microseismicity has opened the door to many potential applications of the clusters for studying earthquake scaling, mechanics and hazards. Chapter IV illustrates this by deriving a tentative moment-recurrence scaling relationship between repeating characteristic microearthquakes and large

repeating strike-slip events along the San Andreas Fault system in California. The implications of this relationship for source and fault mechanics and for earthquake prediction models are unconventional and potentially very significant. Furthermore, recent work relating recurrence intervals of mainshocks to foreshock and aftershock seismicity rates and size distributions (7, 8) suggests a way of scaling the entire ensemble of mainshock-related events.

Chapter V is an exposition of the considerable monitoring potential of microearthquake clusters. The borehole recordings and extreme coherency between temporally separated and repeating microearthquakes provide illumination sources which put the tightest constraints yet on detection of temporal change in various aspects of seismic wave propagation -- travel time, polarization, attenuation, and frequency content. In addition, the parameters of earthquake prediction, as applied to the characteristic microearthquake sequences, provide convenient measures of temporal change in recurrence and occurrence patterns of inter- and intra- cluster seismicity. These parameters appear to show more sensitivity to localized change in the nucleation region than either wave propagation characteristics or traditional patterns of seismicity, and are particularly attractive since they can be readily interpreted in terms of seismic moment and local average slip rate.

I include in chapter V a discussion on the mistaken practice, commonly used by investigators of temporal change, of regarding the scatter of measurements from events with small time separations as unbiased error bounds on the variability of time-independent wave propagation. I

illustrate the significance of this in the context of a travel time stability study and a differential coda Q study (9). I finish the chapter by reporting on the results of studies of travel time, polarization, attenuation, and cluster recurrence and occurrence patterns in the vicinity of the Parkfield asperity.

Chapter VI is the last chapter of the dissertation and in it I summarize the thesis and draw conclusions. The conclusions inevitably point to the need for further study and refinement, but in particular they emphasize the important role characteristic microearthquakes are likely to play in expanding our knowledge of fault zone dynamics and the earthquake nucleation process.

REFERENCES

1. T. Rikitake, Current Research in Earthquake Prediction. 1,1 (1981); M. Wyss, ibid. 1,81 (1981); S. Crampin, R. Evans, B. K. Atkinson, Geophys. J. R. astr. Soc. 76, 147 (1984).

2. W. H. Bakun, and A.G. Lindh, Earthq. Predict. Res., 3, 285 (1985).

3. A. Michelini and T.V. McEvilly, Bull. Seism. Soc. Am. 81, 524 (1991).

4. R. M. Nadeau, W. Foxall, T. V. McEvilly, Science, 267, 503 (1995).

5. W. H. Bakun, and T.V. McEvilly, J. Geophys. Res. 89, 3051 (1984).

6. D. P. Schwartz and K. J. Coppersmith, ibid. 89, 5681 (1984).

7. J. Dieterich, J. Geophys. Res. 99, 2601 (1994).

8. P. A. Reasenberg and L. M. Jones, Science 243, 1173 (1989); L. M. Jones, Bull. Seismol. Soc. Am. 87, 892 (1994); L. Jones and P. Molnar, J. Geophys. Res. 84, 3596 (1979).

9. M. Antolik, R. M. Nadeau, R. C. Aster, T. V. McEvilly, Bull. Seism. Soc. Am., in press, 1995.

CHAPTER II

Seismological Studies at Parkfield III: Microearthquake Clusters in the Study of Fault-Zone Dynamics

(R. Nadeau, M. Antolik, P. Johnson, W. Foxall,
and T. V. McEvilly, 1994, with modifications)

ABSTRACT

More than half of the microearthquakes that occur near Parkfield, California are seen, when located with high-resolution methods, to define some 80 small clusters of 2-12 similar events. Each cluster occupies a patch typically 100-200 m in length within the fault zone. Cluster members have nearly identical waveforms (correlation coefficient of 0.9 or greater) to frequencies of 50 to 100 Hz, as recorded by the HRSN. The clusters are distributed throughout the fault zone around the presumed nucleation region, in the locked section to the SE and in the creeping part to the NW of the previous M6 hypocenters. They are also found in the Salinian block several km SW of the fault zone. The total area occupied by all of the clusters constitutes only a small fraction (<1%) of the fault zone approaching failure at Parkfield. Such clusters provide insight into the dynamics of the failure process through their spatial-temporal characteristics and their mechanisms. They also serve as highly repetitive sources distributed throughout the fault zone suitable for monitoring the nucleation zone for possible precursory changes in physical properties that affect wave propagation. In this study we have demonstrated these

applications with a detailed analysis of selected clusters. In the following chapter, we more rigorously define the geometry of clusters and the nature of subclusters.

INTRODUCTION

On the San Andreas fault near Parkfield, in central California, earthquakes of magnitude around 6 appear to occur with a periodicity of about 22 years (1). It is widely presumed that changes in elastic parameters of crustal rocks may be observable within the nucleation zone prior to an earthquake, in response to the stress buildup and resulting perturbations in fractures and fluid behavior. Far less agreement exists on the expected size of the nucleation zone - a question of utmost importance in earthquake prediction research. Early studies reported very large and spatially extensive changes in the velocity of seismic waves prior to earthquakes over a wide range of magnitudes (2), but these results were not confirmed in central California in more precise later studies (3). In the 1980s the U.S. Geological Survey initiated the Parkfield Prediction Experiment in an effort to monitor those parameters most likely to be influenced by the failure process prior to the expected earthquake there and to obtain a detailed picture of the dynamic process of fault-zone failure (4).

As part of the intensive instrumentation program required for this experiment, the HRSN was installed around the presumed Parkfield nucleation zone in 1986-87 (Fig. 2.1). Data from this network are unique

in their high-frequency content (to 125 Hz) and sensitivity (down to events of magnitude around -0.5). The data have provided a sharpened perspective on the patterns in seismicity relative to the rupture zone of previous M6 earthquakes at Parkfield (5, 6, 7). The closely-spaced stations yield evidence for elastic waves confined to propagation in the low-velocity fault-zone waveguide. (8). These data have also allowed the determination of detailed three-dimensional P and S wave velocity models which reveal a high degree of spatial variability in fault-zone properties. Such models incorporate velocity heterogeneity directly into the hypocenter location process, avoiding the necessity of site-specific station adjustments to arrival times, and provide very high accuracy estimates of the relative positions of neighboring hypocenters (9).

In the first six years of operation (1987-1992) about 1600 micro-earthquakes were recorded and located in the central 25 km stretch of the fault containing the Middle Mountain nucleation zone. During the period 1987-1989, 329 of the 614 events that occurred, when located with high-resolution methods, defined some 80 clusters of from two to 12 events, each occupying a small region, apparently about 100-200 m in extent, within the fault zone (Fig. 2.1b), but under subsequent study it was found that this dimension was more like 20-40m (7). Year-to-year seismicity patterns during that period remained fairly stable (Fig. 2.2). For display convenience we use a fault zone-based coordinate system centered at the 1966 epicenter. The three-dimensional velocity structure and clustered seismicity provide a coupled view of the behavior of a fault segment approaching failure. The tightly-clustered microearthquakes allow

repeated sampling of rupture mechanisms (10) and of physical properties throughout the heterogeneous nucleation zone, thus providing an invaluable monitoring tool in the search for predictive precursory changes. The range of source size seen in a given cluster (from M -0.5 to M 4.0 or greater) also offers a unique opportunity to study scale effects in the seismic source over orders of magnitude and in a wide frequency band, without the ambiguities usually present in such comparative studies due to differing source media and propagation paths.

In this paper (6), we explore the clustering phenomenon at Parkfield and its implications for fault-zone investigations using a limited but illustrative data set. We first review the three-dimensional P and S wave velocity models that have been determined for the region, and describe the microseismicity and clustering at Parkfield. The high degree of similarity among waveforms of cluster members implies near co-locations, so we next illustrate the high-resolution waveform processing we apply to the cluster signals in order to achieve relative hypocenter location precision of a few 10's of meters. We proceed to explore the cluster phenomenon, focusing on the spatial distribution of clusters along the active fault zone and on the relationship of the clusters to the site of the expected M6 hypocenter, and to the NW-SE transition from creep to locked behavior along the San Andreas fault near Parkfield. We then examine a particular cluster and characterize it in terms of its spatial/temporal properties and its variability in source size. Finally, we demonstrate the monitoring potential in the repeating similar waveforms, analyzing events from a cluster which illuminates the 1966 hypocentral region, the presumed nucleation zone of

the expected earthquake. We use the broadband waveform similarity to search for changes over the 1987 - 1992 period of HRSN operation.

Fig. 2.1. The Parkfield study area. (a) Map showing seismographic stations of the borehole network, microearthquake seismicity for the period February 1987 - December 1992, the 1966 epicenter (open circle), and the trace of the San Andreas fault. (b) Locations of the approximately 80 earthquake clusters defined in the period February 1987 - December 1989. Labeled clusters are discussed in the text.

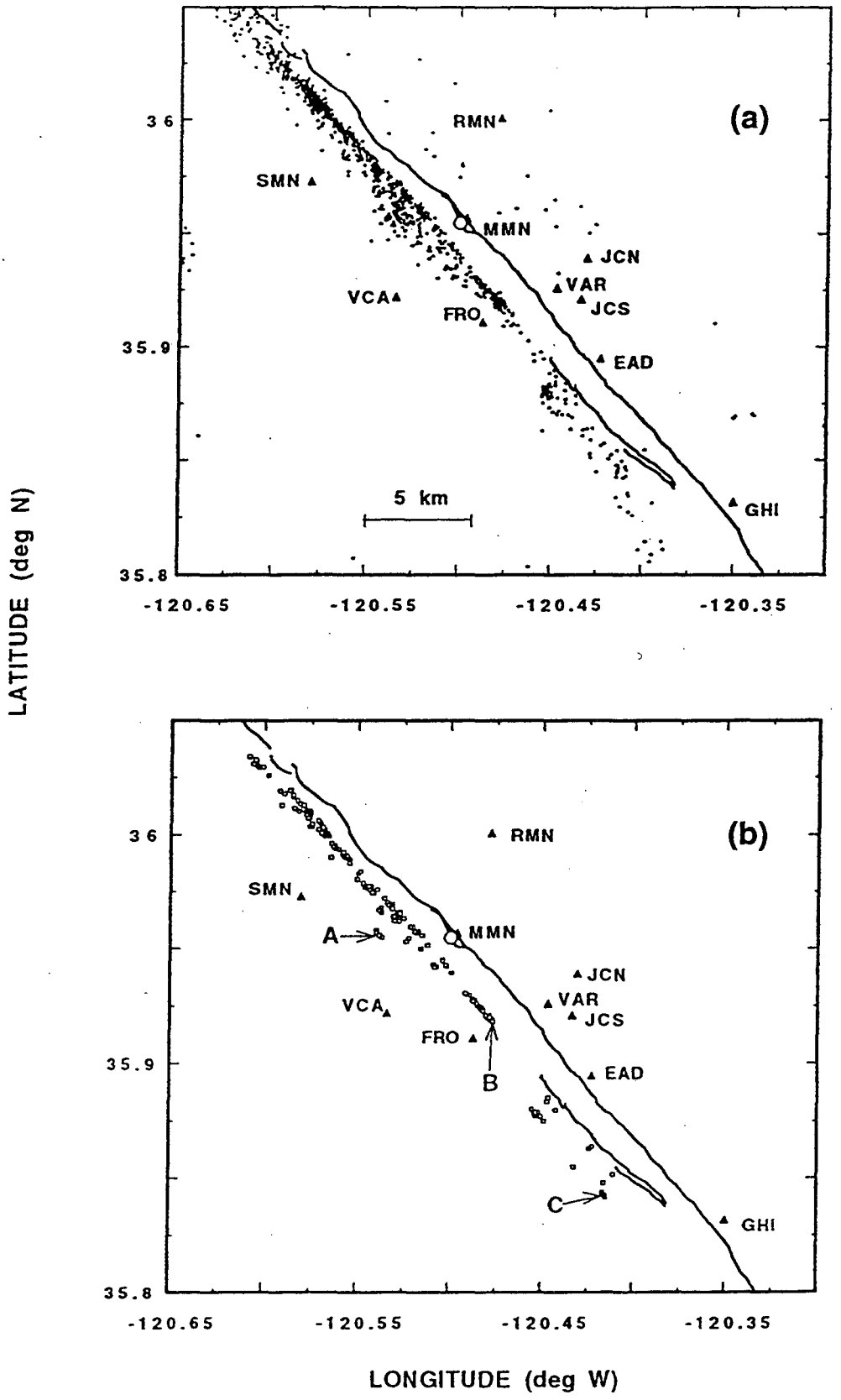
(a)
RMN
SMN
MMN
JCN
VAR
JCS
VCA
FRO
EAD
GHI
5 km
36
35.9
35.8
-120.65
-120.55
-120.45
-120.35
(b)
RMN
SMN
A
MMN
JCN
VAR
JCS
VCA
FRO
B
EAD
C
GHI
36
35.9
35.8
-120.65
-120.55
-120.45
-120.35
LATITUDE (deg N)
LONGITUDE (deg W)

Fig. 2.2. Strip maps of annual seismicity for the years 1987-92. The event labeled S (1991 panel) is discussed in the text. The 1966 epicenter and the town of Parkfield are shown. Note the year-to-year similarity in the pattern of seismicity. This figure shows the X-Y coordinate system used in subsequent presentations (x is fault-normal NE and y is along-strike NW, centered at the 1966 epicenter).

ANNUAL ACTIVITY PATTERNS

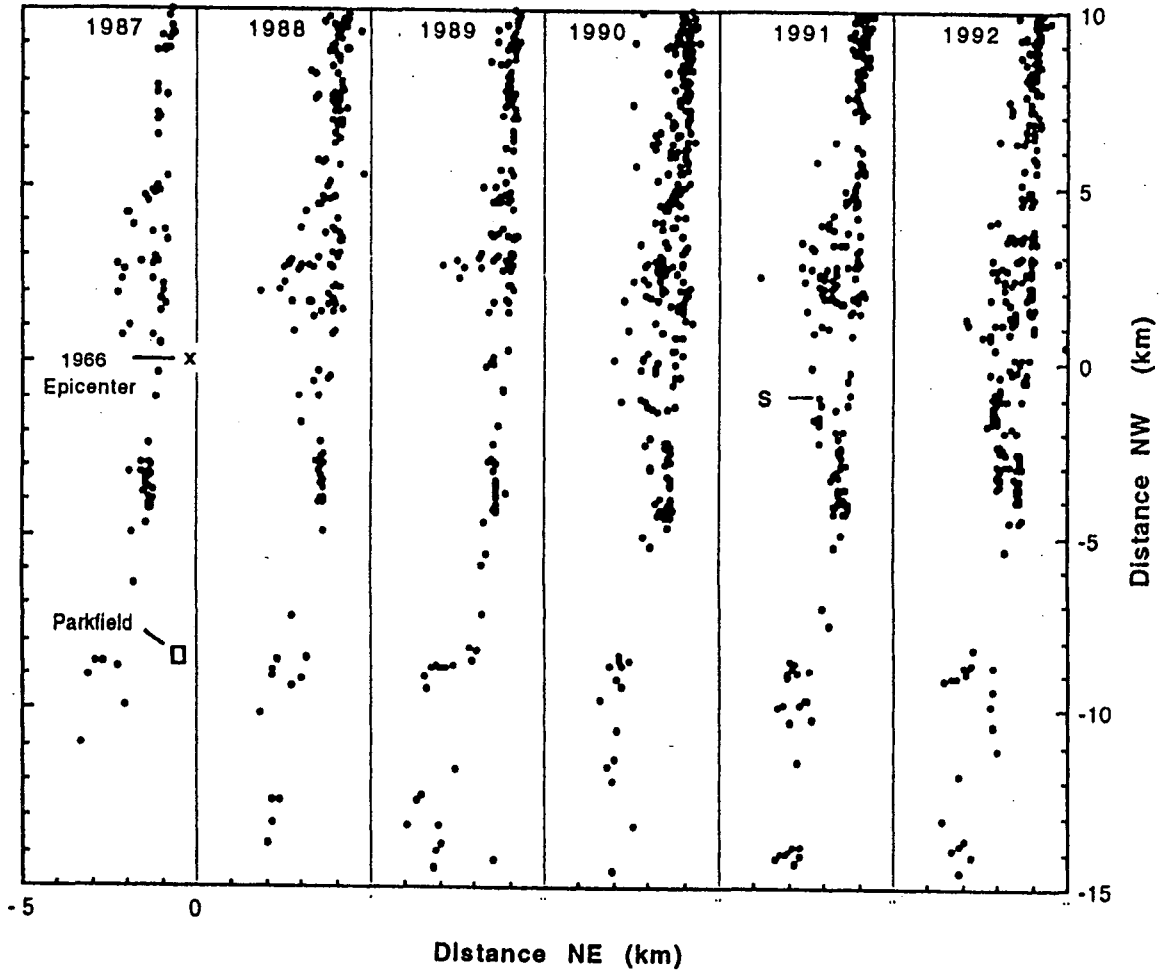

THREE-DIMENSIONAL VELOCITY MODEL AT PARKFIELD

Three-dimensional P-wave velocity models for Parkfield have been determined through joint inversion of CALNET data (11) and from HRSN data (assuming correct hypocenters) (12). CALNET P data with HRSN P and S arrival times has been used in a joint inversion for hypocenters and independent three-dimensional P and S velocity structures (9). Two salient features are clearly visible in the model, shown in cross sections in Fig. 2.3 and 2.4 First, a relatively high-velocity body for both P and S waves is present SW of the San Andreas fault in the region SE of the 1966 hypocenter and below 5 km depth. The P and S velocities (as great as 6.6 and 3.6 km/s, respectively) are probably too high for the granitic composition of the Salinian block. This high-velocity body may control the mode of deformation, the seismicity pattern and the extent of rupture in larger events; a role similar to that proposed for a deep high-velocity body at Loma Prieta (13, 14, 15).

The second notable feature in the 3-D model is a region of high V_P/V_S ratio (about 2.0), localized within the fault zone and extending from the 1966 mainshock focus southeastward about 3 km into the 1966 rupture zone. It is tempting to associate this feature with anomalous conditions related to the nucleation process of the M6 earthquake. Possible causes of the V_P/V_S anomaly involve high pore-fluid pressure or extreme shear-wave anisotropy in the deep fault zone. Dilatant fracturing (16), pore-fluid expansion due to frictional heating (17), or dehydration of clay minerals (18) in a low-permeability fault zone may contribute to the high V_P/V_S ratio,

especially in the complex environment of high stress and strain in the nucleation zone. It is also possible that severe anisotropy in the nucleation zone results in large delays in shear waves propagating through that region. The hypothesis of high pore pressure as the cause of reduced V_S and thus elevated V_P/V_S deep in the fault zone is compatible with the arguments of other researchers who call for high pore pressure (near the level of fault-normal compression) within a fault zone having greater permeability than the adjacent blocks, as an explanation of fault-zone absolute and relative weakness (19, 20). Anisotropic permeability, permitting flow in the plane of the fault but not normal to it, may characterize the deep fault zone. It has been presumed that a supply of fluids exists at the ductile roots of crustal fault zones, and suggested that fluid pressure surges also exist with velocities reaching 1 km/year. The presence of high pore pressure at depth in fault zones has been explained with a time-varying process whereby steadily decreasing permeability and porosity produce increasing pore pressure until spontaneous hydrofracturing occurs, dropping the pressure and beginning another cycle (21). Anomalous V_P/V_S within the deep fault zone may indicate permeability and porosity reduction by volumetric strain in the nucleation zone. This possibility makes the V_P/V_S anomaly a prime target in the monitoring program for premonitory change, using both clustered microearthquakes and the Vibroseis (22) as sources of P and S wave illumination.

Fig. 2.3. Fault-normal cross sections at y=0 (i.e., at the 1966 epicenter) showing the 3-dimensional model P and S velocities and the V_P/V_S ratio (9) with hypocenters for the central section of the fault zone shown in Fig. 2.5. The generally accepted 1966 hypocenter is shown as a red dot. Variations in color intensity correspond to the degree of resolution in the model.

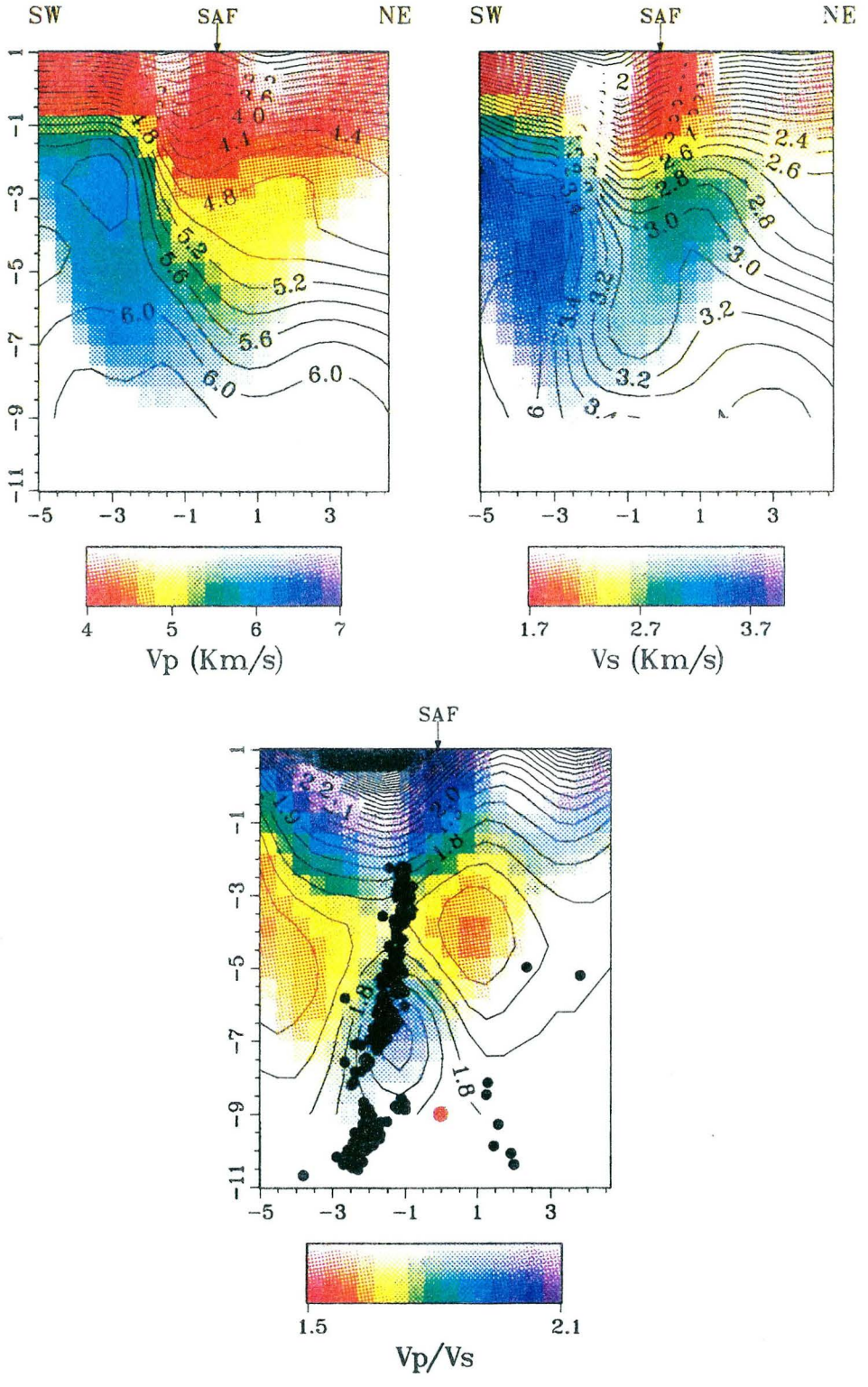
SW
SAF
NE
SW
SAF
NE
Vp (Km/s)
Vs (Km/s)
SAF
Vp/Vs

Fig. 2.4. Fault-parallel cross sections. (a) P velocity model. Scale is the same as in Fig. 2.3. (b) S velocity model. Scale is the same as in Fig. 2.3. (c) Seismicity 1987 - 1992 in fault-parallel section. Hypocenters in a 4-km wide band paralleling the fault are projected onto the plane. Clusters (1987-89) of events are shown as the large dots and those discussed in the text are shown as filled diamonds and labeled. Fault-normal sections for the three segments of the fault zone (south, central, north) are shown in Fig. 2.5. The 1966 hypocenter is the open diamond located at [y,z]=[0,9]

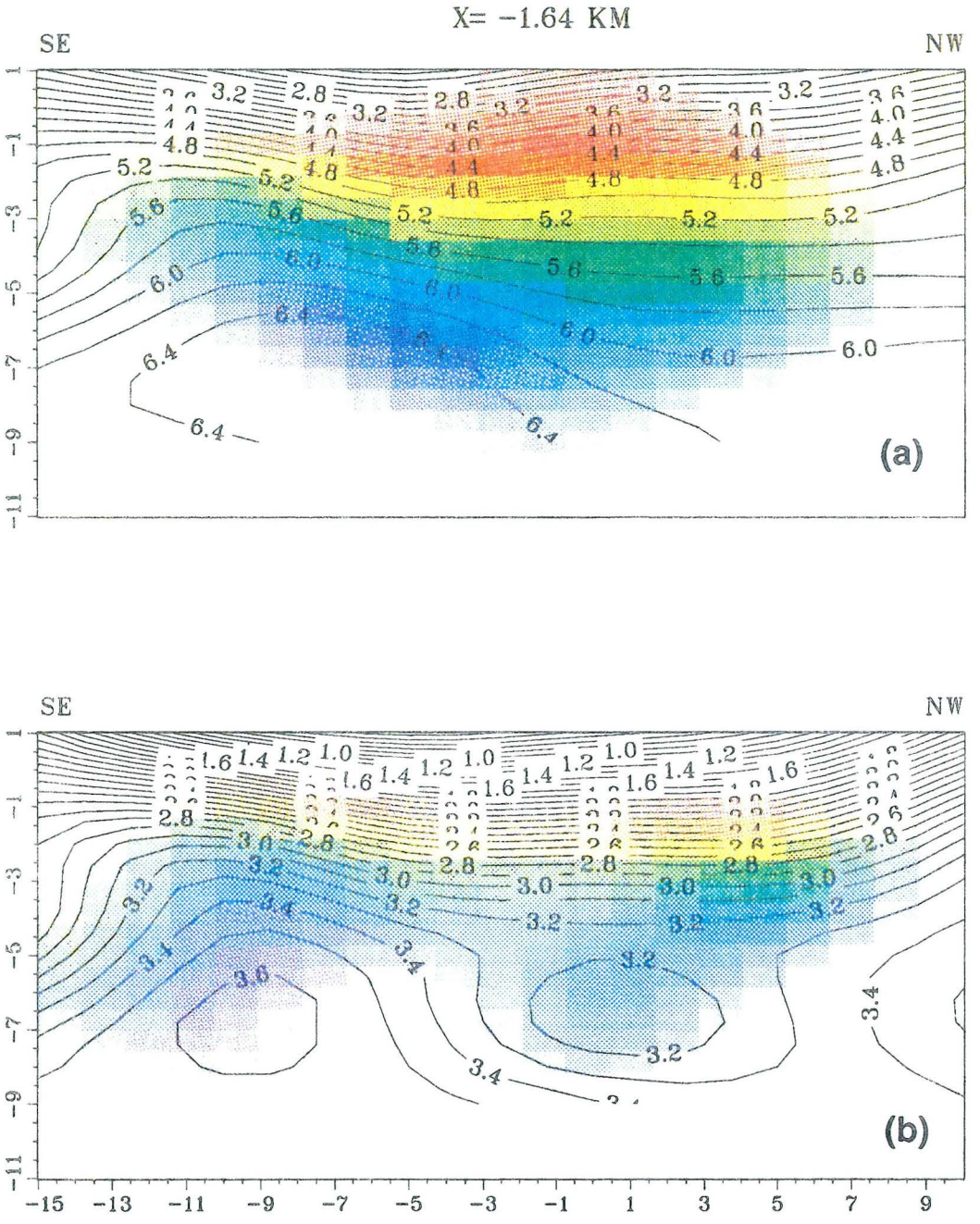
X= −1.64 KM
SE
NW
(a)
SE
NW
(b)
1
-1
-3
-5
-7
-9
-11
-15
-13
-11
-9
-7
-5
-3
-1
1
3
5
7
9

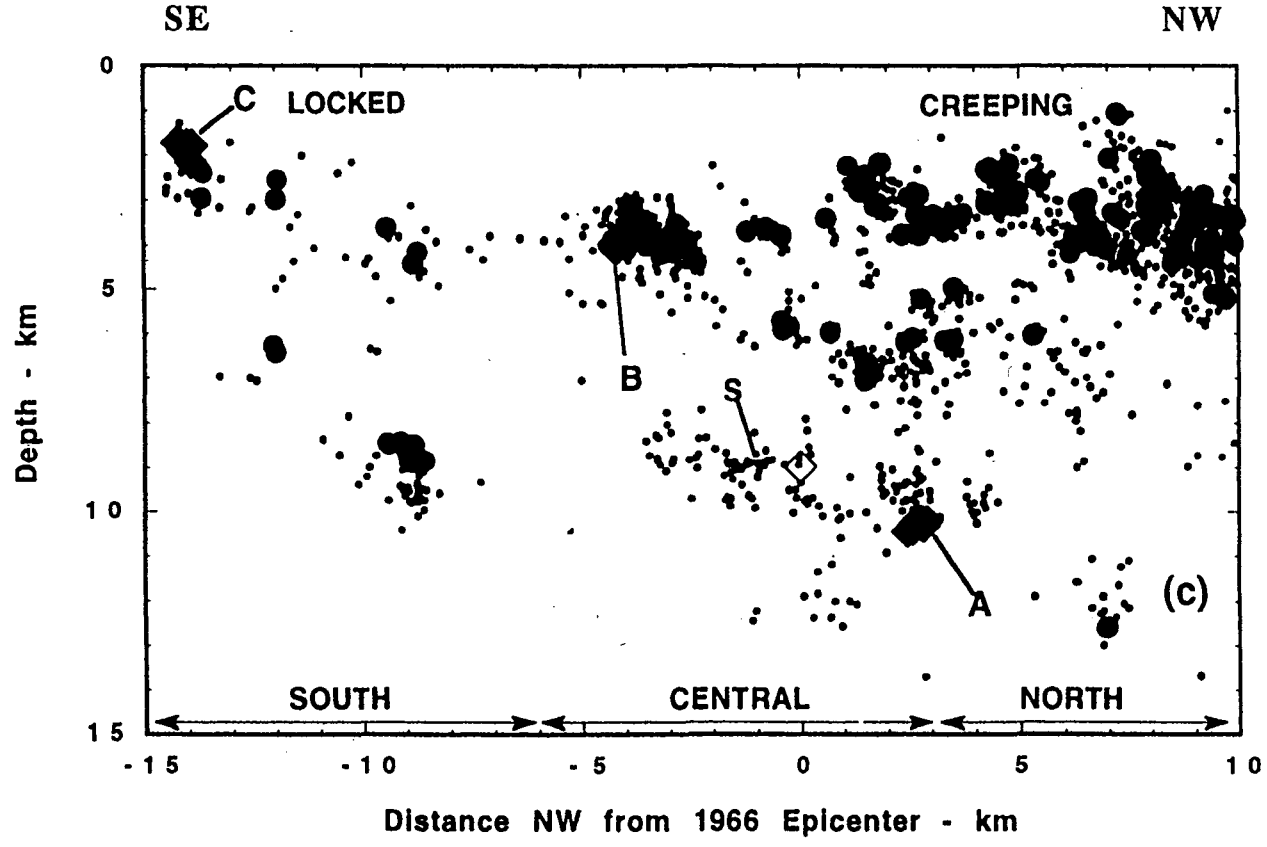
SE
NW
0
5
10
15
C
LOCKED
CREEPING
B
S
A
(c)
SOUTH
CENTRAL
NORTH
Depth - km
-15
-10
-5
0
5
10
Distance NW from 1966 Epicenter - km

SEISMICITY PATTERNS AND CLUSTERS

About 1600 microearthquakes (M -0.5 to M 3.5) detected by the HRSN from 1987 through 1992 were relocated with the 3-D velocity model and are presented in Fig. 2.1a. These hypocenter locations have rms. residuals <50 ms (typically around 20 ms) while generally using 10-12 P and S arrivals. Depths range from about 2 to 13 km. The distinctive variations in seismicity along the fault zone are illustrated in Fig. 2.5 with fault-normal cross sections of the three kinematically disparate segments of the fault at Parkfield defined in Fig. 2.4c (south - locked; central - transitional; north - creeping). The overall pattern of seismicity has been very stable from year to year (Fig. 2.2); the segments of activity, the relatively quiet 'gaps', and the areas of laterally diffuse seismicity have remained the same (to first order) throughout the 6-year period. The Parkfield stretch of the San Andreas fault includes the south-to-north transition from locked to creeping behavior, which spans the presumed M6 nucleation zone, shown as the central cross section in Fig. 2.5. The 1966 hypocenter lies on this section of the fault apparently within the aseismic patch evident at a depth of 8-9 km in Fig. 2.4c and 2.5. Along this central stretch of the fault at Parkfield the seismicity is more uniformly distributed throughout a depth range of 2 to 10 km than it is either to the north in the creeping section or to the south in the locked zone. Hypocenters in the locked zone that ruptured in 1966 occur mainly during the 1987 - 1992 interval studied in two depth ranges, 3 to 5 km and 8 to 10 km. In the creeping section, seismicity is abundant between 1 and 6 km depth, with scattered activity at depths around 7-8 km and 12-14 km.

An outstanding feature of the seismicity is the high degree of spatial clustering mentioned above. The total area occupied by the 80 small patches of clustered foci that include more than half of the earthquakes during the period is a small fraction (less than 1%) of the full fault zone area along this stretch. This fraction of earthquakes as cluster members seems very high. A formalism for organizing waveform pairs into clusters, using a minimum acceptable median cross-correlation coefficient as the measure of similarity has been presented (23). For the Anza network, a coefficient of 0.725 yielded 290 clusters containing 1255 events out of 4569 earthquakes, or 27% of the total. The criterion used to define the 80 clusters at Parkfield is approximately equivalent to a minimum coefficient of 0.90. If we apply this more stringent discriminant to the Anza data (Fig. 3 of (23)), only some 60 clusters containing about 120 events (less than 3% of the total seismicity) are defined. Microearthquake clustering is clearly more central to the process of slip accommodation at Parkfield than it is at Anza. It is interesting to speculate on the potential significance of this seismicity property in terms of its possible systematic change during the failure cycle of a fault segment.

It is not clear at present whether the cluster patches - where the fault zone is accommodating slip through earthquakes - represent 'pinned' strong asperities on the fault 'surface', with aseismic creep in the weak intervening regions, or whether they are points of weakness within a strong 'locked' fault zone. Cluster patches may reflect the fluid regime in the fault zone, perhaps representing localized very high pore fluid

pressure due to the geometry of the permeability distribution. There are indications that some clusters may represent *en echelon* tensional failure points along the fault zone (24), further suggesting the possible role of excess fluid pressure in hydrofracturing the fault zone locally.

Fig. 2.5. Fault-normal cross sections of seismicity at three locations along the strike of the San Andreas fault, as defined in Fig. 2.4c. (left) Southern cross section (locked zone). (center) Central cross section (transition area, including the 1966 hypocenter at about 9 km depth). (right) Northern cross section (creeping zone).

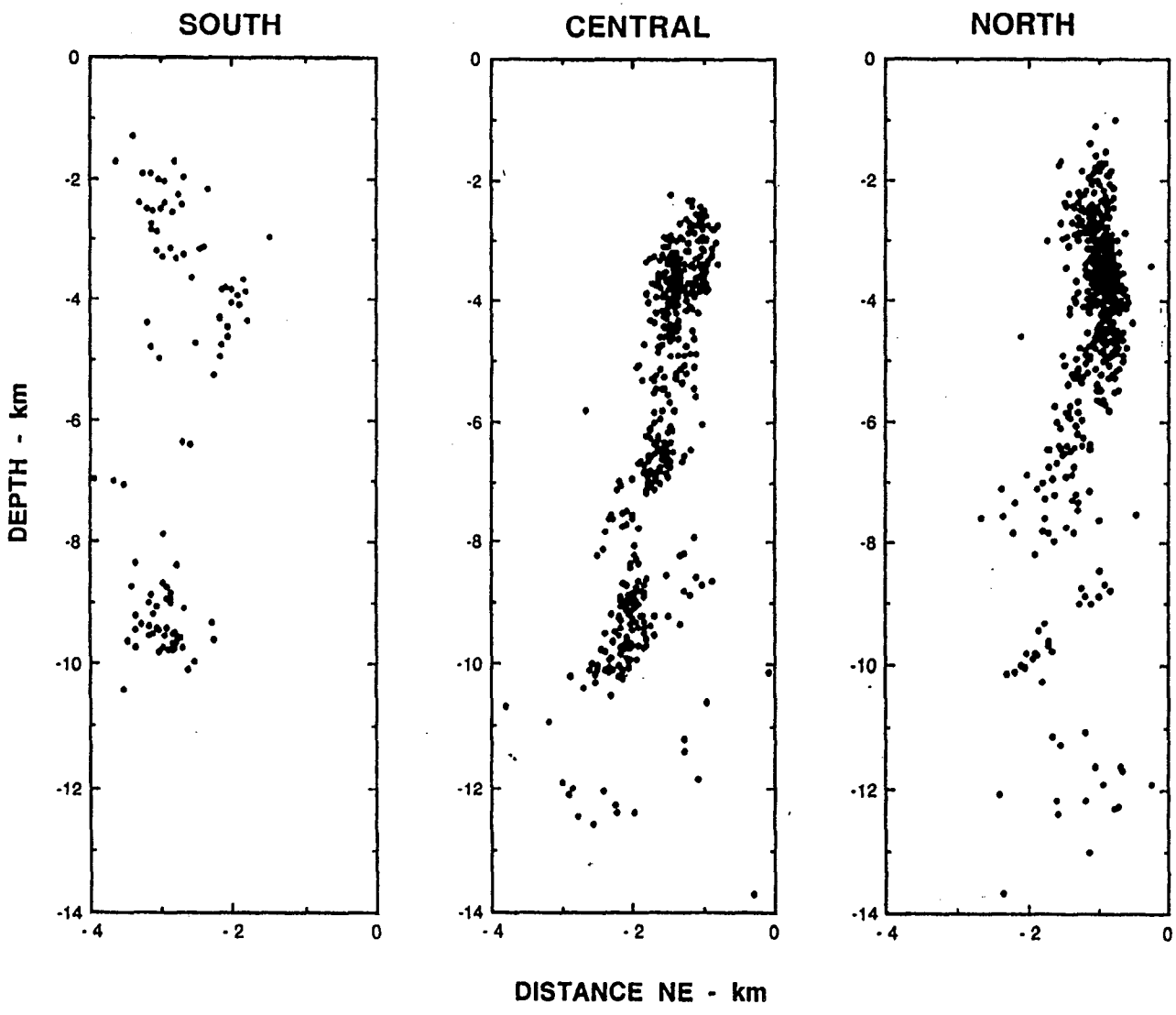
SOUTH
CENTRAL
NORTH
DEPTH - km
0
-2
-4
-6
-8
-10
-12
-14
-4
-2
0
DISTANCE NE - km

HIGH-RESOLUTION RELATIVE HYPOCENTER LOCATIONS

Precise estimates of the relative locations of earthquakes in the clusters are useful in investigating the mode of slip on the fault at Parkfield. The accuracy of hypocenter locations is in large part limited by analyst subjectivity, which leads to inconsistent timing of P and S phase arrivals among clustered events. To circumvent this problem, we determine the group delay from the phase of the cross-power spectrum between two coherent wavelets aligned in time. This method has been used in several earthquake studies (23, 25, 26, 27, 28). We select a reference event from each cluster. The cross-power spectrum of a window (typically of 0.1 s length) beginning at the P and S arrival times are then computed for each successive cluster member paired with the reference event. The window length is chosen with particular care to minimize the influence of multipath and coda arrivals. Due to the borehole depths P and S phases reflected at the free surface arrive at least 100 ms and 200 ms, respectively, after the direct waves. P and S delays relative to the reference event are computed from the slope of the phase of the coherence-weighted cross-power spectra, and the events within each cluster are then relocated relative to the conventional 3-D location of the reference event, using these relative arrival times of P and S phases. A summary of the method is shown in Fig. 2.6.

The high-resolution timing method appears, on the basis of both the formal uncertainty in the slope estimate and on tests with synthetic data, to define relative phase delays as small as ± 0.2 ms between similar traces (one-

tenth the sampling interval). This corresponds to about 1 m propagation distance, and, when combined with the random ±1 ms sample time uncertainty, can theoretically produce an accuracy of around 10 m in the relative hypocenter locations within a typical cluster (27). We guard against variable bias in the relative locations by limiting each cluster to a consistent station set in the relative location exercise.

The relative location procedure makes it possible to discern very detailed patterns present in the clustered seismicity that are not resolved with routine location procedures. Fig. 2.7 shows the separation of the members of one cluster group into two distinct sub-clusters occupying patches of about 100 m diameter after application of the high-resolution timing and relocation method. This separation is apparent in the waveform differences, but not in the original conventionally-determined epicenters shown in Fig. 2.7.

Each hypocenter estimated with the high-resolution method represents the best location of a source point for the entire windowed P and S waveforms. In other words, rather than locating the exact point of fracture initiation, the method yields some spot within the ultimate rupture surface for the source - probably that from which the radiated energy is maximum. Only if the source is truly a point relative to the timing resolution (~ 1 m diameter) and if also there is no strong scatterer near the source (close enough to add significant and azimuthally variable contaminating energy to the direct P or S wave windows used in the correlation) will the estimated hypocenter define the true rupture initiation point. Otherwise,

we are defining an average source point for the P and S wave energy in the 50-100 ms window used to determine the relative time delays. If off-fault scattered contributions are negligible but the source is finite (more than 2-3 m diameter, or having more than 1-2 ms rupture propagation time), the network (if it samples the radiation pattern roughly isotropically) will yield a source point somewhere on the rupture defining a combination of high radiated energy and some network-averaged centroid on the fault surface. If the 100 Hz corner frequencies that are seen for M=0.5-1.0 sources (see scaling section below) represent rupture propagation delays, those microearthquakes have fault dimensions of about 30 m.

Fig. 2.6. Summary of the cross-correlation/cross power spectrum technique for determining relative arrival times. (a) Similar P and S waveform pairs for two events in a cluster aligned by cross-correlation. P- and S windows used in the delay computations are shown. (b) The phase of the cross-power spectrum, the slope of which permits estimation of the relative times to a fraction of the sampling interval. (c) Coherency between the waveform pairs, indicating that the signal pairs are highly coherent to about 80 and 60 Hz for the P and S phases, respectively.

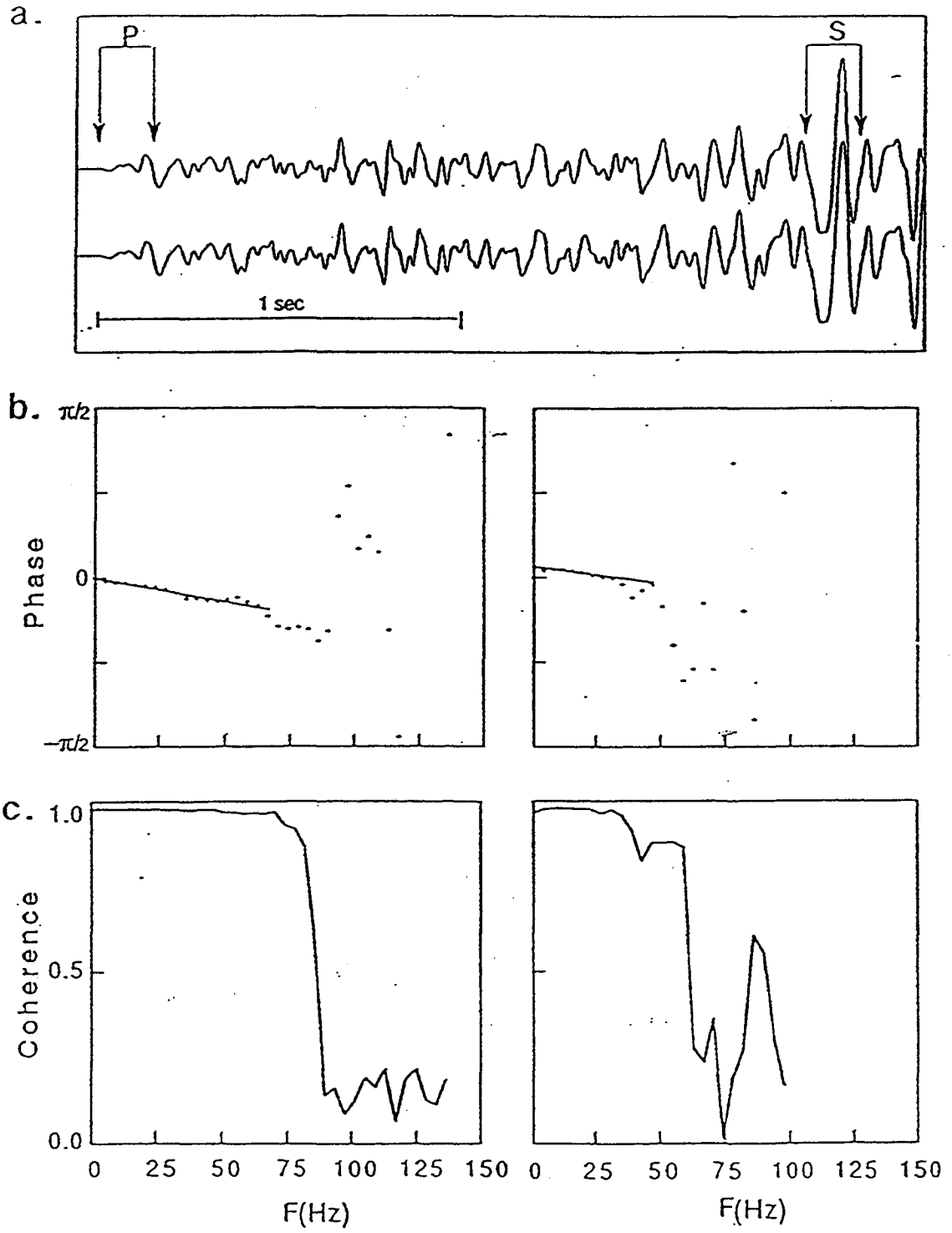
a.
P
S
1 sec
b.
π/2
Phase
0
−π/2
c.
1.0
Coherence
0.5
0.0
0 25 50 75 100 125 150
F(Hz)
0 25 50 75 100 125 150
F(Hz)

Fig. 2.7. Cluster event relocations. (a) Examples of similar waveforms among members of two clusters. Data are from station FRO for a group of events exhibiting two distinct waveforms, labeled 1 and 2.. Note the strong waveform similarities throughout both P and S coda arrivals. (b) Conventional (X's) and high-resolution (dots) locations based on the cross- spectra timing method applied to the events. The relative locations concentrate in two distinct spatial groups, each about 100 m across, substantially reducing the km-scale scatter in the conventional locations.

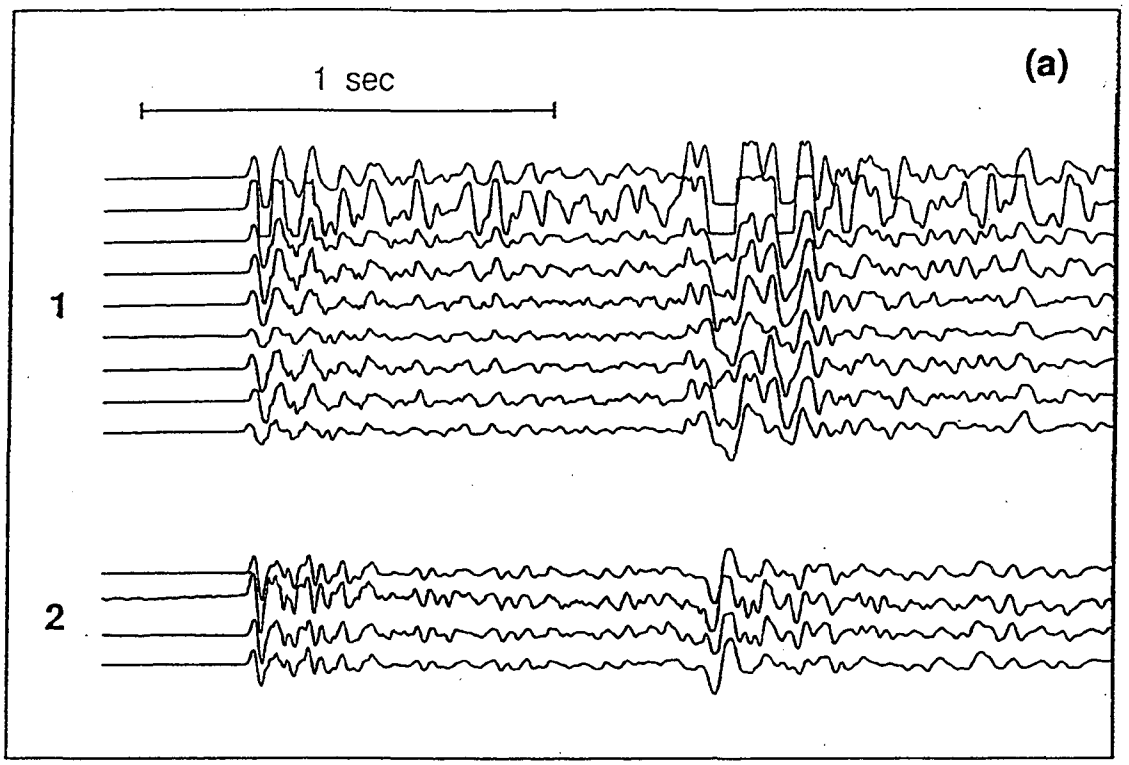
(a)
1 sec
1
2

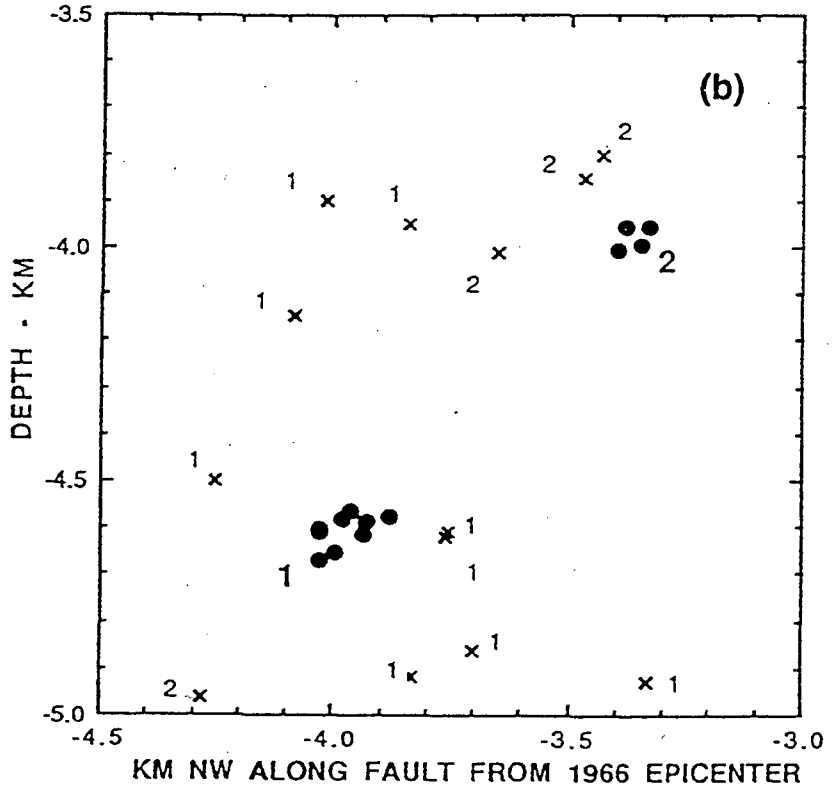
(b)
-3.5
-4.0
-4.5
-5.0
DEPTH - KM
-4.5
-4.0
-3.5
-3.0
KM NW ALONG FAULT FROM 1966 EPICENTER

CLUSTER DISTRIBUTION AND DIMENSIONS

The approximately 80 microearthquake clusters that occurred during the first three years of operation of the HRSN are shown in map view in Fig. 2.1b and in cross-sections in Fig. 2.4c and 2.5. The distribution of microearthquake clusters mimics the overall spatial pattern of background (non-clustered in this sample period) seismicity. This is true for the creeping zone to the NW as well as for the locked section to the SE. It is possible that, given the similar distributions of clusters and non-clustered events, in time all of the background events may become members of clusters. Although the exact definition of a cluster is somewhat arbitrary, we have opted for a tight definition which requires a high degree of similarity well into the S coda (see Fig. 2.6 and 2.7 for examples). This produces a set of clusters containing from two to 12 events, and a mean cluster size of 4.5 events through December 1989. Clusters occupy volumes with dimensions up to about 200 m. Some clusters having waveforms that are highly similar, however, divide further into subclusters, such as the groupings seen in Fig. 2.7 and 2.8. The smallest of these subclusters appear to be confined to a volume 50 m or less on a side. Further improvement of cluster locations has been possible and is illustrated in the next chapter.

We have observed great variability in both the temporal occurrence of events within a cluster and in the range of magnitudes represented. Some clusters consist of single events randomly spaced in time while others, such as Clusters B and C in Fig. 2.8, occurred entirely as bursts of activity

or as bursts of activity in combination with a number of single, isolated events. Cluster B (see Fig. 2.1b for location) occurred mainly as two bursts in September 1987 and August 1990 while Cluster C consists of one event in 1989 followed by a mainshock/aftershock sequence in April 1991. The full range of magnitudes detectable by the HRSN has been observed in clusters. The events of Cluster A (Fig. 2.1b) are distributed fairly uniformly in magnitude and are ideally suited to spectral scaling and source dimension studies. The mainshock in Cluster C (event #2 in Fig. 2.8) is nearly one magnitude unit larger than the other events of the cluster. The M4.7 shock in October 1992 occurred in a cluster containing members with M<0.

Some of the cluster patterns are suggestive of en-echelon lineations of hypocenters. Cluster B in Fig. 2.8, for example, appears to consist of two en-echelon strands about 50 m apart and about 100 m long and a third rather diffuse sub-cluster. Cluster C contains possibly two parallel en-echelon strands 50 m apart. In both of these clusters the orientation of the en-echelon strands is about 40 degrees clockwise from the N45W local strike of the San Andreas Fault. This geometry, while tenuous, is suggested in many of the clusters.

Fig. 2.8. Map views of the high-resolution locations for Clusters B and C. Dates are shown for the events of Cluster C.

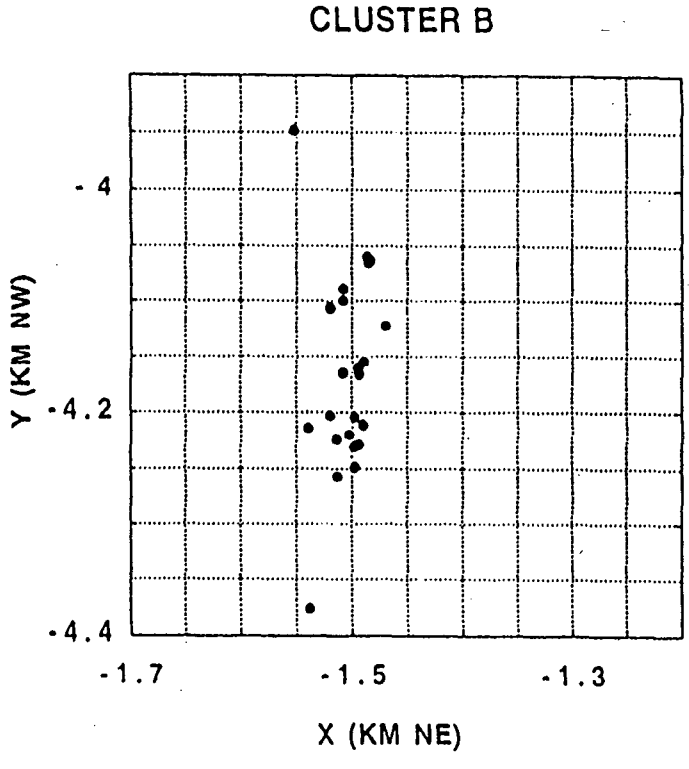

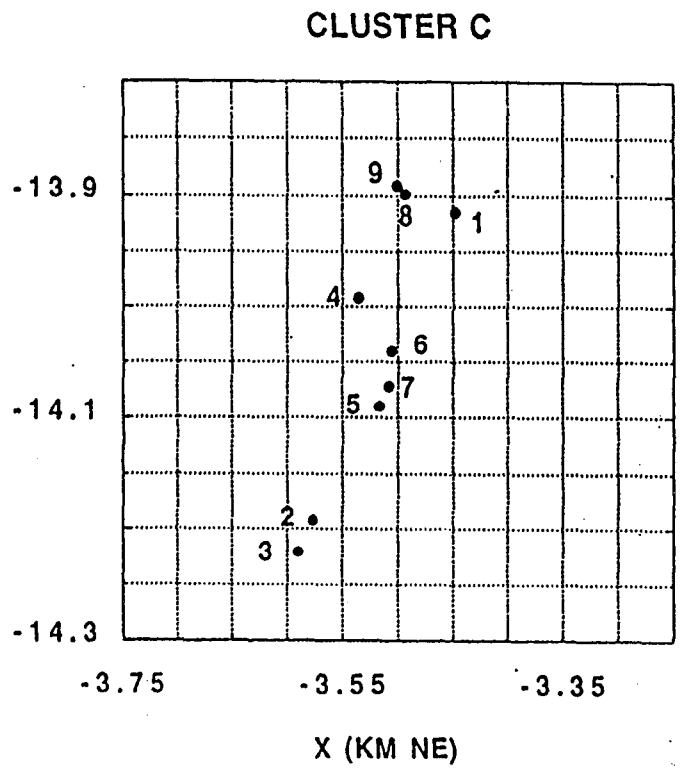

Events

1. 89 273 2256
2. 91 099 1400
3. 91 099 1401
4. 91 099 1547
5. 91 099 1627
6. 91 100 0333
7. 91 100 0400
8. 91 100 0404
9. 91 100 0720

FREQUENCY SCALING AND SOURCE MECHANISMS IN CLUSTERS

Consensus is elusive on earthquake source scaling issues such as stress drop, the magnitude dependence of source dimension or rise time, f_{max}, and whether stress drops vary with tectonic setting. To obtain a solid scaling relationship for a set of earthquakes, all site, path and instrument effects must be accounted for. The use of highly coherent waveforms from cluster members and comparisons within a data set spanning a wide range of magnitudes is possible with the Parkfield data set. We illustrate this potential with a subcluster from Cluster A (Fig. 2.1b) containing six events having magnitudes between 0.3 and 1.8. Fig. 2.9 shows horizontal-component waveforms, S wave velocity spectra, and event-to-event S wave spectral ratios for the five smallest events, each computed with respect to the largest (M1.8) event. The departure from zero slope at ≈40 Hz in the ratios of the smaller events relative to the M1.8 spectrum identifies this frequency as the corner (at this site) for the M1.8 event. The parallel nature of the ratios above 40 Hz for the smallest events suggests a 100 Hz corner frequency (beyond which we lose signal) for an event in the magnitude range 0.5-1.0; i.e., smaller events will in general have corner frequencies above 100 Hz. We cannot measure corner frequencies for the smallest events recorded (M<0) due to the 125 Hz anti-alias filters and the limited 16-bit dynamic range of the data acquisition system. The ripple seen in the spectral ratios, if related to rupture propagation of the M1.8 event, suggests an effective delay of 40-50 ms to station VCA, a value consistent with rupture propagation at the S wave velocity on a fault patch 100-150 m long.

The *en echelon* patterns seen in some clusters at Parkfield and the stable small-scale discrete segments of continuing year-to-year activity suggest that fault slip there is an intricate process, one likely to involve tensional and reverse-slip failure in addition to more conventional pure strike-slip motion on a planar fault. We are investigating this complex rupture hypothesis for earthquakes at Parkfield by reviewing their mechanisms for evidence of a non-double-couple component. This study is motivated by other evidence that non-shear earthquake mechanisms exist on some scale. For example, many laboratory experiments have demonstrated that shear failure is accompanied by 'kinked crack extension', in which a kink (also known as a tension or wing crack) forms near the tip of the shear crack. The orientation of this wing crack is at a high angle to the shear crack and is such that it fails in a tensile mode (29). Fracture-mechanical theory predicts stresses at crack tips which are consistent with the numerous laboratory and field observations of tensional wing cracks (30). It has also been observed that the development of a macroscopic shear plane is due to the coalescence of tensile cracks (29, 31). A substantial fraction of events induced at depth in unfractured granite appear to have a significant tensional component (30, 33). A study of 22 microearthquakes at Long Valley caldera has found that 50% have a substantial amount of non-double-couple radiation (34). Studies of joint formation in granite show clearly that voids open at seismogenic depths (35, 36). Finally, the growing evidence for a major role of high pore pressure (19, 20) in accommodating slip on mature fault zones prompts a search for tensional-failure events indicative of local hydrofracturing under high compressive

stress within the fault zone.

The cluster mechanisms are investigated for evidence of non-shear source components, by computing S/P spectral ratios in the frequency band below 5 Hz for three-component data at a number of recording sites at a range of azimuths (24, 34). Predicted values of the ratios for appropriately oriented tensile and shear sources are compared with the observations in a search for evidence of non-shear mechanisms. We have so far examined more than ten earthquakes, sampling clusters and isolated events. We illustrate the analysis in Fig. 2.10, comparing a member of Cluster B with an isolated event ('S' in Fig. 2.2). Spectral ratios for Cluster B suggest that these earthquakes involve a substantial non-double-couple component. Cluster C (not illustrated, see Fig. 2.1) also appears to have some non-shear source component. On the other hand, isolated Event S has an S/P spectral ratio that agrees well with a double-couple mechanism. We have begun to map the source mechanism character and its variation throughout the fault zone, with the goal of relating it to the mode and geometry of ongoing fault slip, to the dynamics of the locked-to-creeping transition, and to the M6 nucleation process at Parkfield.

Fig. 2.9. S wave spectral scaling for six events in Cluster A for station VCA, east component: (Top) Horizontal-component seismograms for events with magnitudes as indicated, and showing the S wave window used for spectral computation. (Center) Velocity spectra for the windowed S waves. The dashed curve represents atypical noise spectrum. (Lower) Ratios of the S wave spectra to the largest of the events.

CLUSTER A

VCAE

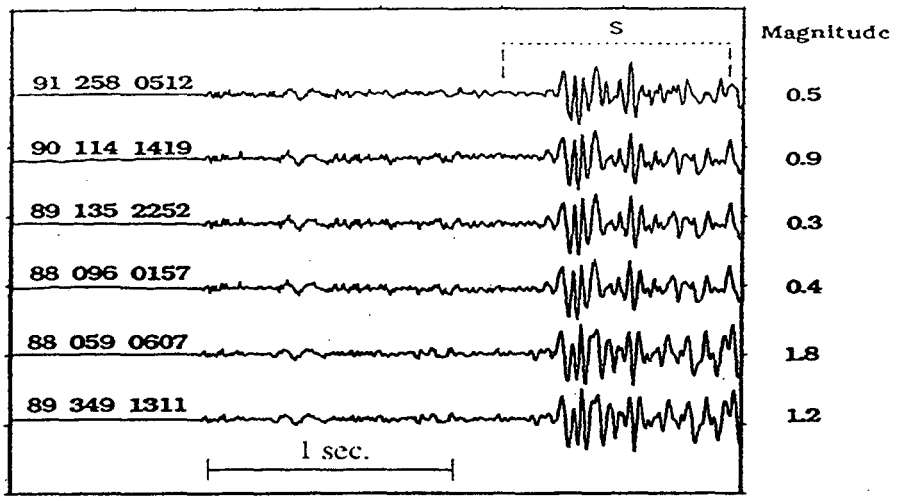

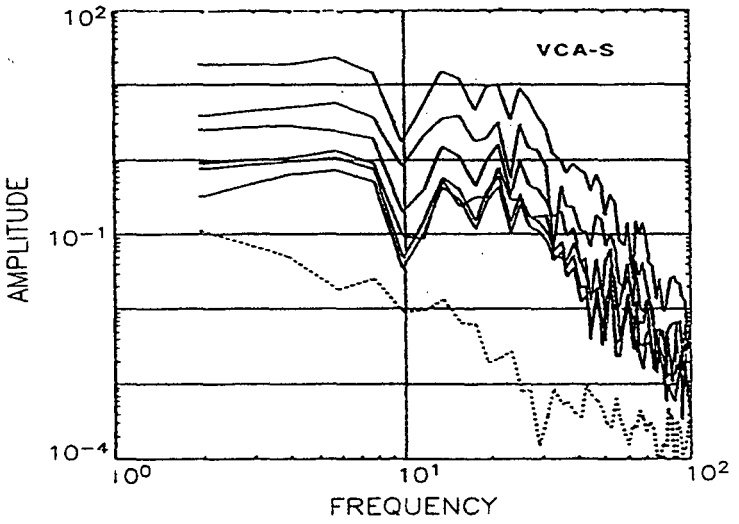

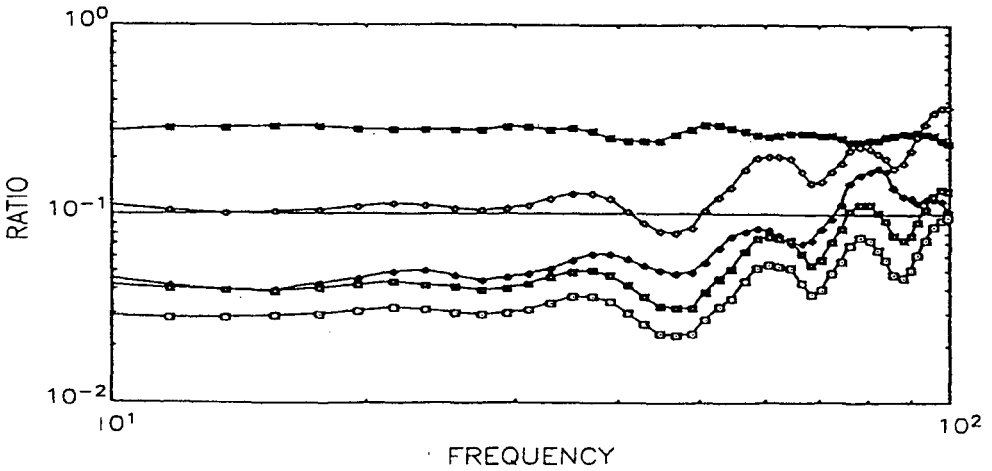

Fig. 2.10. Comparison of observed low-frequency S-to-P spectral ratios as a function of azimuth to those ratios as calculated for a strike-slip (shear) source on the local fault surface, and as calculated for tensile cracks oriented 70° to the main and auxiliary fault planes: (Left) Event in Cluster B exhibiting tensile-type spectral ratios. (Right) Event S, exhibiting spectral ratios more consistent with a shear source.

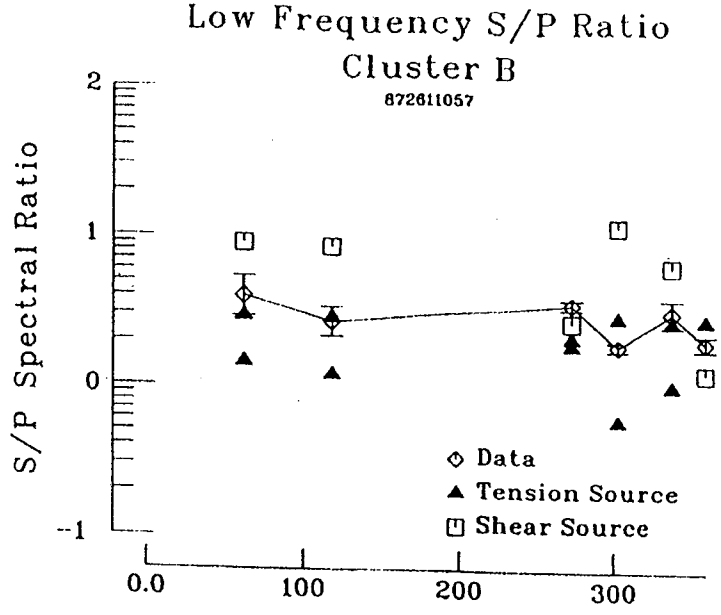
Low Frequency S/P Ratio
Cluster B
872611057
S/P Spectral Ratio
2
1
0
-1
0.0
100
200
300
Data
Tension Source
Shear Source
Source-to-Receiver Azimuth

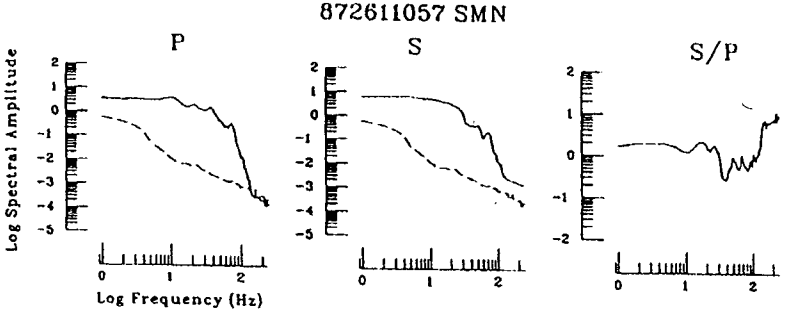
872611057 SMN
P
S
S/P
Log Spectral Amplitude
Log Frequency (Hz)

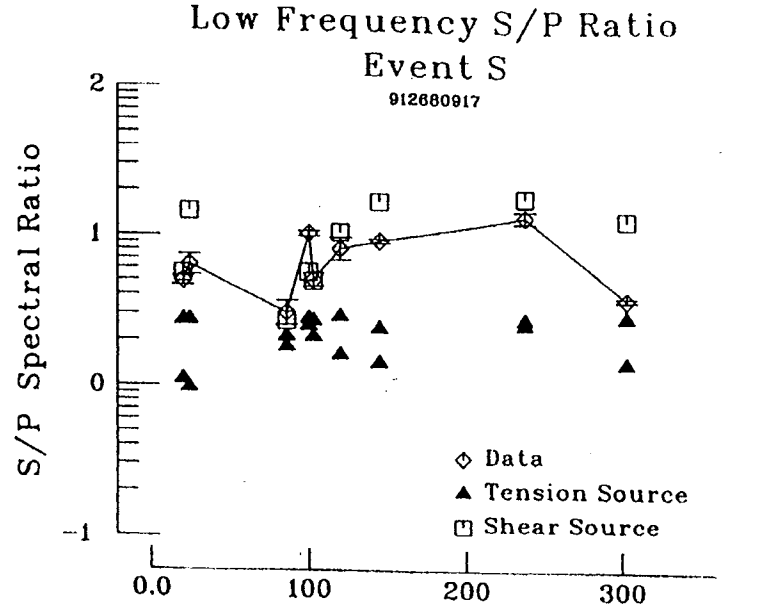
Low Frequency S/P Ratio
Event S
912680917
S/P Spectral Ratio
2
1
0
-1
0.0
100
200
300
Data
Tension Source
Shear Source
Source-to-Receiver Azimuth

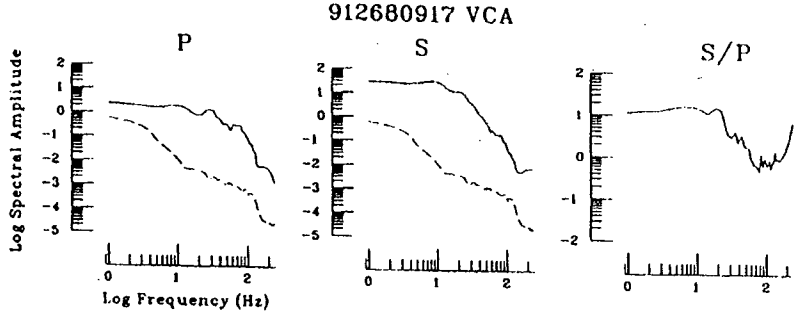
912680917 VCA
P
S
S/P
Log Spectral Amplitude
Log Frequency (Hz)

CLUSTERS AS MONITORING SOURCES - SOME EXAMPLES

Repeating cluster events, with nearly identical waveforms and hypocenters, may be used to monitor the fault-zone environment for changes in P and S wave travel times, frequency content, attenuation and polarization in an effort to detect any changes in medium properties affecting wave propagation that may have occurred in the nucleation zone at Parkfield during the period of network operation, now over six years. This operating period is a substantial fraction of the 20-25 years average recurrence time for previous Parkfield earthquakes. By assuming source co-location, repeatability of mechanism, and constant receiver response, we limit the cause of any observed waveform differences predominantly to temporal variation in the propagation medium. In fact, however, second-order variations may exist due to the small changes in cluster event locations, magnitudes and mechanisms, to possible near-source nonlinear strain-dependent wave-propagation effects, and to small changes induced in the immediate environment of the cluster by the failure processes of the small sources themselves. Detection and separation of these phenomena is a primary goal in our research on the Parkfield high-resolution network data.

We have developed three techniques with which to examine specific aspects of elastic wave propagation for changes with time. Because of the unique fault-zone illumination this particular combination provides in the vicinity of the presumed nucleation zone (see Figs. 2.1b and 2.4c), we use events in Cluster A at 10 km depth recorded at stations VCA and MMN to

illustrate these techniques. Specifically, seismic waves emitted from a member of Cluster A and recorded at station MMN sample the proposed M6 nucleation zone, while waves from the same event travel to station VCA on a path that samples the nucleation zone only minimally. This geometry-dependent sampling can be very useful in isolating medium changes from other source and receiver effects. The large number and distribution of the clusters provides a rather full illumination of the study region. We explore the monitoring concept by examining the stability of P and S wave velocities, spectral amplitudes, and polarizations of the P and S direct arrivals and their coda structures.

First we examine travel-time stability, using the continuous cross-correlation technique applied to cluster event waveforms (22). In this method one trace from the illuminating cluster is selected as a reference. This reference is then cross-correlated with waveforms from every other cluster member in turn, resulting in a set of waveform comparison pairs. For each pair, the P wave arrivals of the two traces are aligned to the nearest 2 ms sample (±1 ms time uncertainty). Then an 80 ms boxcar moving time window is stepped down the two traces in 6 ms increments (these windowing parameters were determined experimentally). For each time step, the lag of the correlation maximum gives the offset (to the nearest sample) between corresponding time windows of the two traces. The windowed offsets in trace-time order constitute new time series describing the relative delays between waveform pairs. The set of delay-time traces are then gathered in order of event occurrence time and displayed in color (Fig. 2.11). The method provides an effective multi-

dimensional visual means for displaying lag times throughout waveform time for all the members of a cluster as a function of calendar time.

Fig. 2.11 presents two lag time displays, one for Cluster A recorded at station VCA and one for the same set of events as recorded on MMN. The six horizontal-component traces are arranged in order of event occurrence, from April, 1988 to April 1991. Four seconds of data are shown beginning at 0.1 sec before the P arrival, and the reference trace (green, trace #3) is overlain with the corresponding 4 seconds of the reference waveform. Interpolation is applied between and within traces. Notice the relative stability -- i.e., "greenness" -- of the VCA display, compared to that of MMN, especially in the P and S coda. This suggests a greater variability with time in the medium along the raypath between Cluster A and station MMN -- which includes the proposed nucleation zone -- than for the medium between Cluster A and station VCA -- largely outside the nucleation zone. An alternate explanation attributes the greater variation seen at MMN to noise interference there due to lower signal-to-noise ratio at that station for those events. The events used from Cluster A are M0.5 in magnitude, with peak amplitudes of a few hundred digital counts at MMN. We are exploring this possibility with more energetic Cluster A members, including a subcluster of M1.5 events (a few thousand counts maximum amplitudes). Preliminary indications are that the coda appears more stable at MMN for these larger cluster events in the same source region.

Shifts of a few ms in P and S wave arrival times yield a separation of about

20 m between two calculated hypocenters in a cluster. To estimate the size of a velocity perturbation that would be required to produce an apparent 20 m separation of two co-located events, we calculated delays by applying a small perturbation to the P and S velocities in the anomalous V_P/V_S zone. No simple perturbation produces exactly the observed shift in the hypocenter, but an apparent movement of 20 m can be induced by a velocity perturbation of about 0.5 percent in a volume about 2 km wide near the focus.

Fig. 2.11. Travel time lags for six events in Cluster A as a function of trace time, 0-4 sec. Traces are plotted in chronological order, beginning with April 1988 (Event 1 on the vertical axis) and ending in April 1991 (Event 6). Lag times are relative to trace 3, an event in June, 1988. (Upper) Data for horizontal component 2 (90°), Station VCA. (Lower) Data for horizontal component 2 (265°), Station MMN.

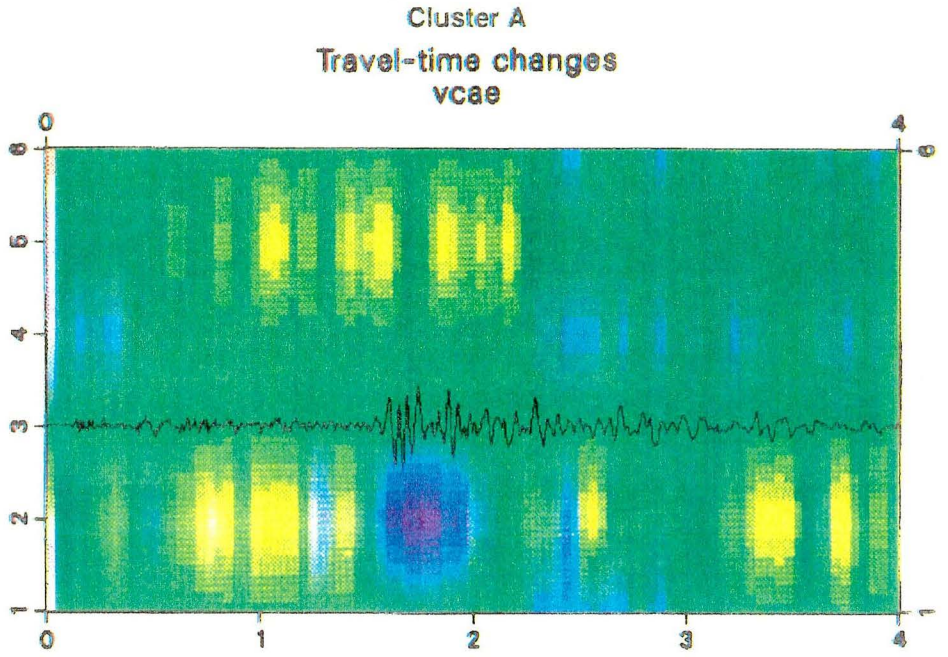
Cluster A
Travel-time changes
vcae
0
4
6
5
4
3
2
1
0
1
2
3
4

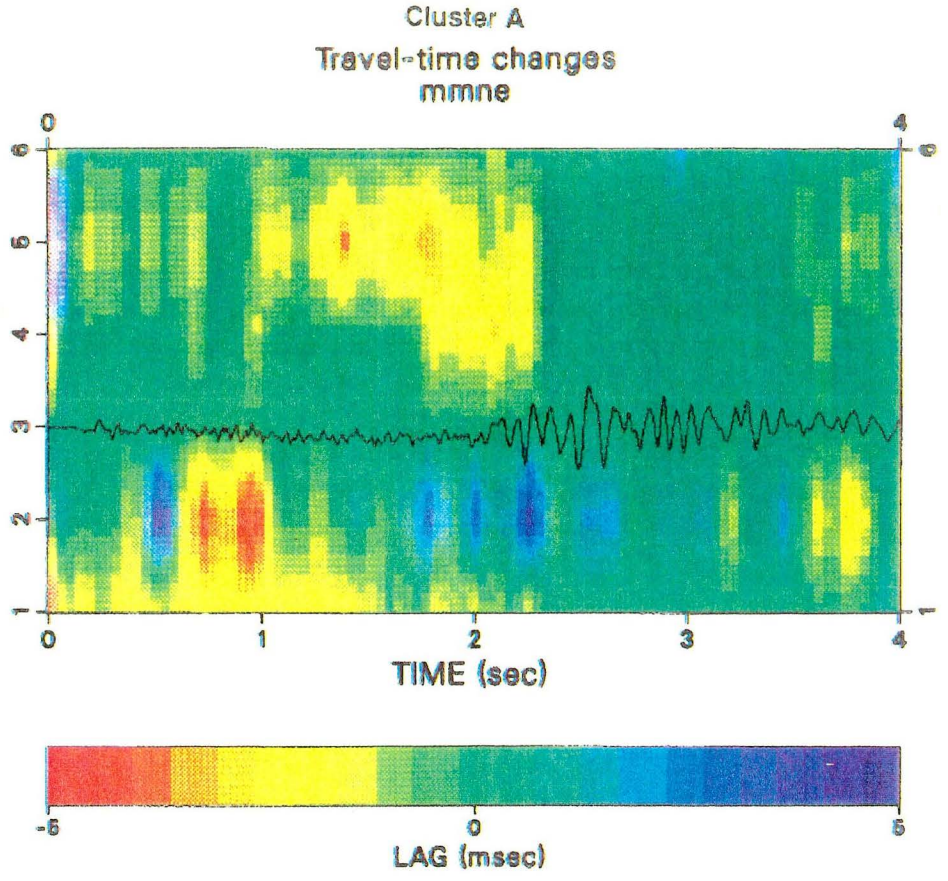
Cluster A
Travel-time changes
mmne
0
4
6
5
4
3
2
1
0
1
2
3
4
TIME (sec)
-5
0
5
LAG (msec)

Next we examine variability in the amplitude spectra with time using a continuous trace-display technique (22). In this method, the spectrum of the waveform is computed, for one component from each event, along the trace time axis using a 128 ms window moved in 128 ms steps. The resulting multi-dimensional data set consists of a continuously varying amplitude spectrum along the recording time axis with separate display panels for each event. Spectral strength is given by the color, normalized to span the spectral range of the respective trace. The spectra are arranged in the order of event occurrence..

Fig. 2.12 illustrates the time-varying spectral analysis with 3 events from Cluster A recorded at VCA and MMN. A 4-second sample waveform from the event cluster is also shown, starting 0.1 s before P. The events (3, 4, and 6 in Fig. 2.11) occurred in June, 1988, May, 1989 and April, 1991. While the spectral character seen at VCA remains rather stable, the MMN data show significant variation, especially between events 3 and 4. A greater spectral amplitude variability in the medium between Cluster A and MMN is consistent with the result above for the travel-time analysis, including the possible effects of low signal-to-noise ratio at MMN.

Fig. 2.12. Spectral amplitudes as a function of trace time for three members of Cluster A (events 3 (Jun/88), 4 (May89) , and 6 (Apr91) in Fig. 2.11). Color scale is normalized to the spectral range of each trace. (left) Station VCA, horizontal component 2. (right) Station MMN, horizontal component 2.

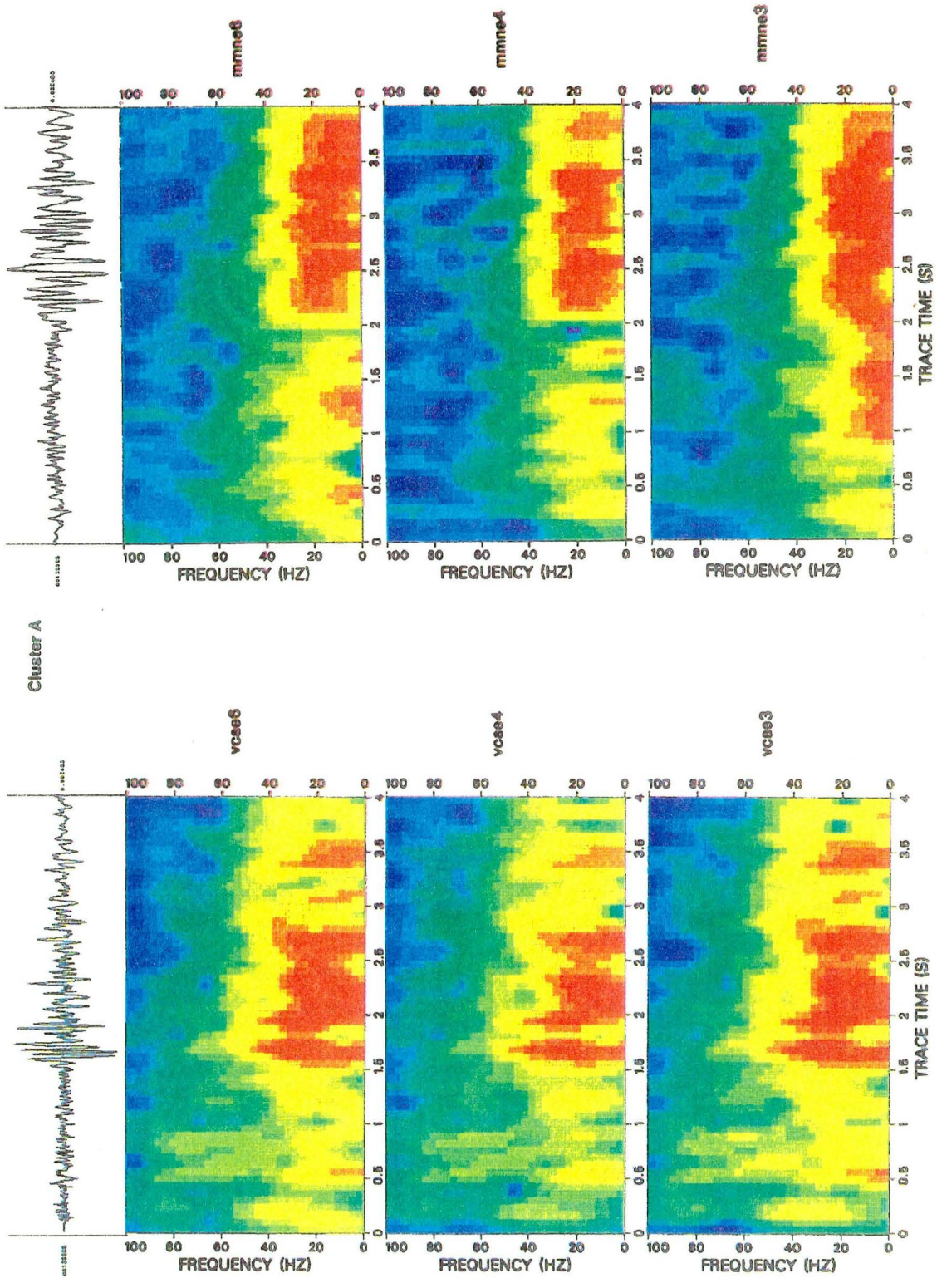
Cluster A
mmne5
mmne4
mmne3
vcse5
vcse4
vcse3
FREQUENCY (HZ)
TRACE TIME (S)

Finally, we examine time-variable polarization characteristics by comparing vector linearity traces which represent polarizations in trace time as previously defined (37). Fig. 2.13 illustrates the method. A 50 ms (25 samples) boxcar time window is moved down the 3-component waveform in 2 ms steps. For each window, the vector linearity is computed from the 3-D particle motion (top). The resultant pseudo-vector is plotted on the color trace (bottom) as a single colored and shaded pixel. The pixel's position in time along the color trace corresponds to the center of the analysis time window. Its placement along the inclination axis reflects the vertical projection of the linearity vector, with more vertically-incident energy presumably defining P waves. The color hue of the pixel represents vector azimuth (0° to 180°, North from East), and the color intensity represents the magnitude of the linearity as previously defined (38). This type of display combines information from all three waveform components into a single trace and allows the investigator simultaneously to view indicators of wave type, scattering and conversions, S wave splitting, polarization directions and degree of vector linearity. A series of these displays for members of a single cluster can be made as a function of occurrence time and receiver location, thus identifying differing degrees of waveform stability in the direct waves and the P and S coda for propagation throughout the network volume.

Fig. 2.13. Schematic diagram of the 3-component vector linearity and polarization calculation used in the study of total wavefield character and its stability with time. The upper illustration defines the polarization geometry estimated within the moving window shown on the three seismograms. The color trace at the bottom displays the estimated vector properties in a 50 ms moving window stepped in 2 ms increments down the seismograms: color trace position indicates the inclination of the vector (the top of the frame is fully vertical polarization vector orientation, expected for P waves, while the bottom of the frame is horizontal polarization expected for S waves), trace color hue gives the horizontal azimuth (N from E) of the linearity vector, and color intensity represents the magnitude of its linearity. Note the clear separation of P and S arrivals and their respective coda compositions by the inclination parameter.

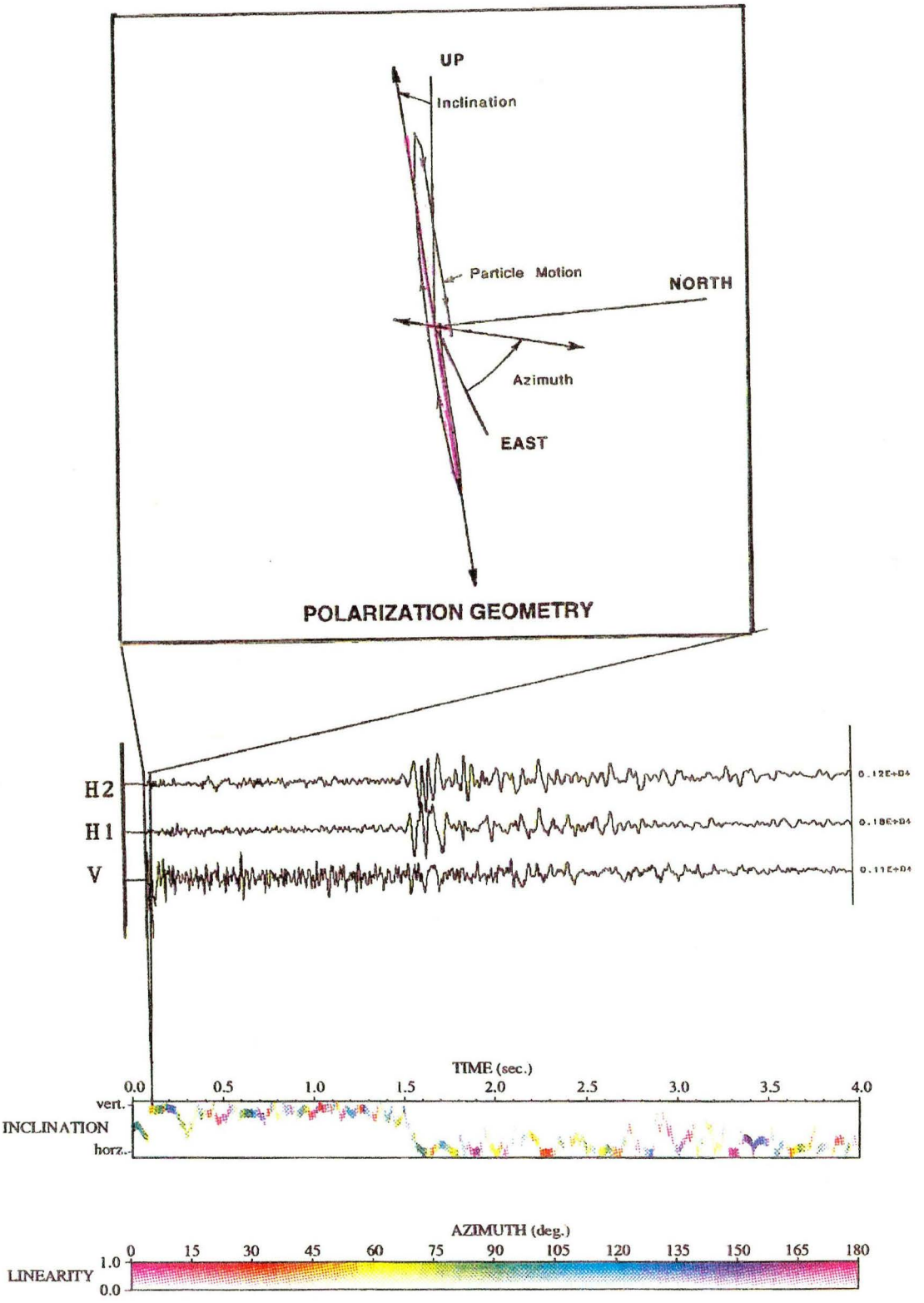
UP
Inclination
Particle Motion
NORTH
Azimuth
EAST
POLARIZATION GEOMETRY
H2
H1
V
TIME (sec.)
0.0
0.5
1.0
1.5
2.0
2.5
3.0
3.5
4.0
vert.
INCLINATION
horz.
AZIMUTH (deg.)
0
15
30
45
60
75
90
105
120
135
150
165
180
LINEARITY
1.0
0.0

Fig. 2.14 illustrates vector linearity results for 4 seconds of data (beginning 0.1 s before P) at stations VCA and MMN for the three M0.5 events of Cluster A shown in Figs. 2.11 and 2.12, and for three larger M1.5 events from a nearby subcluster within A (about 100 m distant) recorded at MMN and spanning a similar time interval (2/88, 12/89, 7/91). Example 3-component waveforms are displayed for reference. Note the remarkable similarity of the polarization traces throughout the seismograms for the smaller events recorded at VCA (Events 3,4,6) and for the nearby larger events recorded at MMN. The similarity between the cluster members is much less for the small M0.5 events recorded at MMN, where signal levels are generally lower, presumably due to attenuation in the fault zone. The similarity is retained in the larger signals of the direct S waves. This observation suggests that the signal-to-noise ratio must be monitored when investigating variations in full waveforms over time, particularly P and S coda waves.

The vector linearity trace highlights other features of wave propagation. In clean waveforms rich in high frequencies (e.g., VCA) we see a persistent dominance of vertically-polarized energy (P waves) throughout the entire P coda until the fairly abrupt shift at the S arrival to similarly persistent horizontally-polarized energy (S waves) in the S coda. At MMN, however, where the signals always exhibit lower frequency content, the P coda is much richer in S-polarized arrivals. S codas are not as different between the two stations, exhibiting generally similar codas with predominantly S energy and containing several discrete P-like arrivals. Attenuation differences between the two paths alone cannot explain this spectral

contrast. in the waveforms. Simple scattering models, which call for progressively enhanced S wave content in the P coda (e.g. , 39), suggest that the path to MMN is rich in scattered, multipath S energy. This is not surprising, given the location of station MMN on the SAF trace. However, waveforms recorded at other stations (RMN, JCS) sited NE of the SAF that we have analyzed in this fashion display P coda properties like MMN, whereas waveforms recorded SW of the SAF (e.g., FRO) exhibit P coda similar to VCA. This P coda difference suggests that the Franciscan upper crust NE of the SAF is much more heterogeneous at wavelengths of 50 to 500 m than is the crust SW of the fault zone.

Fig. 2.14 illustrates the nature of the direct S arrival as the polarization changes from P- to S-type. At VCA, the direct S wave arrival emerges cleanly from the dominantly P-polarized P coda over about 0.1 s (the moving window is 0.05 s long). This suggests either a somewhat emergent amplitude buildup in the direct S wavefront, or a field of forward-scattered P waves off the direct S, or some combination of such effects. For the low-frequency waveforms, we see several sharp transitions between P- and S-type polarizations as the 'direct' S arrival emerges. This detail of the S wave onset structure has implications for precise arrival time determinations and for analyses that use the onset of S assuming it to be a pure S wave.

The vector linearity trace formalism lends itself particularly well to the analysis of S wave anisotropy. We observe polarization shifts of approximately 90 degrees (red/orange to green/blue azimuth differences

in Fig. 2.14) within the complex S wave arrival. A marked 90 degree contrast in azimuth is seen clearly at MMN between two parts of the direct S wave separated in time by some 300-400 ms. If this is an indication of birefringence, propagation through the nucleation zone (MMN data) shows a much stronger effect than propagation oblique to the zone (VCA data). The pattern of polarization azimuths appears to remain stable throughout the 3+ year period. The earlier arriving S wave at MMN is polarized parallel to the fault zone and the slower S wave is polarized normal to the fault. Their travel times differ by about 8 percent from the source to MMN. This geometry is consistent with that seen near the fault zone in shear-wave Vibroseis studies (22), and in a VSP survey (40). Those observations suggest anisotropy closely related to the sheared fabric of the fault zone, with a horizontal axis of symmetry normal to the fault plane. Such a geometry is also consistent with anisotropy of permeability within the fault zone (20).

No significant variations are apparent over the Feb88 - Jul91 time span for P and S wave travel times and spectra for VCA seismograms from Cluster A events, nor for coda polarizations in those data and MMN data from Cluster A. These three techniques for detecting subtle differences among waveforms of cluster members represent a potentially powerful monitoring scheme for identifying and delineating regions in the subsurface that are experiencing temporal variations in material properties, presumably due to the nucleation process. Assuming constant receiver response through time, the marked stability observed at VCA requires both similarity in the source time functions and a stable propagation medium. The observed

stability of the source time function then allows us to attribute the variation with time seen at other stations to changes in the propagation medium between cluster and station. A massive exercise using all clusters and stations can produce an effective 3-D tomographic image of the variations in network-sized volume that contains the expected hypocenter and its surrounding environment.

Fig. 2.14. Vector linearity and polarization displays for the three M0.5 events of Cluster A used in the spectral displays in Fig. 2.12, and for three larger M1.5 events from a nearby cluster also recorded at MMN spanning about the same time interval (Feb88, Dec89, Jul91). The colored traces contain information on the stability of the composition of the P and S coda, travel times, birefringence, multipathing, scattering and attenuation effects in the wavefield over the 1988-1991 interval. Differences are small for the well-recorded signals. (top) Cluster A data for Station VCA (middle) Cluster A data for Station MMN. (bottom) MMN data for M1.5 events in a nearby cluster. Note the greater stability in the coda waveforms at MMN of these larger events.

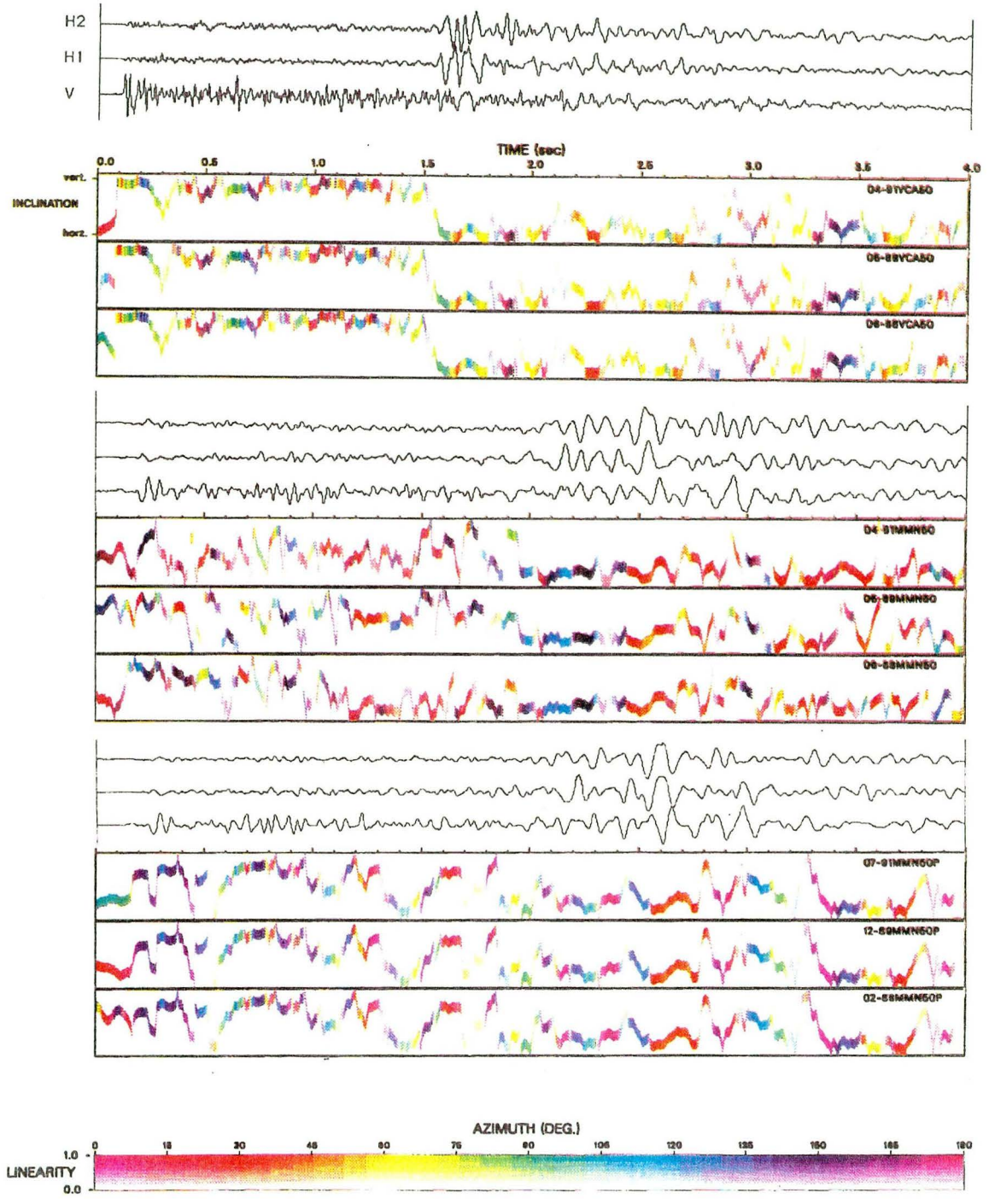
H2
H1
V
TIME (sec)
0.0
0.5
1.0
1.5
2.0
2.5
3.0
3.5
4.0
vert.
INCLINATION
horz.
04-91VCA50
05-88VCA50
06-88VCA50
04-91MMN50
05-88MMN50
06-88MMN50
07-91MMN50P
12-88MMN50P
02-88MMN50P
AZIMUTH (DEG.)
0
15
30
45
60
75
90
105
120
135
150
165
180
1.0
LINEARITY
0.0

SUMMARY AND CONCLUSIONS

The very high resolution in relative hypocenter locations attainable due to the 100 Hz bandwidth and low noise of the Parkfield borehole network has provided the observation that more than half of the microearthquakes are members of some 80 clusters of very similar events. The clusters, with dimensions of 50-200 m, contain events with high P and S wave coherency (>0.9) to frequencies of 50-100 Hz. Clusters are distributed throughout the fault zone around the presumed nucleation region, in the locked section to the SE and in the creeping part to the NW of the expected hypocentral location. Some clusters contain events that occur more or less independently over time, while others are seen to include, in addition, bursts of events over durations of minutes to days. The cluster events provide a new perspective on the process underway in the presumed near-term earthquake cycle at Parkfield, adding details on the failure modes along the fault surface and acting as repeated wide-bandwidth sources of illuminating elastic waves with which to probe for process-induced temporal changes in physical properties in and around the presumed nucleation zone. Initial results presented here from several prototype studies on some of the potential research applications of the cluster phenomenon have been very encouraging, and a subsequent effort is presented in chapter III.

In this 1987 - 1992 study we obtained results for a few clusters and receivers. Findings for that period are as follows:

Clusters are typically 100 to 200 m in maximum dimension.

Relative location accuracy for cluster members is probably 5-10 m, and the point located is some averaged centroid of energy release on the rupture surface.

Clusters are found in both the creeping and the locked sections of the fault zone at Parkfield.

Corner frequencies are around 40 Hz and >100 Hz for M~1.8 and M~0.5, respectively.

There is evidence for non-shear mechanisms in some cluster events.

P and S wave codas remain predominantly P and S waves, respectively, throughout their lengths.

Repeated cluster sources, used in a monitoring mode for possible temporal changes in nucleation-zone properties, can reveal very small changes in the total waveform, including travel-times, spectral content, and S wave polarization. Preliminary application of this method using raypaths near the presumed nucleation zone did not reveal significant variations over a 3+ year period.

Questions remain open on the nature of the clusters and their potential uses:

Does each cluster event break the entire 'patch', or just a part of it?

Is the Parkfield cluster behavior common to other segments of the San Andreas fault or to other active fault zones? Does it reflect a changing state of slip dynamics related to the

nucleation process?

Are the patches stronger or weaker than their surroundings?

Is the *en echelon* geometry suggested in some cluster patterns evidence for the mode of progressive yielding of the fault zone?

Is the presence of high pore-fluid pressure a controlling factor in cluster seismicity and/or major earthquake occurrence?

Can we separate effects of medium changes near the hypocenter from slightly differing locations?

Will the cluster behavior change measurably as the failure cycle for Parkfield begins to close, or, following the M6 event?

Do the P and S coda constitute sensitive probes of the deep fault zone?

Can the clusters be used to monitor for changes in the high Vp/Vs anomaly seen in the presumed nucleation zone?

Subsequent efforts addressed the problems of systematizing the full sequence of processing and analysis steps involved in identifying cluster members and integrating them into the various monitoring efforts. Previous research has identified a zone of apparently changing travel times south of MMN in the Vibroseis monitoring program (22). We hope to concentrate observations and analysis in this area during times of alert and during the aftershock sequence of the expected M6 earthquake. Cluster member recurrence intervals vary from less than a minute to

months or years. Cluster events widely separated in time provide long-term sampling histories for monitoring, but they fail to give the detailed medium history essential for understanding fine-scale changes late in the failure cycle. Bursts of events within a cluster can provide a detailed picture of the changing stress conditions.

ACKNOWLEDGMENTS

This chapter was published previously as an article in the Bulletin of the Seismological Society of America (6) and was co-written with Michael Antolik, Peggy Johnson, William Foxall, and Thomas McEvilly. The authors thank E. Karageorgi for her help in adaptation of travel time lag and spectral amplitude analyses techniques to microearthquake sources. The Parkfield High-Resolution Seismic Network functions through close cooperation among researchers at the University of California at Berkeley, Lawrence Berkeley Laboratory, Duke University and the US Geological Survey. USGS provides financial support for this research through NEHRP award 14-08-0001- G1703. Data processing was done at the Center for Computational Seismology at LBL, which is operated by the University of California for the US. Department of Energy under contract No. DE-AC03-76SF00098.

REFERENCES

1. W. H. Bakun and T. V. McEvilly, J. Geophys. Res. 89, 3051 (1984).

2. R. R. Robinson, R. L. Wesson, W. L. Ellsworth, Science 184, 1281 (1974); M. A. Sadovsky, I. L. Nersesov, S. K. Nigmatullaev, L. A. Latynina, A. A. Lukk, A. N. Semenov, I. G. Simbireva and V. I. Ulomov, Tectonophysics 14, 295 (1972); C. H. Scholz, L. R. Sykes Y. P. Aggarwal, Science 181, 803 (1973); J. H. Whitcomb, J. D. Garmany D. L. Anderson, Science 180, 632 (1973).

3. T. V. McEvilly and L. R. Johnson, Bull. Seism. Soc. Am. 64, 343 (1974); D. M. Boore, A. G. Lindh, T. V. McEvilly, W. Tolmachoff, Bull. Seism. Soc. Am. 65, 1407 (1975).

4. W. H. Bakun, and A. G. Lindh, Earthq. Predict. Res. 3, 285 (1985).

5. P. E. Malin S. N. Blakeslee, M. G. Alvarez, A. J. Martin, Science 244, 557 (1989).

6. R. Nadeau, M. Antolik, P. Johnson, W. Foxall, T. V. McEvilly, Bull. Seismol. Soc. Am. 84, 247 (1994).

7. R. M. Nadeau, W. Foxall, T. V. McEvilly, Science 267, 503 (1995).

8. Y.-G. Li and P. C. and Leary, Bull. Seism. Soc. Am. 80, 1245 (1990); Y. Ben-Zion and P. Malin, Science 251, 1592 (1991).

9. A. Michelini and T. V. McEvilly, Bull. Seism. Soc. Am. 81, 524 (1991).

10. N. Deichmann and M. Garcia-Fernandez, Geophys. J. Int. 110, 501 (1992).

11. A. J. Michael and D. Eberhart-Phillips, Science 253, 651 (1991).

12. J. M. Lees and P. E. Malin, J. Geophys. Res. 95, 21793 (1990).

13. A. Michelini, Ph. D. Thesis, Univ. Calif., Berkeley (1991).

14. W. Foxall, Ph. D. Thesis, Univ. Calif., Berkeley (1992).

15. W. Foxall, A. Michelini, T. V. McEvilly, J. Geophys. Res. 98, 17691 (1993).

16. A. Nur, Bull. Seism. Soc. Am. 62, 1217 (1972).

17. A. H. Lachenbruch, J. Geophys. Res. 85, 6097 (1980).

18. C. B. Raleigh, Proceedings of Conference II, Experimental Studies of Rock Friction with Application to Earthquake Prediction, U. S. Geological Survey, Menlo Park, CA., 291 (1977).

19. J. Byerlee, Geophys. Res. Lett. 17, 2109 (1990).

20. J. R. Rice, Fault Mechanics and Transport Properties of Rocks, edited by Brian Evans and Teng-fong Wong (Academic Press, 1992).

21. A. Nur and J. Walder, Fault Mechanics and Transport Properties of Rocks, edited by Brian Evans and Teng-fong Wong (Academic Press, 1992).

22. E. Karageorgi, R. Clymer, T. V. McEvilly, Bull. Seism. Soc. Am. 82, 1388 (1992).

23. R. C. Aster and J. Scott, Bull. Seism. Soc. Am. 83, 1307 (1993).

24. P. A. Johnson, M. Antolik, W. A. Peppin, W. Foxall, T. V. McEvilly, Seism. Res. L. 63, 75 (1992).

25. G. Poupinet, W. L. Ellsworth, J. Frechet, J. Geophys. Res. 89, 5719 (1984).

26. M. -J. Fremont and S. D. Malone, J. Geophys. Res. 92, 10223 (1987).

27. W. Foxall and T. V. McEvilly, Seism. Res. L. 59, 1 (1988).

28. A. Ito, Tectonophysics 175, 47 (1990).

29. S. Nemat-Nasser and H. Horii, J. Geophys. Res. 87, 6805 (1982).

30. D. D. Pollard and P. Segall, Fracture mechanics of rock (Academic Press, London, 1987).

31. D. K. Hallbauer, H. Wagner, N. G. W. Cook, Int. J. Rock Mech. Min. Sci. Geomech. Abstr. 10, 713 (1973).

32. B. Feignier and R. P. Young, EOS, Trans. Am. Geophys. Un. 72, 292 (1991).

33. S. J. Gibowicz, R. P. Young, S. Talebi, D. J. Rawlence, Bull. Seism. Soc. Am. 81, 1157 (1991).

34. W. A. Peppin and P. A. Johnson, Bull. Seism. Soc. Am. (in press) (1993).

35. S. J. Martel, D. D. Pollard, P. Segall, Bull. Geol. Soc. Am. 100, 1451 (1988).

36. S. J. Martel and D. D. Pollard, J. Geophys. Res. 94, 9417 (1989).

37. R. C. Aster, P. Shearer, J. Berger, J. Geophys. Res. 95, 12449 (1991).

38. R. C. Aster and P. Shearer, Bull. Seism. Soc. Am. 81, 1057 (1991).

39. R. Wu and K. Aki, Geophysics 50, 582 (1984).

40. T. M. Daley and T. V. McEvilly Bull. Seism. Soc. Am. 80, 857 (1990).

CHAPTER III

Clustering and Periodic Recurrence of Microearthquakes on the San Andreas Fault at Parkfield, California

(R. M. Nadeau, W. Foxall, and T. V. McEvilly, 1995, with modifications)

ABSTRACT

The San Andreas fault at Parkfield, California, apparently late in an interval between repeating magnitude 6 earthquakes, is yielding to tectonic loading partly by seismic slip concentrated in a relatively sparse distribution of small clusters (<20-meter radius) of microearthquakes. Within these clusters, which account for 63% of the earthquakes in a 1987 - 92 study interval, virtually identical small earthquakes occurred with a regularity that can be described by the statistical model used previously in forecasting large characteristic earthquakes. Sympathetic occurrence of microearthquakes in nearby clusters was observed within a range of about 200 meters at communication speeds of 10 to 100 centimeters per second. The rate of earthquake occurrence, particularly at depth, increased significantly during the study period, but the fraction of earthquakes that were cluster members decreased.

INTRODUCTION

Conceptual methods for earthquake forecasting and hazard mitigation depend critically on the process of fault slip being time-varying in a predictable manner, and evidence for such behavior has been elusive (1). In this report we describe patterns of microseismicity that show clustering in space, periodic recurrence, and systematic changes with time on the Parkfield stretch of the San Andreas fault, and we discuss possible mechanisms for this behavior.

Since 1987, seismicity near Parkfield, California, has been monitored with a network of sensitive seismographs installed in boreholes. This stretch of the San Andreas fault has experienced magnitude (M) 6 earthquakes on average every 22 years, on the basis of the record from 1857 to 1966 (2). Hypocenter locations for the last three events in the sequence define a common nucleation zone on the fault to within a few kilometers. A diverse earthquake prediction experiment is underway at Parkfield to establish a baseline of parameters that may reveal anomalous behavior before the next M 6 event (3).

Approximately 3000 earthquakes were recorded and located from 1987 to June 1994 on the central 25-km-long section of the fault zone being studied. A three-dimensional model for P and S wave velocities for this segment has been developed from the microearthquake data (4). These small earthquakes are concentrated along a slipping fault zone that is characterized by locally depressed seismic wave velocities, particularly

the shear-wave velocity (Vs), and by a region of elevated Vp/Vs near the presumed nucleation volume of the repeating M 6 earthquakes (Vp is the velocity of the P wave).

More than half of the earthquakes can be grouped spatially into small clusters within which events exhibit highly similar recorded waveforms, in many cases over the full 100-Hz bandwidth of the data (Fig. 3.1) (5). The generation of near-identical waveforms at wavelengths as short as 50 m suggests that the sources of seismic wave radiation for these clustered events are essentially repeating ruptures on a common slip surface. We are dealing mainly with small earthquakes in the magnitude range 0 to 1 on fault surfaces with dimensions of a few meters (6). The largest events studied have conventionally estimated source dimensions of a few tens of meters, although it is possible that the source dimension has been overestimated because of attenuation effects (7). Within the individual clusters, where relative location resolution is a few meters, we can study fault zone dynamics at a scale approaching that of large laboratory experiments.

Fig. 3.1. Waveforms recorded at station VCA from cluster CL14. Recorded amplitude (counts/1000) are shown on the right. The cluster subdivides into three types of events on the basis of subtle differences in waveform, as indicated by the numbers on the left.

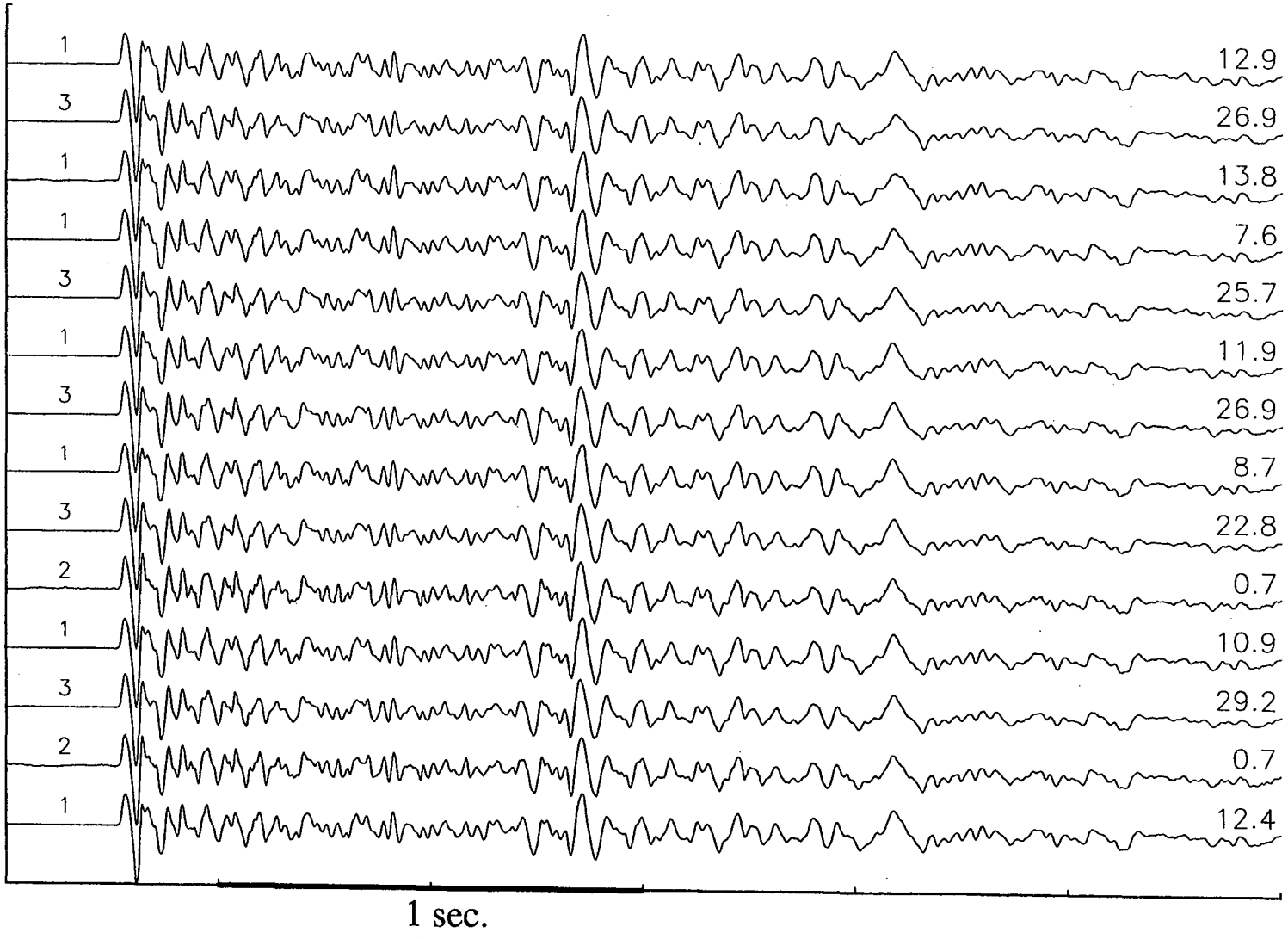
1
3
1
1
3
1
3
1
3
2
1
3
2
1
12.9
26.9
13.8
7.6
25.7
11.9
26.9
8.7
22.8
0.7
10.9
29.2
0.7
12.4
1 sec.

CHARACTERIZATION OF CLUSTERS USING WAVEFORM SIMILARITY

To analyze the clustering phenomenon quantitatively, we assigned the ~1700 earthquakes in the 1987 - 92 period to event clusters using an equivalency class (EC) algorithm (8, 9), which was refined by visual inspection and regrouping. The similarity measure, β, used in the EC organization is based on a network-wide characterization of maximum cross-correlation coefficient values for P and S waves between pairs of earthquakes, and it varies systematically with the distance (offset) separating event pairs (Fig. 3.2). An interesting result of this analysis was that the correlated earthquake pairs tended to fall into two distinct, offset-dependent populations. One group ($\beta > 0.9$) contains event pairs separated by less than about 200 m, and the other group contains those pairs ($\beta < 0.6$) having offsets greater than 500 m. The β versus offset relation seen for the latter group would be expected for a uniform spatial distribution of hypocenters in which waveform similarity slowly decreases with event pair offset because of increasingly different wave propagation paths. The distinct, high β, short-offset group contains the clustered events. The isolation and intensity of this concentrated group was surprising to us, so we studied it in detail.

Fig. 3.2. Cross-correlation measure of similarity, β, verses separation distance (offset) for more than 650,000 event comparison pairs. Permutations of event pairs from 1679 events occurring during the period 1987 to 1992 and separated by 7.5 km or less were used. Earthquakes were located within 5 km of the San Andreas Fault Zone along a 25-km segment centered on the nucleation region of the 1966 M 6 mainshock. Contours show the percentage of event comparison pairs with a given offset having a given β. The gap in the range $0.6 < \beta < 0.9$, 200 m < offset < 500 m generally separates clustered and nonclustered behavior.

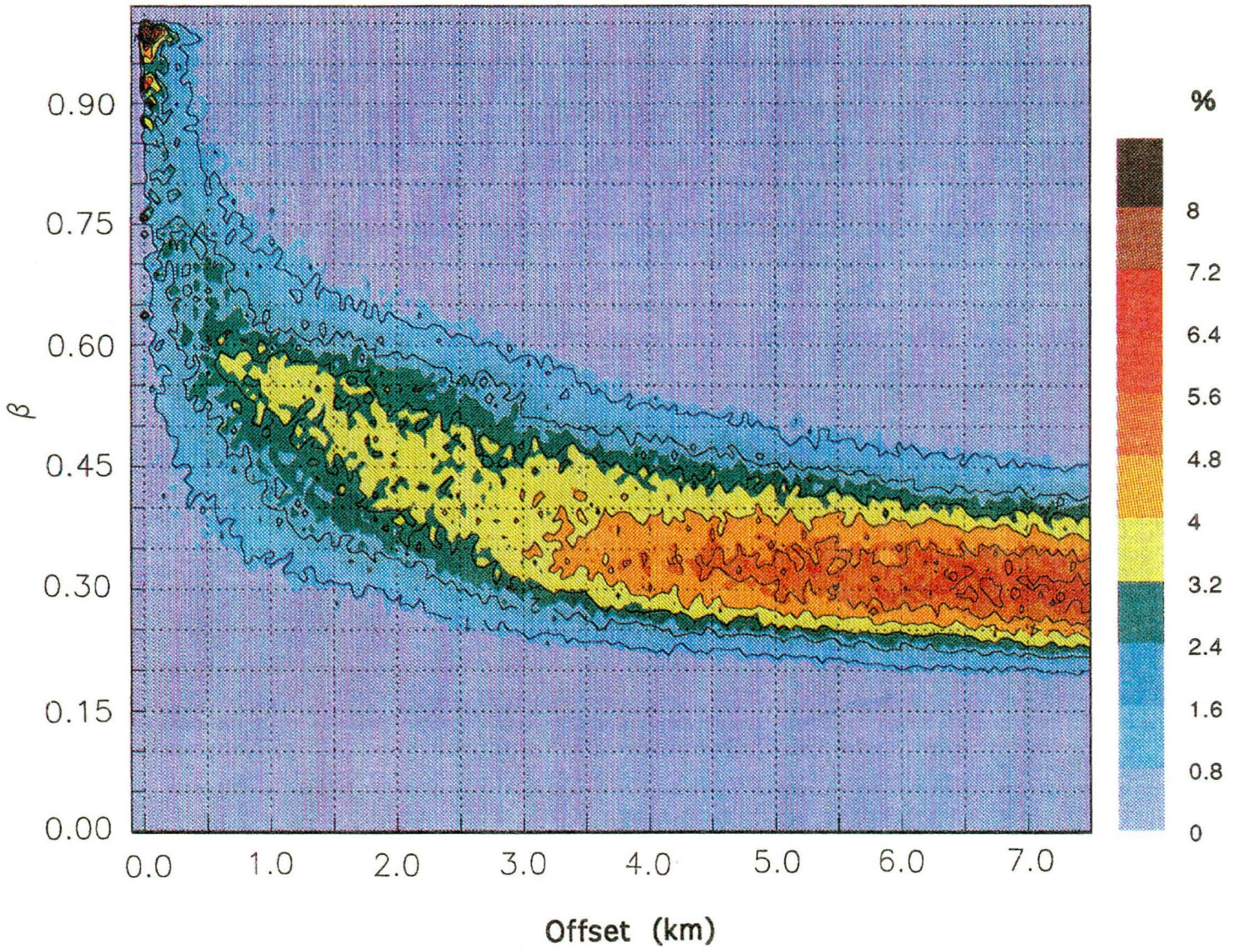
0.90
0.75
0.60
0.45
0.30
0.15
0.00
β
0.0
1.0
2.0
3.0
4.0
5.0
6.0
7.0
Offset (km)
%
8
7.2
6.4
5.6
4.8
4
3.2
2.4
1.6
0.8
0

We selected a similarity measure of $\beta \geq 0.98$ as our criterion for defining cluster members, based on the stabilization of the population within each cluster below this β value. This definition selected 63% of the ~1700 events. These events were found to be organized spatially into 294 small, distinct clusters of 2 to 16 hypocenters that collectively occupy no more than 1% of the active fault surface (Fig. 3.3). Nearly half (43%) of the clusters contained two events (doublets). For clusters of three or more events, 80 to 90% were complex in that their member events could be further subdivided into subgroups (each containing a different event type) on the basis of subtle differences in high-frequency waveforms. Clustering was more prevalent and tended to be more complex for the shallow earthquakes (10).

Fig. 3.3. Sections through the three-dimensional velocity model for Parkfield (4) showing the 294 cluster locations (large dots) defined for $\beta \geq 0.98$, background seismicity (small dots), the 1966 main shock (large square), and recording station names and locations (small triangles) projected onto the fault plane. Depth is kilometers below sea level. The Vp contours and the Vp/Vs anomaly location (dashed contour) are shown.

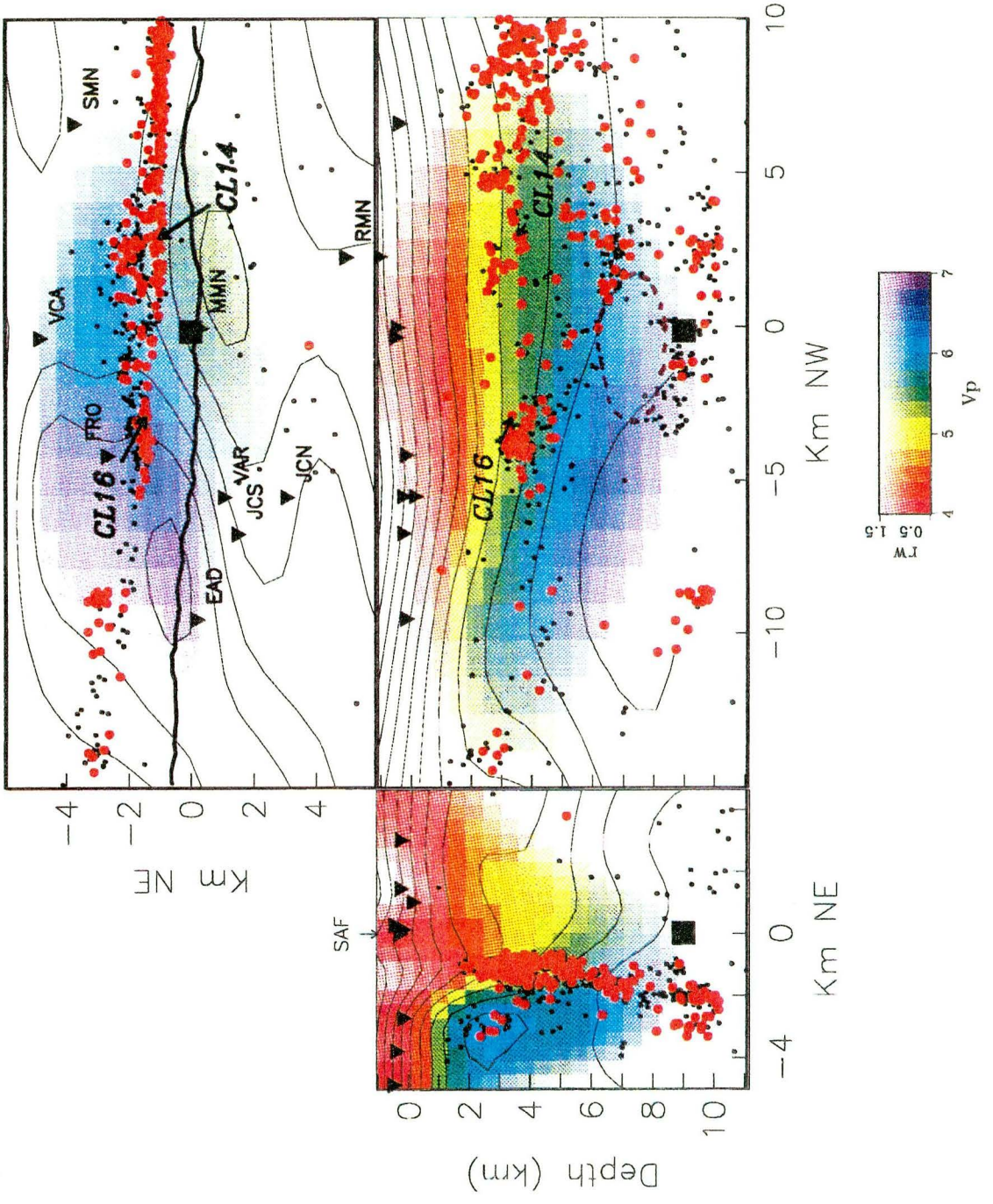
SMN
VCA
FRO
CL16
CL14
MMN
RMN
EAD
JCS
VAR
JCN
SAF
Km NE
Km NW
Depth (km)
Vp
RW
0.5
1.5

SPATIAL DISTRIBUTION OF EVENTS IN CLUSTERS

To investigate the spatial distribution of events within the clusters, we located a representative sample (87 events in 15 clusters) accurately relative to each other by exploiting the similarity of their waveforms (5, 11). This showed that the individual clusters have much smaller dimensions than the 200-m maximum offset for the $\beta > 0.9$ population in Fig. 3.2 (which is based on our routine absolute hypocenter locations). Half of the clustered events in the sample were found to lie less than 10 m from their respective cluster centroids, and all of the events were within 20 m (12). Two shallow clusters, CL14 and CL16 (Fig. 3.3), containing 14 and 16 members, respectively, demonstrate the types of cluster geometries often seen (Fig. 3.4). These are complex clusters, each containing three types of events. In CL14, each type has a characteristic size (Fig. 3.1), spanning about 1.6 in Richter magnitude, whereas the three event types in CL16 are roughly the same size. In both cases each event type appears to occupy a distinct region within the cluster. The clusters define discrete flattened zones, 2 to 5 m thick, of concentrated seismic slip within the fault zone. CL14 is about 35 m long and 7 m wide, with the large events occurring in the upper 20 m of the cluster. CL16 is similar in size, and its event types are organized into groups separated by as little as 2 or 3 m. If we use conventional estimates of rupture dimensions for these earthquakes (6), each of the large events of CL14 involved slip over the entire cluster, even though the centroid of energy release appears to be located at a slightly different position for each event.

Fig. 3.4. Cell geometries for example clusters CL14 and CL16. The coordinate system is oriented on the southeast-northwest fault zone with its origin at the centroid of the cluster. Sections are vertical-plane projections onto and normal to the San Andreas fault. In CL14, the event type is indicated by symbol size, which also represents source strength (larger symbols for greater seismic moment). Events in CL16 are all of approximately the same magnitude.

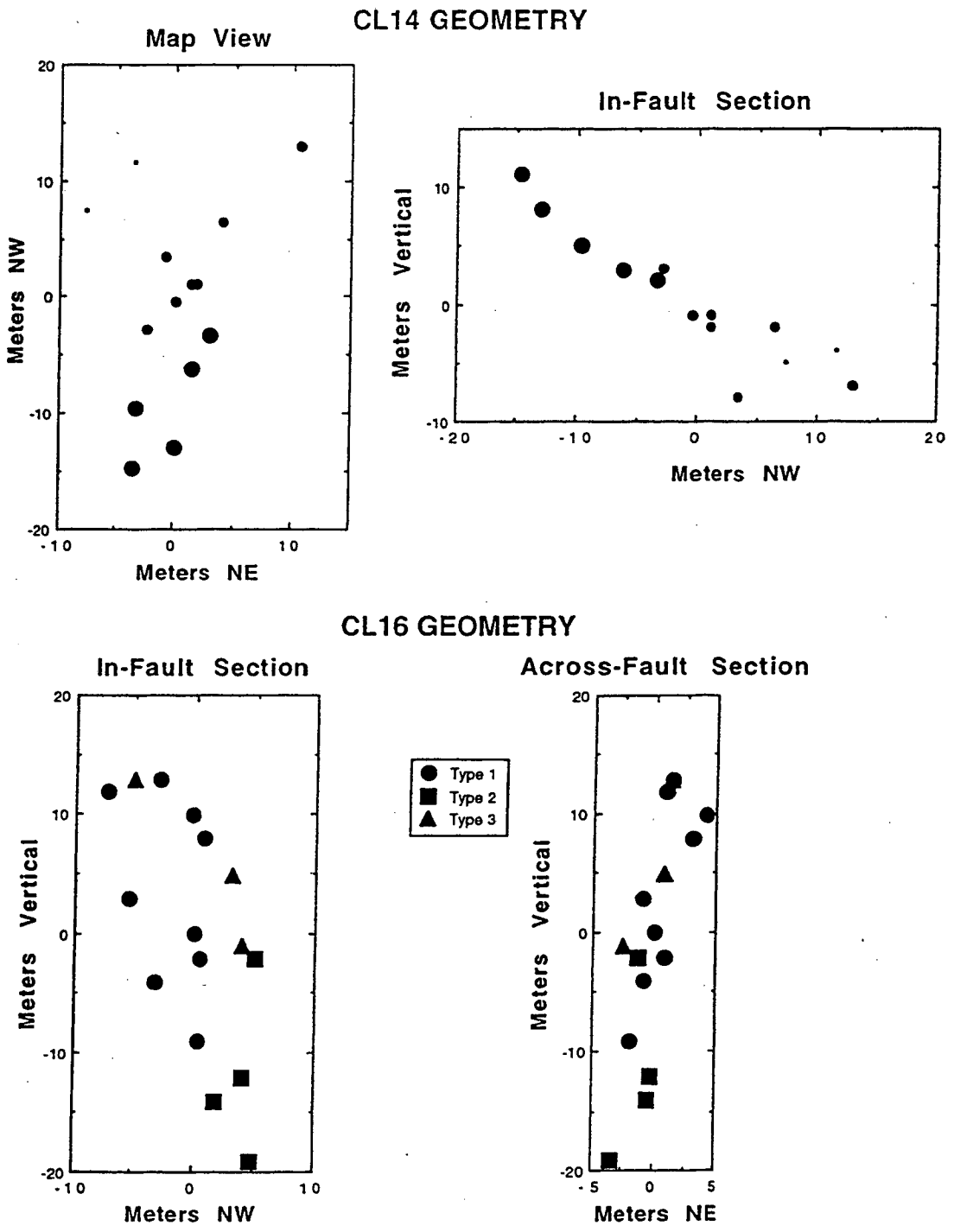
CL14 GEOMETRY
Map View
Meters NW
Meters NE
In-Fault Section
Meters Vertical
Meters NW
CL16 GEOMETRY
In-Fault Section
Meters Vertical
Meters NW
Type 1
Type 2
Type 3
Across-Fault Section
Meters Vertical
Meters NE

INTEREVENT OCCURRENCE TIMES WITHIN CLUSTER SEQUENCES

Another feature of interest regarding events within the clusters was their periodicity in recurrence. We computed the time intervals between successive events (recurrence intervals) in each of the 294 clusters defined by $\beta \geq 0.98$ and found 778 intervals that were bimodally distributed (Fig. 3.5A). Eighteen percent of the recurrence intervals are less than 0.1 year, and most of these are less than 10 min. These intervals are approximately exponentially distributed (Fig. 3.5A, inset), much like a typical aftershock sequence. Recurrence intervals between 0.2 and 2.8 years fit a lognormal distribution, as shown in Fig. 3.5B, with a peak of about 0.8 year. To compare periodic recurrence within these sequences of small earthquakes with recurrence of moderate and large earthquakes (13, 14), we computed the median-normalized recurrence interval, T/T, for each cluster with two or more intervals longer than 0.2 year. The normalized intervals for all such clusters fit a lognormal distribution closely (Fig. 3.5C), as do the normalized recurrence intervals for large and moderate earthquakes (13). The standard deviation of ln (T/T) is referred to as the intrinsic uncertainty in the recurrence interval (14) and is a measure of the regularity of occurrence (15). From Fig. 3.5C. we obtained an intrinsic uncertainty of 0.43, compared with the value of 0.21 used in earthquake forecasting (14). However, as we discuss next, recurrence in a complex cluster is often dominated by one type of event, and when only the dominant events in our representative sample of clusters are considered, the intrinsic uncertainty is much smaller, in the range of 0.03 to 0.2, indicating strongly periodic behavior.

Fig. 3.5. (A) Distribution of intracluster recurrence intervals. The bimodal character of the distribution is shown in the main figure, in which data are plotted in 0.1-year bins. The inset (2.1-min bins) shows details of the distribution of short recurrence intervals, illustrating the peak at intervals less than a few minutes and the approximately exponential fall-off. (B) Fit of the distribution of recurrence intervals greater than 0.2 year (solid) to a lognormal model (dashed). Intervals greater than 2.8 years are undersampled because the database is complete only for about 5.5 years, and all intervals are undersampled to some extent because of equipment malfunctions or imperfect event detection. (C) Distribution of the median-normalized recurrence interval for clusters with two or more recurrence intervals of 0.2 year or greater and lognormal fit (dashed).

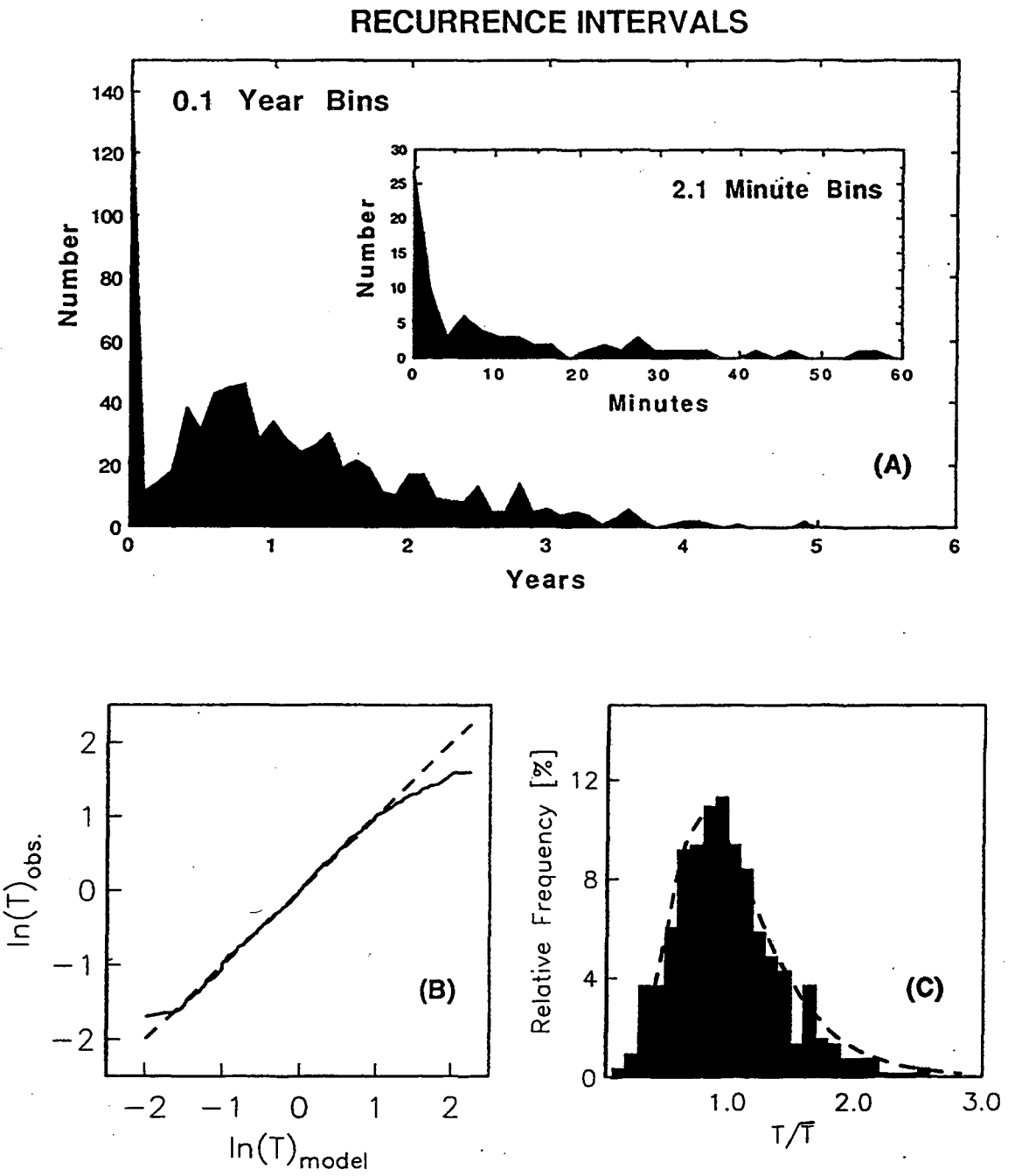
RECURRENCE INTERVALS
0.1 Year Bins
2.1 Minute Bins
Number
Minutes
Years
(A)
(B)
(C)
ln(T)obs.
ln(T)model
Relative Frequency [%]
T/T̄

SUBCLUSTERING

Both short-interval (minutes) and long-interval (months) recurrence traits can be seen in simple plots of cluster event occurrence times (Fig. 3.6). Bursts of near-simultaneous events within complex clusters like CL14 and CL16 invariably involved events of different types; we have yet to observe the near-simultaneous occurrence of events of the same type in a cluster. Events that repeated at intervals of several months, in contrast, were predominantly of one type, although one or more of the other event types in the cluster were often incorporated into the regular sequence as bursts of coincident activity both before and after the dominant repeating event. In CL14 the large-magnitude events dominated the regularity, whereas in CL16 the periodic recurrence pattern (235 ± 25 days, mean ± SD) was produced by the events that fill the central portion of the cell (type 1 in Fig. 3.4). Repeat times between the dominant CL14 events became progressively shorter. Clusters of a single event type usually exhibited higher periodicity than was generally seen for complex clusters, as shown for CL5 (459 ± 16 days) (Fig. 3.6), suggesting that interaction among event types in complex clusters interferes with regularity.

Fig. 3.6. Event chronology patterns for three clusters (see Fig. 3.4 for explanations of symbols). Ordinates for CL14 and CL16 are vertical positions of the events with respect to the cluster centroid. Precise hypocenter locations are not available for CL5, so spatial positions are not given. The open circle in the CL16 plot is a type 1 event that could not be located. Note the periodicities in the largest events of CL14 and in the type 1 events of CL16. CL5 illustrates the strong periodicity seen in noncomplex clusters having events of only one type.

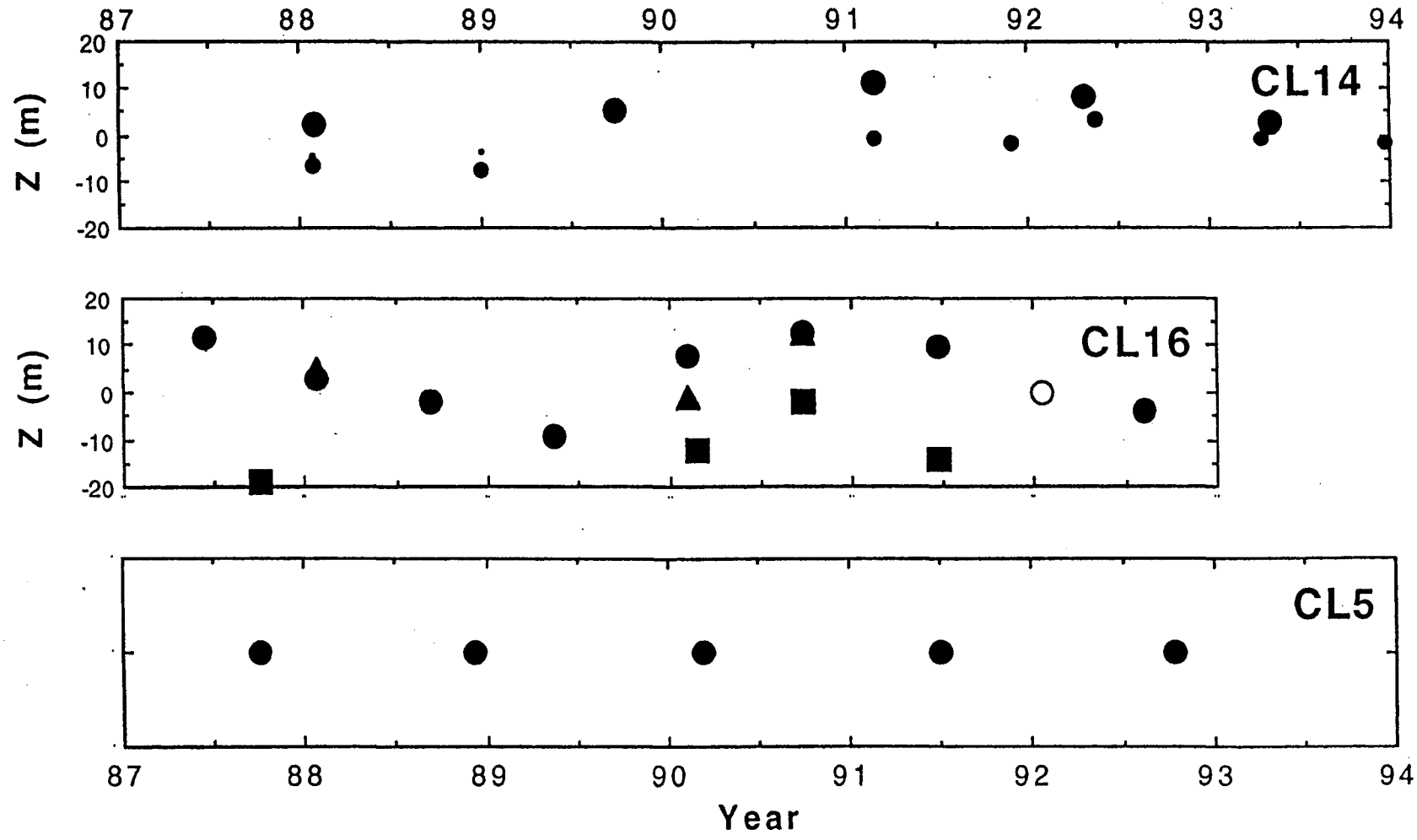
87
88
89
90
91
92
93
94
20
10
0
-10
-20
Z (m)
CL14
CL16
CL5
Year

INDUCED SEISMICITY

The bimodal distribution of recurrence intervals in Fig. 3.5 is for $\beta \geq 0.98$, which corresponds to event-pair offsets of less than 30 to 40 m. To investigate the distributions at larger offsets, we redefined the clusters for gradually decreasing values of β, progressively merging nearby but presumably out-of-phase periodic clusters and causing the gradual disappearance of the lognormal recurrence peak. Near $\beta = 0.93$, a value corresponding to offsets of 100 to 200 m, the number of intervals shorter than 10 min reached a maximum and the bimodal character of the distribution vanished. This indicates that there is communication between earthquakes 100 to 200 m apart on a time scale of several minutes, corresponding to communication at speeds of 10 to 100 cm/s.

DEEP VERSES SHALLOW CLUSTERING

Having found clustering and patterns in recurrence intervals for small earthquakes, we next examined these features in relation to the depth of the seismic activity. Deeper than about 5 km, clusters were less common, contained fewer events on average, and did not exhibit recurrence intervals of less than 10 min, as was generally seen in many shallow clusters. There was more variation among waveforms for deep clusters than for shallow clusters, possibly because of longer, slightly different propagation paths or physical heterogeneity in the cluster volume, although the separations between deep cluster members are similar to those in shallow clusters. Some communication between deep

clusters was evident as sympathetic activity in neighboring clusters at ranges of up to 200 m, but at intervals of hours to days rather than minutes.

TEMPORAL STABILITY OF CLUSTERED AND NONCLUSTERED SEISMICITY

To investigate the temporal stability of the clustering process, we examined characteristics of individual clusters as well as the entire seismicity picture throughout the study period. Significant change was found in some aspects of cluster behavior, along with evidence for high stability in other clusters.

Locations of dominant repeating events appeared to migrate cyclically within the clusters over several years (Fig. 3.6). In CL14, the largest events define one cycle in 6 years, and the dominant events in CL16 define two cycles in the central region of the cluster (Fig. 3.4). If we can assume that these systematic patterns in space and time are genuine, we are viewing the process of fault slip at a scale approaching 2 to 3 m. The relative hypocenter location technique presumes that the P and S wave velocities are not changed by earlier nearby earthquakes or other local processes, and that effects such as meter-scale heterogeneity in source mechanisms or medium properties are negligible (16). An apparent 20-m migration of a hypocenter could be caused by stress-induced travel-time variations of a few milliseconds that would impress the same migration pattern on all event types within the cluster (17). There is some evidence for this in CL16, but it is less pronounced in CL14 (Fig. 3.7). This

phenomenon, if present, would not affect the cluster periodicity or the distribution of event types.

We also examined the change with time in the fraction of seismicity represented by clustered earthquakes (Fig. 3.7). The total number of earthquakes per year increased from 1987 to 1993, but the fraction of all events that were cluster members decreased somewhat, from around 70% of the total to about 60%. The ratio of the number of events deeper than 5 km to the total number of events doubled. The relative sizes of the two peaks in the distribution of recurrence intervals (Fig. 3.5) also changed with time. The population in the short-interval peak was growing with time relative to that in the 0.8-year peak, and the minimum between them at 0.1 to 0.2 year became more pronounced, so that

the increased seismicity was being partitioned into more near-coincident events within existing clusters and more nonclustered deep events. Recent clustering activity at the expected M 6 hypocenter, which had been relatively quiet before 1992, has accompanied two earthquake sequences at depths of 8 to 10 km with mainshock magnitudes of 4.7 and 4.8.

Fig. 3.7. Changes in seismicity by year. The annual earthquake count increased substantially over the period 1987 to 1993, whereas the fraction of the total number of earthquakes that are clustered events decreased during the analysis period (1987ñ92). The fraction of the total activity deeper than 5 km increased significantly. The mode of slip in the fault zone is changing, involving more earthquakes in the deep nucleation zone.

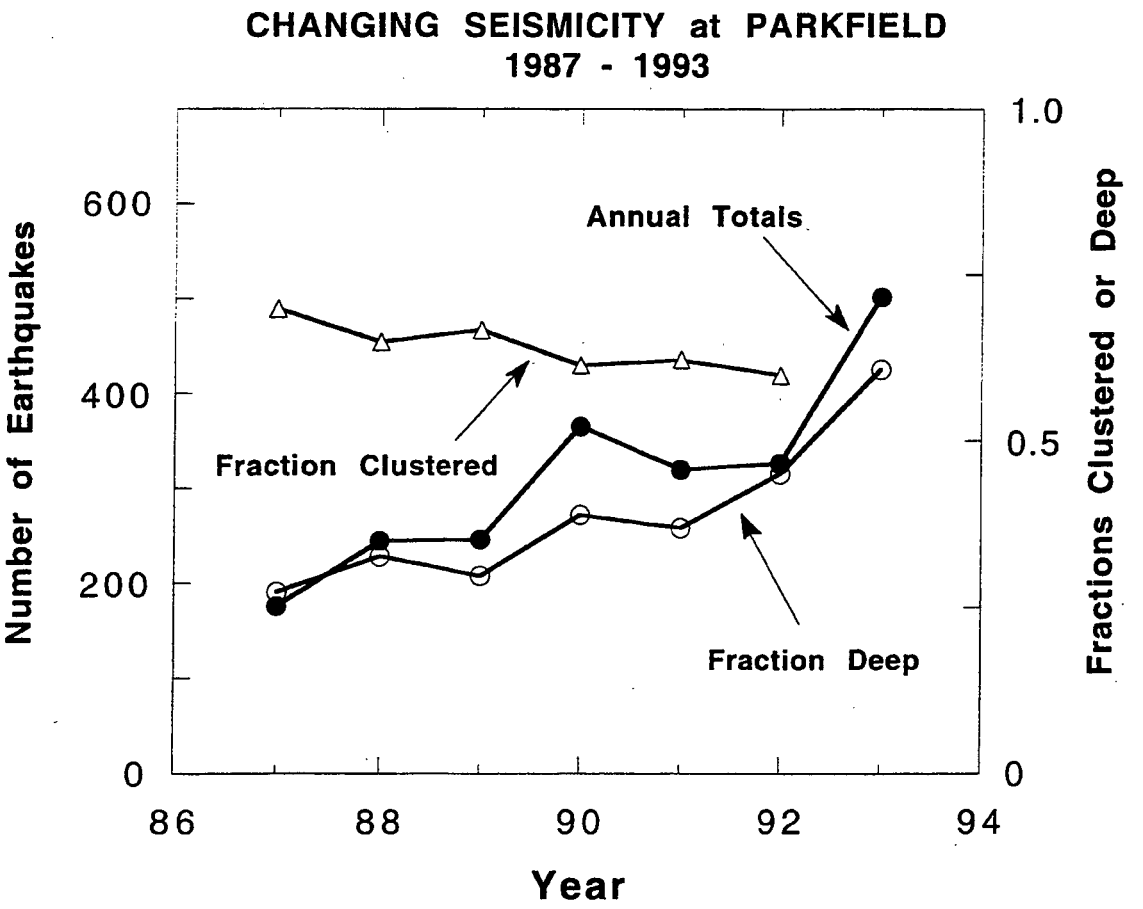
CHANGING SEISMICITY at PARKFIELD
1987 - 1993
Number of Earthquakes
Fractions Clustered or Deep
Annual Totals
Fraction Clustered
Fraction Deep
600
400
200
0
1.0
0.5
0
86
88
90
92
94
Year

During the entire observation period, which represents about 25% of the average M 6 recurrence interval at Parkfield, the local stress state presumably was changing as the fault zone was being loaded by the regional tectonic strain. Despite this, we found no progressive changes in waveform similarity among cluster members that would be indicative of changing material properties within or around the cluster sites. The environment controlling the waveforms thus appears stable to wavelengths comparable with the cluster size, although regularity of occurrence is seen to vary, and both the background seismicity and the distribution of clusters have changed over the larger scale fault zone.

HEALING

In an earlier study of a cluster of small similar earthquakes (M ~ 1.5) in central California, the logarithm of the elapsed time since a previous event was found to be proportional to the seismic moment and to the stress drop of the subsequent event (18). These observations were explained by progressive healing of the fault between events. We examined a group of 11 clusters for evidence of this phenomenon at Parkfield and found no indication of healing. Rather, within clusters we found a pattern of periodic recurrence of similar-size events, modified to varying degrees by interactions with other event types in the same cluster.

PHYSICAL PROCESS

We have considered some intuitively simple processes that might explain

these observed fault zone phenomena: localized seismicity in small clusters, both quasi-periodic and aperiodic recurrence within clusters, sympathetic occurrence of events up to a range of ~200 m, and clustering behavior is not stationary.

The clusters localize more than half of the microearthquake activity onto about 300 small patches, with a total area of <1 km^2 and distributed over the 10 km by 25 km fault zone. These sites represent concentrations in strength or in stress that are related to heterogeneity in the mechanical, thermal, chemical, or hydrological properties of the fault zone. Mechanisms of the microearthquakes are invariably strike-slip motion with San Andreas geometry, regardless of the cluster shape or orientation, indicating that the homogeneous regional stress field controls the slip direction within the clusters. The tendency among the clusters to similar recurrence intervals suggests a common driving mechanism for the periodicity. The simplest mechanism conceptually is frictional stick-slip on cluster patches of constant strength under steady tectonic loading. Alternatively, repeated failure under approximately constant load could occur if the patch strength is modulated locally in a steady-state mode. Near-simultaneous events of differing types within the same cluster are similar to earthquake aftershock sequences but without a defining large-magnitude mainshock. Triggering of events within a range of 200 m in nearby clusters may involve rapid aseismic slip on the fault surface between the clusters. Alternatively, the stress field perturbation from an event in one cluster may be sufficiently intense within a distance of 200 m to induce slip in another cluster. It is difficult to discriminate between these

possibilities.

A possible role for fault zone fluids in the earthquake process has been proposed in general (19), and at Parkfield specifically (20). Common themes involve high pore pressures, rapidly sealing compartments, hydrofracturing, episodic flow, and permeability barriers. Verification of these hypotheses will likely require direct sampling by drilling into one or more of the shallow clusters at a depth of 3 or 4 km (21).

IMPLICATONS FOR NUCLEATION OF THE EXPECTED PARKFIELD M6

Nucleation of the next M 6 event is a steadily evolving process of fault zone deformation that involves periodic recurrence of characteristic microearthquakes that are localized in small clusters. The overall rate of seismicity is increasing, and the fraction of the total seismicity confined to clusters is decreasing. Deeper seismicity is seen to increase markedly with time, whereas activity above 5 km depth appears to be relatively stable. If these trends can be projected, seismicity in the early loading phase is dominated by shallow clustered activity. By the end of the cycle, the increasing seismicity is largely filling zones that were relatively quiet, including the deep site of the impending rupture onset. A rapid decrease in clustering that accompanies increased deep seismicity, therefore, may be an indication of an impending M 6 earthquake.

APPENDIX: COMMENT AND REPLY

Since publication of this chapter as a report in Science (26), the authors of reference 18 (Vidale et al.) have submitted a comment which contends that our duplication of their analysis ('HEALING' section this chapter) was done incorrectly. We submitted a reply and, subsequent to peer review, Science decided against publishing the comment. Nonetheless, the issues raised in the exchange are important and subtle enough to justify a short discussion which I present below.

The comment of Vidale et al. contends that we lack the sensitivity to see the patterns they observe, since in our analysis we mixed earthquakes that repeatedly rupture the same fault patch with earthquakes that break adjacent segments of the fault plane. Implicit in this criticism is the assertion that they successfully discriminate between adjacent and repeating fault patch rupture. We showed (26) that spatial clusters of almost identical earthquakes, defined according to a very strict criterion of similarity, can be subdivided further based upon subtle yet systematic differences among their waveforms. We suggested, based upon the relative locations of the events, that these subgroups may rupture adjacent patches of the fault or that overlapping patches may rupture with discretely different rupture histories.

The assumption by Vidale et al. that the earthquakes used in their analysis

repeatedly rupture the same patch with essentially identical rupture histories implies that such differences should not exist in the waveforms of their events. In fact, the variations among their repeating events are much greater than variations present among members of the clusters we define. Reference 22 contains a set of similar seismograms taken from 18 events they report as having ruptured the same fault patch identically. These seismograms are far more variable than the seismograms we used in our study (e.g. Fig. 3.1). Therefore, based on the similarity of seismograms, the assertion of Vidale et al. that our more similar seismograms include earthquakes rupturing adjacent fault patches, requires the same possibility for their events. However, whether the subgroups of repeating events observed in most of the spatial clusters we define are ruptures on discrete adjacent fault patches (as claimed by Vidale et al.) or are ruptures on the same or overlapping patches with slightly different rupture histories remains unclear, since the dimensions of the region occupied by each cluster approach the limit of spatial resolution in the relative location method used in either study.

Vidale et al. assert that their earthquakes are identically repeating ruptures based, primarily, on the observations of localization to a 20m dimension for their event locations. This criteria is inadequate for two reasons. First, we commonly observe non-repeating rupture for events of magnitudes comparable to theirs to be separated by no more than ~10-15m (Fig. 3.4). Second, in contrast to our analysis, Vidale et al. do not use a constant station set in their relative location determinations. Since they never explicitly show their locations, it is not possible to assess their accuracy,

but it has been our experience that the use of a heterogeneous station set will introduce sufficient location scatter to mask systematic spatial separations between the locations of non-identical ruptures. Hence, the analysis of Vidale et al. (18) most probably does not discriminate between repeating and adjacent patch rupture when, as is usually the case, both exist.

In order to duplicate the analysis of Vidale et al. (18) we employed a similar selection criteria to theirs -- earthquake localization to ~20m dimension -- despite the fact that by this criteria systematically different event types, or ruptures on adjacent or distinct overlapping patches are often included into the analysis. The inconsistent results we report in our analysis of 11 different sequences may have resulted from the inclusion of these different event types into the analysis. Several lines of evidence suggest, however, that the events used by Vidale et al. (18) also contain systematically distinct earthquake types and that their results appear consistent because only one sequence was analyzed:

1) A second repeating sequence analyzed by three of the same authors (23) exhibits recurrence time - moment dependence opposite to that of study (18). Furthermore, the repeating events in (23) show considerably greater range in size, which further supports our contention that their selection criterion does not differ significantly from ours.

2) In our data, spectral ratios between repeating ruptures are observed to

be flat to beyond 50-80 Hz. Ratios between different event type ruptures remain flat or moderately varying -- similar to that reported in Vidale et al. (18) -- out to 20 Hz only. Beyond 20 Hz, and above the bandpass of the Vidale et al. data, considerable spectral variability exists. This suggests that the spectral resolution needed to discriminate between same event type and different event type ruptures and to identify spectral corner frequencies was not present -- as asserted -- in the Vidale et al. study (18). (Fig. 5, (24)).

3) We have superposed the distributions of occurrence time intervals used in this chapter and in (18) (Fig. 3.A1, this appendix). Both distributions have bimodal shapes, with a short-interval spike and a broad spread of longer time intervals. Short intervals are minutes to months in our study and days to months in (18). Long time intervals are roughly the same for both populations. The similarity in the shapes of the two distributions suggests that they represent similar underlying processes. It seems, therefore, that the set of events from the single cluster used by Vidale et al. (18) is no more valid a basis for investigating relationships between recurrence interval and source parameters than are the sets of events from the several clusters used in our test of their result.

Truly repeating events are essentially characteristic and so have a strong affinity toward quasi-periodic recurrence. This, however, makes it difficult to obtain the mix of short and long recurrence intervals needed to accurately test for increasing moment with asperity contact time. Fortunately, the mechanical complexity associated with the transition from

locked to creeping behavior at Parkfield appears to give rise to some localized time variability in slip at depth. Evidence for this is reflected in the systematically evolving recurrence intervals of repeating identical events observed under station FRO (see chapter V). As we accumulate a larger data set with longer repeating event sequencies that span the occurrence of recent, slip enhancing, magnitude 4+ and 5 events, it should be possible to carry out a more complete investigation of the dependence of seismic moment on recurrence time using repeating identical events only.

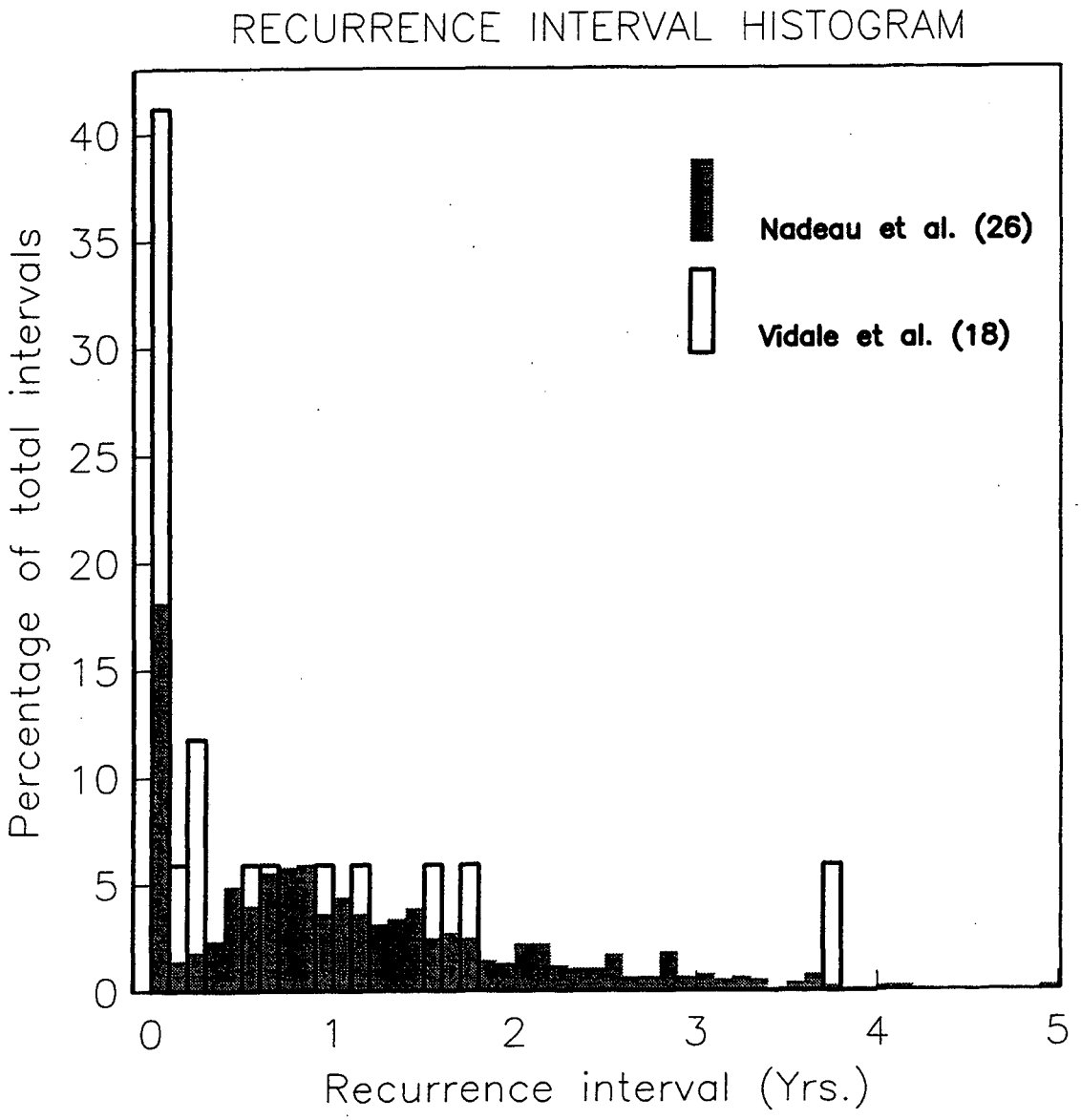

Fig. 3.A1. Superposed intra-cluster occurrence time separation intervals for the sequence reported on in (18) (framed bars) and for all 294 sequences reported on in this chapter (shaded bars).

REFERENCES AND NOTES

1. Y. Kagan and D. D. Jackson, J. Geophys. Res. 96, 21419 (1991); J. McCloskey and C. J. Bean, Science 266, 410 (1994).

2. W. H. Bakun and T. V. McEvilly, J. Geophys. Res. 89, 3051 (1984).

3. W. H. Bakun and A. G. Lindh, Earthquake Predict. Res. 3, 285 (1985).

4. A. Michelini and T. V. McEvilly, Bull. Seismol. Soc. Am. 81, 524 (1991).

5. R. Nadeau, M. Antolik, P. Johnson, W. Foxall, T. V. McEvilly, ibid. 84, 247 (1994).

6. Source parameters conventionally estimated from the source spectrum of a typical small event are as follows: magnitude ~0.5, seismic moment ~0.5 ¥ 1017 dyne cm, source radius 5 to 10 m (10 to 20 m for M ~ 1.5), and stress drop 3 to 10 MPa.

7. The frequency spectrum of the P or S wave displacement is flat at low frequency and decreases exponentially beyond the corner frequency because of interference due to the finite source. A similar spectral roll-off will be introduced by the source rise time, which is the duration of the slip at a point. Anelastic attenuation due to medium properties also produces high-frequency spectral decay that can mask high corner frequencies, although spectral ratios for co-located events should eliminate this effect.

8. R. C. Aster and J. Scott, Bull. Seismol Soc. Am. 83, 1307 (1993).

9. D. Knuth, Fundamental Algorithms, The Art of Computer Programming (Addison-Wesley, Reading, MA, 1968).

10. About 75% of the events above 5 km depth are members of clusters, representing 44% of the total centers of activity (cluster sites plus non-clustered events), compared with only about 40 and 20%, respectively, for the deeper events.

11. M.-J. Fremont and S. D. Malone, J. Geophys. Res. 92, 10223 (1987).

12. These distances approach the spatial resolution of the analysis, so that at least some of the events in clusters may be co-located. Unlike a conventional hypocenter determined from arrival times, which is the point of rupture nucleation, each of these relative locations corresponds to a centroid of seismic moment release, because the cross spectra of entire P

or S waveform pulses are used to estimate the time delays between the event arrivals.

13. S. P. Nishenko and R. Buland, Bull. Seismol. Soc. Am. 77, 1382 (1987).

14. Working Group on California Earthquake Probabilities, U.S. Geol. Surv. Circ. 1053 (1990).

15. An intrinsic uncertainty value of 0 means perfect time predictability. A value of 1 means that the normalized recurrence intervals describe a Poissonian process where recurrence times are not predictable (14).

16. Two observations support these assumptions. First, pairs of events from different event types occurred only a few minutes apart in either order, with no measurable effect of the first event on the waveform character of the second. Second, events of different event types in a cluster sometimes were separated by distances much smaller than separations between events of the same type [for example, CL16 (Fig. 3.4)].

17. Progressive travel-time variations of this magnitude have been reported at Parkfield [E. Karageorgi, R. Clymer, T. V. McEvilly, Bull. Seismol Soc. Am. 82, 1388 (1992)].

18. J. E. Vidale, W. L. Ellsworth, A. Cole, C. Marone, Nature 368, 624 (1994).

19. M. L. Blanpied, D. A. Lockner, J. D. Byerlee, ibid. 359, 574 (1992); J. Byerlee, Geology 21, 303 (1993); P. Gavrilenko and Y. Gueguen, Tectonophysics 217, 91 (1993); A. H. Lachenbruch, J. Geophys. Res. 85, 6097 (1980); P. R. Sammonds, P. G. Meredith, I. G. Main, Nature 359, 228 (1992); R. H. Sibson, Tectonophysics 211, 283 (1990); A. Nur and J. Walder, in Fault Mechanics and Transport Properties of Rocks, B. Evans and T.-F. Wong, Eds. (Academic Press, San Diego, CA, 1992), chap. 19; J. R. Rice, ibid., chap. 20; N. H. Sleep and M. L. Blanpied, Nature 359, 687 (1992); U.S. Geol. Surv, Open-File Rep. 94-228 (1994).

20. P. A. Johnson and T. V. McEvilly, J. Geophys. Res. 100, 12937 (1995).

21. S. Hickman, M. Zoback, L. Younker, W. Ellsworth, Eos 75, 137 (1994).

22. W. L. Ellsworth, Characteristic earthquakes and long-term earthquake forecasts: Implications of central California seismicity, Urban disaster mitigation: The role of engineering and technology (Elsevier Science, Ltd., Oxford, U.K., 1995).

23. C. J. Marone, J. E. Vidale, W. L. Ellsworth, Geophys. Res. Lett., in preparation.

24. M. Antolik, R. M. Nadeau, R. C. Aster, T. V. McEvilly, Bull. Seism. Soc. Am., in press (1995).

25. J. Dieterich, J. Geophys. Res. 99, 2601 (1994).

26. R. M. Nadeau, W. Foxall, T. V. McEvilly, Science 267, 503 (1995).

27. This chapter was published as an article in Science and was co-written with William Foxall, and Thomas V. McEvilly. The Parkfield High-Resolution Seismic Network functions through close cooperation among researchers at the University of California at Berkeley, Lawrence Berkeley Laboratory (LBL), Duke University, and the U.S. Geological Survey (USGS). USGS provides financial support for this research through NEHRP award 14-08-0001-G1703. Data processing was done at the Center for Computational Seismology at LBL, which is operated by the University of California for the U.S. Department of Energy under contract No. DE-AC03-76SF00098.

2 September 1994; accepted 28 November 1994

CHAPTER IV

Scaling from Microearthquakes to Large Earthquakes: Similarity of Recurrence Statistics and Implications for Fault Mechanics and Seismic Hazard.

INTRODUCTION

Relations of scale between earthquakes ranging in seismic moment (M_o) from ~10^{19} to ~ 10^{30} dyne-cm have been studied extensively and equations relating various source parameters are commonly used (1, 2),

$$M_o = GuA \qquad (e1)$$

$$M_o = (1/C)(\Delta\sigma\Lambda)A \qquad (e2)$$

$$\Delta\sigma = CG(u/\Lambda) = C(G/\Lambda)u \qquad (e3).$$

Here G is the shear modulus; C is a constant that depends on the geometry of rupture; A is the fault area; u is the mean static slip averaged over A; $\Delta\sigma$ is the average static stress drop; and Λ is a characteristic rupture dimension, such as the radius of a circular rupture surface.

Much controversy exists over the appropriateness and proper application of these relations to events with M_o less than ~ 10^{21} and greater than ~ 10^{25} dyne-cm. Resolution of these issues is important for understanding the mechanics of earthquake nucleation and faulting, and for scaling laboratory results and microseismicity patterns to large damaging earthquakes. Microearthquakes (M_o <10^{21}) are of particular interest

since they occur in great abundance and have sources widely distributed in depth and along strike which frequently surround large locked asperities .

However, for microearthquakes, measurements of source dimension, slip and stress drop can only be estimated by indirect means. Typically, earthquakes of this size are assumed to rupture a circular patch and Brune-type models (3) are used to relate observables in the radiated elastic wave to a time-history of slip. In such models the displacement spectral corner frequency, f_c, is assumed to be proportional to the inverse of the rupture duration which, in turn, is assumed to be approximately equal to the rupture velocity divided by the radius of the circular rupture. The radius is considered the characteristic rupture dimension so that from the measurement of seismic moment and rupture radius one can estimate stress drop and mean slip using equations (e1-e3) -- after having assumed reasonable values for G (typically 3 X 10^{11} dyne/cm^2) and C ($7\pi/16$).

Source parameters derived in this way, however, depend critically on an accurate determination of the characteristic dimension, Λ, because for circular rupture (where $\Lambda = a$), $A = \pi a^2$ so that equations (e1) and (e2) become functions of a^2 and a^3 respectively,

$$M_o = G u \pi a^2 \qquad \text{(e4)}$$

$$M_o = (16/7)\Delta\sigma a^3 \qquad \text{(e5).}$$

It is still unclear, however, whether the corner frequencies measured from

spectra of microearthquakes are truly representative of rupture radius (Brune personal communication, 1995; 1; 4). Various observables related to source dimension -- f_c, pulse widths, and rise times -- generally indicate that source dimension remains nearly independent of M_0 for events smaller than about 10^{19} dyne-cm (1, 4, 6, 7), and measurements of Parkfield microearthquakes appear to be no exception (Fig. 3.1; Fig. 4.1). If these measurements are truly representative of source dimension, their constancy indicates a lower limit to asperity size. It follows, then, that since M_0 has no lower observational limit, stress drops will decrease without limit for ruptures of this minimum-size asperity.

On the other hand, many investigators argue that the apparent threshold of asperity size is a manifestation of near-surface attenuation of seismic waves (5, 9, 10) or that it occurs when small event source corner frequencies exceed the high-frequency cutoffs of the seismometers (Abercrombie, personal communication, 1995; Fig. 2.9 and related discussion). Spectral corner frequencies may also be affected by high frequency source directivity (11, 12), site-specific resonance (13) or near-surface scattering (14). This multiplicity of interfering spectral effects, particularly for small earthquakes and at high frequencies, makes it unlikely that reliable values of source dimension, stress drop and slip can be estimated using spectra. To establish source parameter scaling relationships, then, between very small and larger damaging earthquakes, other observables must be sought.

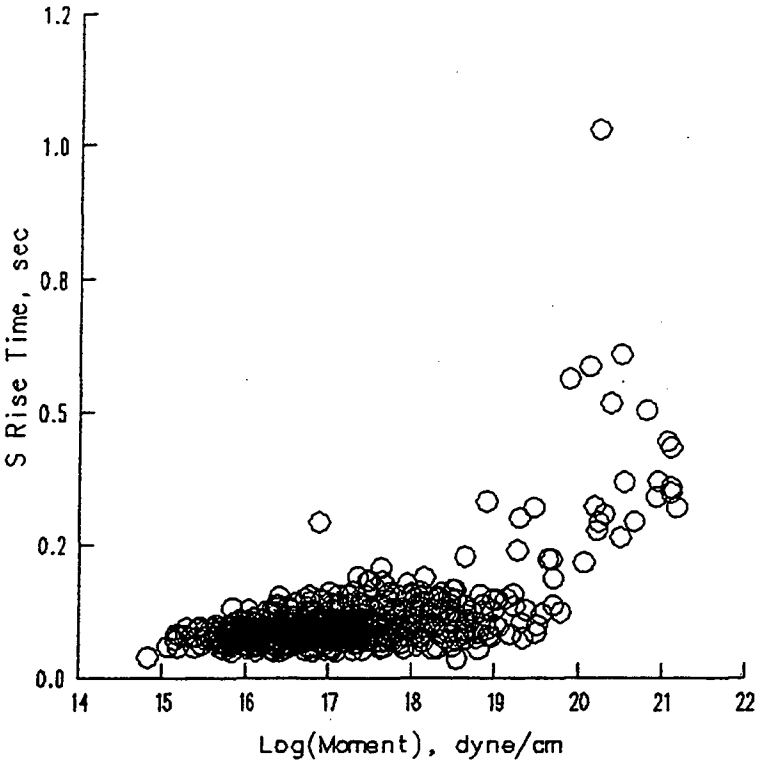

Fig. 4.1 Station averaged S rise times, (determined from horizontal component pulse widths) verses seismic moment (estimated from the three-component seismic moment tensor (72) using P and S wave amplitudes) for all reporting stations and components of 1650 Parkfield microearthquakes occurring between mid-1991 and 1994 (inclusive) and within the 25 km study zone defined in Chapter III, (Fig. 3.3). Note the lack of dependence of the S-rise times on seismic moment below $Mo \cong 10^{19}$ dyne-cm.

Large numbers of characteristic earthquake sequences -- groups of events that occur on the same asperity, with similar rupture histories, sizes, seismic slips, and with quasi-periodic recurrence-times (61) -- spanning a wide range of sizes have been reported (26, 27, 28, 29, 62, 70, 76, 80) suggesting T -- the average recurrence-time between repeating events -- to be a suitable parameter for use in earthquake scaling. Assuming a steady state in which the sum of seismic slip on an asperity over time balances (or is proportional to) the integrated tectonic strain loading rate, the average seismic slip per event, u, of a characteristic sequence equals (or is proportional to) the product of the average fault slip rate, V, and T (60) so that, on average, for each event in a characteristic sequence,

$$u = VT \quad (\text{or at least } u \propto VT) \qquad \text{(e6)}.$$

where, at depth the average slip rate, V, is usually inferred from surface measurements while T is accurately determined from relative occurrence times.

Equation (e6) has found much utility in seismological studies (29, 47, 62, 73, 75) and has been accepted as a basic postulate in seismology. The repeating mainshock or "characteristic earthquake" hypotheses (20, 61) is still controversial, however (21, 22, 23, 24, 29, 61), but the phenomenon is real (see Chapter III, 25, 26, 27, 43, 62, 80). Using these two assumptions, $\Delta\sigma$, Λ, and A can be estimated for repeating earthquakes using (e1-e3). Furthermore, they can be scaled, independent of spectra, provided a systematic relationship between the characteristic size and recurrence times of repeating earthquake sequences (M-T) can be established. The scaling can also be extended to non-recurring events by assuming a

common physics of rupture.

Another advantage of using T as a scaling parameter is that it could potentially be used to unify two other fundamental scaling laws -- the Gutenberg-Richter (GR) frequency-size distribution and the 1/t Omori law decay -- which could significantly improve earthquake hazard estimates. Specifically, recent work (15) has indicated that T can be a predictor of a repeating event's foreshock and aftershock seismicity and decay rates suggesting that, in conjunction with a M-T scaling and work relating mainshock size to foreshock and aftershock size-distributions (16, 17), hazards associated with the entire mainshock event ensemble -- foreshocks, mainshocks, compound events and aftershocks -- might be predicted from characteristic mainshock size or recurrence-time or by scaling up mainshock ensemble parameters of smaller more frequently recurring mainshock ensembles.

However, theory relating GR, Omori-like 1/t statistics, and ensemble activity to mainshock recurrence-time is largely based on observations of events of magnitude ≥ 3 (i.e. $M_0 > 10^{21}$). Therefore, I begin the body of this chapter with an initial review of GR and rate dependent seismicity theory, and follow it by a report of microearthquake observations from the Parkfield High Resolution Seismic Network to demonstrate the applicability of theory to the micro-earthquake scale (magnitudes -0.5 to 2). In the process, two important properties of the Parkfield microseismicity (i.e. depth dependence and non-stationarity) are discussed with regard to their implications for fault zone mechanics, earthquake hazards, prediction

and scaling.

Following this discussion, I establish an empirical M-T relationship for California strike-slip earthquakes using currently available characteristic sequences ranging in seismic moments from ~10^{15} to 10^{28} dyne-cm. I then discuss the implications of the M-T for the constant stress drop case and derive a series of source parameter scaling relationships based on the M-T results. The relationships are unconventional and call for a reevaluation of established models of scaling, source mechanics and conditions at depth. In the final section of the chapter I show how the combination of quasi-periodic recurrence-times and an M-T can affect the GR statistics to provide an alternative explanation for reported slope variations in GR and decreasing B-values prior to large events. Current models attribute these to either characteristic earthquake behavior, brittle-ductile transition depths or an increasing average fracture size.

GUTENBERG-RICHTER SCALING OF EARTHQUAKE SIZE DISTRIBUTION

Traditionally, the fundamental scaling relationship between earthquake size and relative number (frequency) has been the Gutenberg-Richter (GR) or power-law relationship (19) commonly expressed in terms of either magnitude,

$$\log(N) = z - bm \qquad \text{(e7a)}$$

where N is the cumulative number of events of magnitude m or greater

and z and b are constants, or (using the moment- magnitude relationship of Hanks and Kanamori (82)) as seismic moment,

$$N(M_o) = aM_o^{-B} \qquad \text{(e7b)}$$

where a and B are constants and $N=N(M_o)$ is the cumulative number of earthquakes of moment $\geq M_o$ occurring during a given period of time and within a defined region. The GR distribution is used extensively in the assessment of earthquake hazards and has found popularity among modelers of fault zone dynamics as a target size distribution (35, 36). This type of power-law relationship arises from the self-similarity of earthquakes where B can be related to a self-similarity dimension (37, 38, 39). Since fracture is also a self-similar process, the sizes of faults and joints also obeys a power law distribution (40, 41, 42) so that the M_o and fracture distributions are probably related. Not surprisingly, then, variations of B in space and time are frequently interpreted in terms of varying fracture size though, as I will show, the fracture size interpretation can be in error if significant numbers of characteristic earthquakes exist over a wide size range and new non-recurrent fracturing is taking place (see last section this chapter).

RATE DEPENDENCE IN EARTHQUAKE SEQUENCES

Omori law for Aftershocks:

Another well-defined aspect of seismic behavior indirectly related to earthquake size is the Omori Law (18),

$$n(t)=p/(s+t) \qquad \text{(e8)}$$

where n(t) is the occurrence frequency of aftershocks at time t after the mainshock, and p and s are constants such that p/s is the seismicity rate

immediately following the mainshock. The Omori decay law contains no magnitude dependence; however, previous observations (30, 31) and recent empirical and theoretical work (15, 16, 17) indicate that aftershock size distributions can be related to mainshock size and that both seismicity rates and decay times can be related to mainshock recurrence-times, T.

Foreshock-Mainshock-Aftershock Ensemble:

A general 1/t dependence of foreshock seismicity rates has also been observed (32),

$$n(t) = at^{-\omega} \qquad \text{(e9)}$$

where t is the time before the origin time of the mainshock, n(t) is the frequency of foreshocks and a and ω are constants (ω close to 1). Furthermore, from a study of southern California eathquakes showed that the magnitudes of mainshocks follow a normal GR distribution above the magnitude of their foreshocks (33). Statistics of sequences of worldwide multiple or compound earthquakes -- two or more events often of similar size occurring on nearby rupture surfaces close together in time -- also show distributions with 1/t seismicity decay and dependence on average mainshock recurrence-time, T (15, 34). The ensemble of earthquakes surrounding a repeating mainshock, then, all seem to exhibit the same 1/t decay in seismicity rate and according to theory (15,16,17), have size distributions which are predictable and can be modeled using the GR relationship (In their treatment Reasenberg and Jones; and Jones (16, 17) consider compound events to be a part of the foreshock and aftershock sequences).

OBSERVATIONS AT PARKFIELD

Seismicity Rates:

For the most part, rate studies (15, 16, 17) have considered earthquakes with M_o >~10^{21}. However, 1/t decay is also well represented in the clustered microseismicity observed at Parkfield (3.5A inset), The small and sometimes comparable sizes of events in clusters and their commutative triggering -- the variable order in occurrence of foreshock and aftershock events about repetitions of a mainshock -- makes it difficult to distinguish between foreshocks, aftershocks, compound events and mainshocks in this context, and investigations of scaling appears, at first, to be impractical. Fortunately, theory has shown a similar ~1/t decay rate for all ensemble event types, allowing us to study their decay without differentiating amoung them. It is then possible to scale seismicity rates and decay times of the mainshock ensemble with mainshock size or recurrence-time over a very wide range of moments (M_o ~10^{15} to ~10^{28} dyne-cm).

As a test, consider the recurrence-time distribution of the Parkfield microearthquakes presented in Chapter III (Fig. 3.5A). This distribution is bimodal with the short interval peak exhibiting the characteristic 1/t decay envelope of foreshock-aftershock sequences. It is characterized by the duration decay time, t_a, which represents the time before and after a mainshock for foreshock and aftershock seismicity rates to achieve background levels. For Parkfield microearthquakes, t_a has a typical value of about 30 days. The second broadly peaked mode of Fig 3.5A reflects the quasi-periodic recurrence-time behavior of repeating sequences in the

cluster population and is centered at about 1 year. Taking 1 year as a typical recurrence-time of a characteristic microearthquake sequence, T, and the typical characteristic duration decay time of ta = 30 days we arrive at a T/ta ratio of ~ 12.2 which, from Fig. 3 of Dieterich (15), is consistent with ratios of larger event ensembles (main shock magnitudes 4.8 to 9.2) whose T/ta ratios generally lie between 10 and 50. This suggests that the dependence of aftershock duration on recurrence time extends from the microearthquake scale to large damaging event ensembles and that, given an established M-T, parameters derived from repeating microearthquake ensembles might be scaled to estimate seismicity rates and decay for large repeating ensembles prior to their anticipated mainshock. In addition, microearthquake-derived parameters might also provide important information on conditions of stress, friction and source-dynamical processes at depth (15).

Gutenberg-Richter Statistics:

The difficulty in discriminating between foreshocks, mainshocks, compound events and aftershocks within cluster ensembles is more problematic for scaling ensemble size distributions. However, the GR statistics of the entire microearthquake data set are consistent with results of multiple-fault GR distributions using larger events. This is true despite the predominantly clustered and recurring seismicity of the microearthquakes, and it supports the arguments that size scaling of mainshock ensemble distributions continue down to the microearthquake level and that similar patterns of clustering and recurrence between microearthquake and large event ensembles might be expected given

comparable relative observation periods and analysis resolutions.

Consider the seismic moment expression of the GR (e7b) for Parkfield microearthquakes shown in Fig. 4.2A. Here $N(M_o)$ vs. M_o is normalized to yearly rate from a 7 year microearthquake catalogue (1988-1994 inclusive) the characteristic Parkfield M6 occurrence rate is normalized based on its 21.5 year average recurrence-time (43). The curve rolls off for $M_o \leq 10^{17}$ and $M_o > 10^{21}$ because of perceptibility and the exclusion of severely clipped events from consideration HRSN severely clips at all stations for events larger than about $M_o \sim 10^{20}$). The slope of the regression line for the linear portion of the curve -- 0.54 -- is a relative measure of the number of small events to large events in the study area. The goodness of fit of the data to a straight line, is an indication of how self-similar the seismic process is for the moment range considered. For large non-fault-specific cases, the fit to a straight line is generally quite good, and the regression slope from small events usually around 0.667 (1).

The intercept of the straight line fit to $N(M_o)$ = [1/(largest event recurrence-time)] -- generally modeled as the largest sized event to occur in the sampled region -- is only 6×10^{23} dyne-cm and seriously underestimates the expected size of the repeating Parkfield M6 (1.26×10^{25} dyne-cm) (81). Previous authors have attributed such behavior in other fault-specific cases to a variety of effects: 1.) an inadequate spatial sampling (71), 2.) A 1.5 magnitude gap between mainshock magnitudes and largest aftershocks magnitudes (47, 76), 3.), a break in the self-similarity between

small and large events (associated with the brittle-ductile transition depths and rupture geometries) (1), or 4.) the regional stress control exerted by the largest event on a fault under fault-specific conditions (47). It is also possible that temporal under-sampling of seismicity can result in the observed under-estimations if (as is usually the case) the duration of the seismic catalogue is less than one seismic cycle (43) and either significant non-stationarity or a large fraction of small characteristic sequences, obeying an M-T relationship, exist. Both these conditions are present at Parkfield and their respective effects on the GR distribution, along with an alternative explanation for the GR underestimation of largest event sizes, will be discussed in the last section of this chapter.

Spatio-temporal variations in GR at Parkfield:

In general, observations of increased seismicity and decreased B-values prior to large events (17) and the lower B-values observed for known foreshocks (44) correlate with results of experimental lab studies which show that acoustic emission increases and its B-values decrease prior to rock fracture (48, 49). These observations have been interpreted as indicating that the average fracture size and fracturing rate within a rock mass increase as gross failure is approached (1), and that dilatant processes are at work during the earthquake nucleation phase.

At Parkfield, seismicity rates and B-values (manifest in the GR) are observed to vary with depth (Fig. 4.2B). For example, from 1988-1994 about 40% more earthquakes occurred above 5 km depth than below that depth (Fig. 4.2B) with corresponding B-values of 0.58 and 0.46

respectively. Furthermore, most of the larger events since the beginning of HRSN operation ($M_0 \geq 10^{21}$ (~ m3)) have occurred below 5 km. The greater number of shallow events could be due to a greater average slip rate (consequently shorter recurrence-times) observed above 5 km (50), and the variability in the B-values could be explained by a greater average fracture size below 5 km. Alternatively, the greater number of large events at depth may reflect stronger deep asperities resulting from greater effective normal stress, as expected from a frictional model of faulting (1). In any case, the observed depth dependence of GR for microearthquake events should be taken into account when applying scaling relationships to microearthquakes, and the systematics suggest that depth-varying mechanical conditions might be derivable from microearthquake observations.

Temporal changes in GR at Parkfield are also observed. Some of these changes are illustrated in Fig. 4.2C where GR for two 3.5 year periods -- before and after mid-1991 -- are presented. Seismicity after mid-1991 shows a 77% increase over the previous 3.5 years. Furthermore, the earlier B-value, 0.68, is close to the global average for small events (i.e. 0.667); while the subsequent value of 0.51 is significantly lower which reflects a recent increase in the proportion of larger microearthquakes. Coupled with the recent increase and deepening of the microseismicity (80) and the appearance of M4+ activity since Fall 1992, the decreasing B-value may be indicative of a dynamic and non-stationary process of increasing fracture size or asperity strength possibly associated with intermediate-term nucleation of the expected M6 event at Parkfield.

Interestingly, the decreasing B-value could also result from the combined effects of the deepening microseismicity and the decreasing fraction of clustered microseismicity observed at Parkfield (80). This effect will be discussed further in the last section of this chapter.

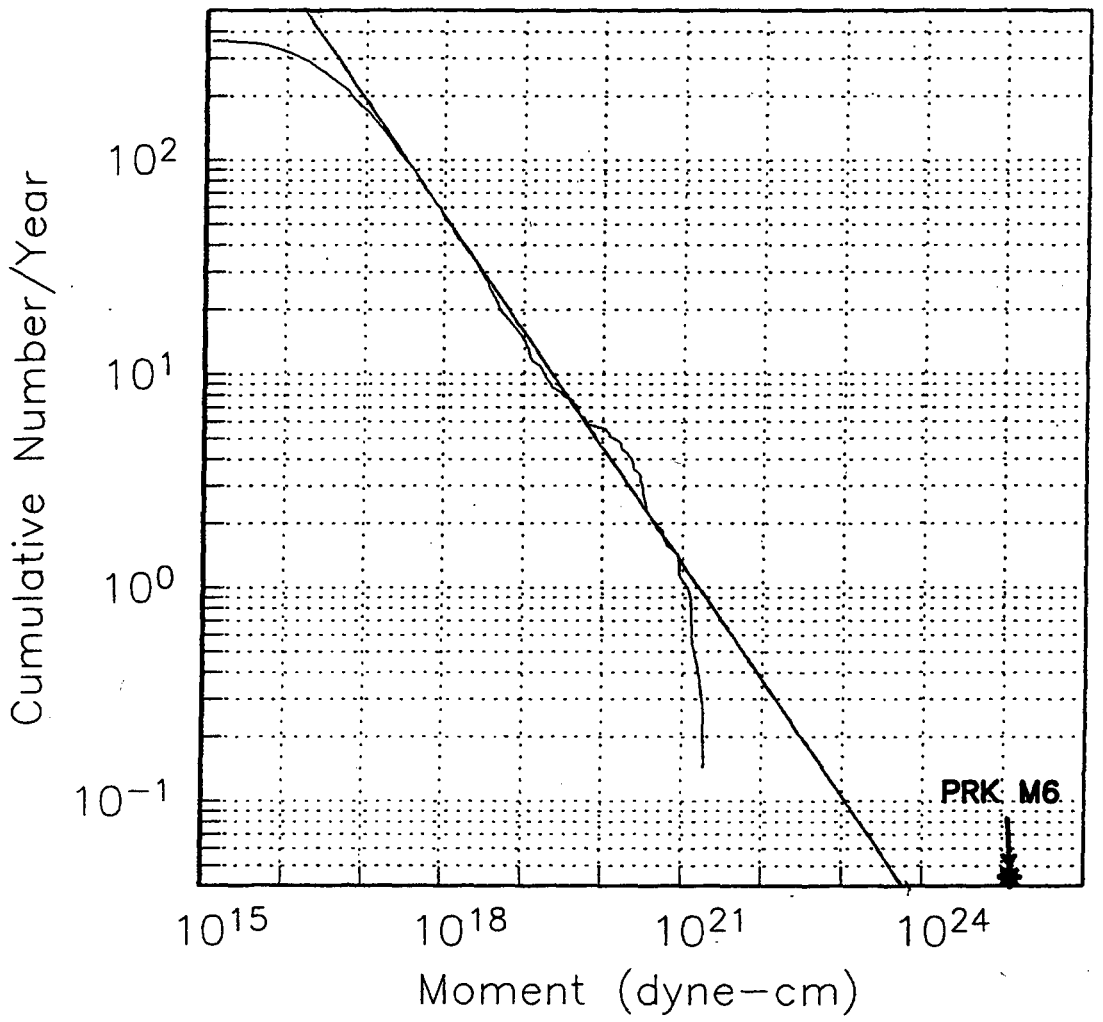

Fig. 4.2A GR distribution for Parkfield microearthquakes occurring in the 25x10x12 km study volume of Chapter III and recorded between 1988 and 1994 inclusive. The characteristic Parkfield M6 event is indicated with an asterisk.

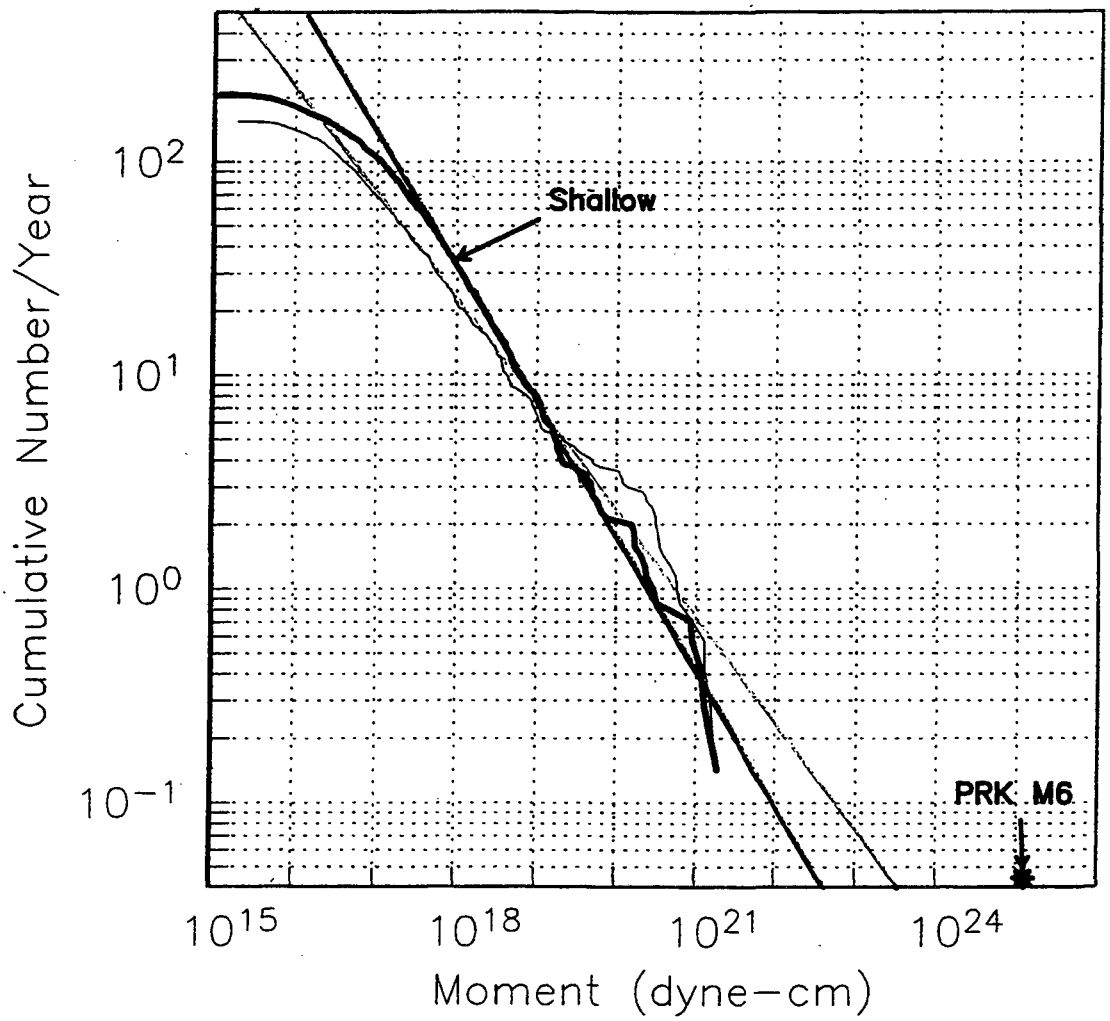

Fig. 4.2B Same as 4.2A with seismicity partitioned at 5 km depth. Darker curve shows the distribution above 5 km.

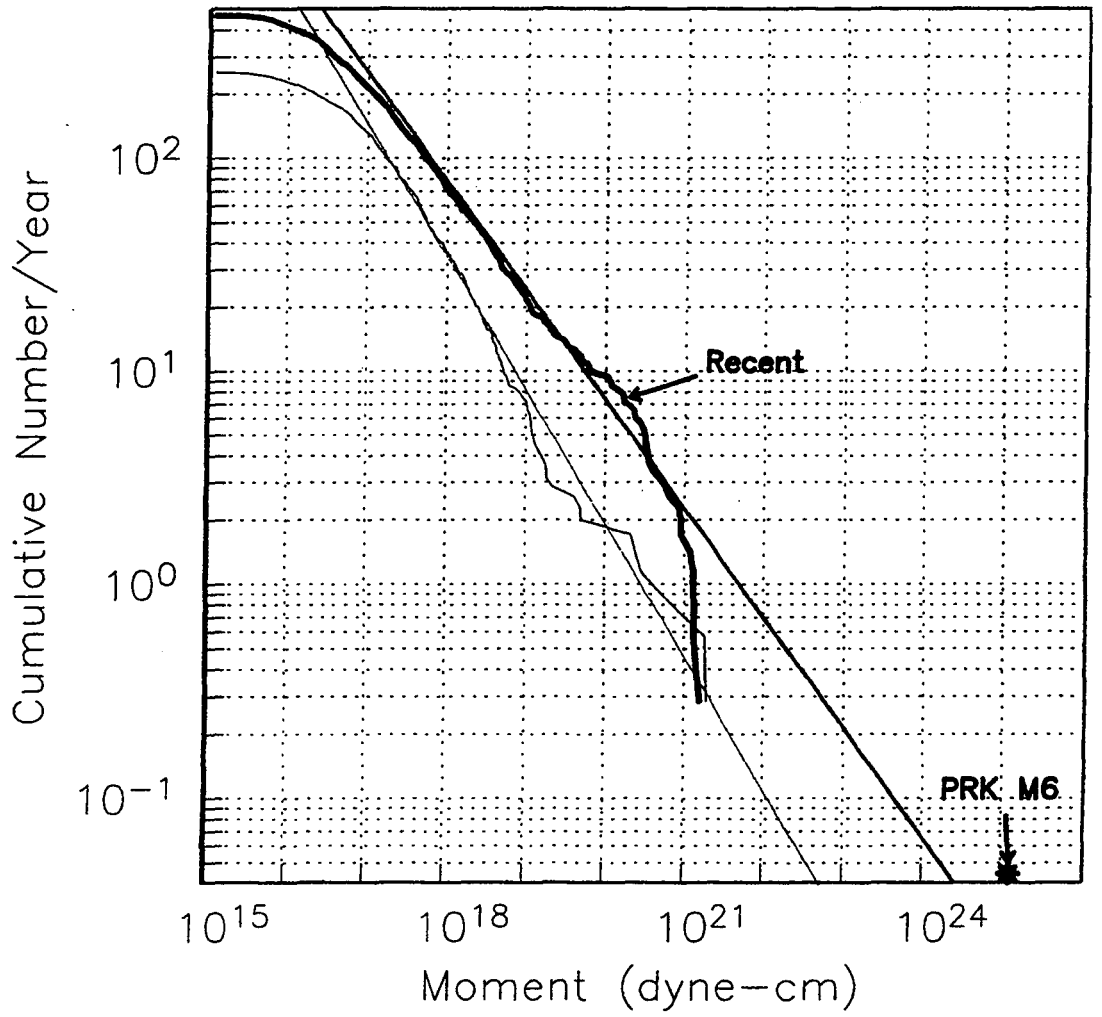

Fig. 4.2C Same as 4.2A with seismicity partitioned into two 3.5 year time windows before and after June 30, 1991. Darker curve shows recent activity. Note how, as time progresses, the largest event extrapolation approaches the PRK M6 datum.

In summary, the general features of the multiple-fault GR frequency-size relationship are seen in the predominantly clustered and characteristic Parkfield microearthquake data set with deviations similar to those seen generally for larger earthquakes under spatially varying and non-stationary conditions. This continuity of behavior to the microearthquake level suggests that scaling of mainshock ensemble activity extends beyond seismicity rates and decay -- to moments as well -- and justifies application of the GR size distribution to ensembles with mainshocks ranging in size from $M_o \sim 10^{15}$ to 10^{28}. In earthquake hazard analyses it supports the argument that parameters of seismic ensemble behavior observed for small earthquake sequences can be used to infer properties of expected damaging mainshocks and their ensembles. Care must be taken, however, to compensate for any depth dependence of the GR distributions especially when earthquake dimensions are small with respect to thickness of the brittle zone.

The observation of significant non-stationary seismicity at Parkfield has two important implications for hazard studies. First, the non-stationarity provides promise for the use of properties of microseismicity as intermediate to short-term indicators of impending large earthquakes (see Chapter V). Second, the accuracy of methods for empirical modeling of earthquake hazards using the GR can be improved by correcting for non-stationary effects. Corrections are especially necessary when, as is usually the case, the time windows of recorded seismicity are shorter than one cycle of the largest recurring earthquake or when substantial numbers of events obeying an M-T exist. A method of correction is

suggested at the end of this chapter.

M-T SCALING

Next I establish the empirical scaling relationship, M-T, which relates the seismic moment of characteristic sequences to their recurrence-times and suggests a common process between the recurrence of large damaging earthquake and microearthquake sequences. In Fig. 4.3 Parkfield characteristic microearthquake sequences are seen to exhibit a lognormal distribution in median normalized recurrence-times, $T_i/\overline{T}$, (i.e. the recurrence-times, T_i, ($i = 1,2,...,n-1$; n = number of events in the sequence) of a repeating sequence divided by the sequence median recurrence-time, $\overline{T}$). Intermediate-sized characteristic events (62) and large characteristic events (28, 29) are similarly lognormally distributed. Study of large damaging earthquakes has led to adoption of the lognormal distribution as a fundamental element in earthquake prediction models currently used in earthquake hazard assessments (29). The similarity of distributions across this wide spectrum of characteristic sequences argues for a common process and in favor of a M-T scaling relation.

By normalizing T_i by $\overline{T}$, a recurrence variable is defined which can be compared between all characteristic sequences regardless of average recurrence time. The measure of scatter of $T_i/\overline{T}$ commonly used for lognormal distributions is called the intrinsic uncertainty, σ_l, and is defined as one standard deviation of the natural log of the normalized recurrence

distribution,

$$\sigma_I = \text{s. d. } [\ln(T_i/\bar{T})] \qquad \text{(e10)}.$$

This is illustrated graphically in Fig. 4.3. A σ_I equal to 0 indicates strictly periodic and predictable recurrence-times whereas a value of 1 indicates random recurrence-times (a Poissonian process) with no predictability. The σ_I estimates for large damaging events worldwide and currently in use for earthquake hazard assessment ranges from 0.2 (28) to 0.5 +/- 0.2 (63). This corresponds well with the σ_I observed for Parkfield microearthquakes (i.e. 0.41, +/- 0.2; Fig. 4.3 right) (54) and with the σ_I reported for intermediate sized events (0.4) (62). This similar degree of scatter in recurrence-times between small and large events argues further for the existence of a common recurrence process on all observed scales.

The average recurrence-time, T ($\cong \bar{T}$), can serve as central measure of recurrence-time for each sequence and is observed to scale with the characteristic size of earthquake sequences, as shown in Fig. 4.4. Scatter about a best-fit line to the data rarely deviates outside the intrinsic bounds of 0.2 to 0.5, and the trend over 12 orders of magnitude is persistent. This relationship is the empirical M-T scaling we seek and is perhaps the strongest argument for regarding characteristic sequences ranging in moment from ~ 10^{15} to 10^{28} dyne-cm as a common population which physically scales. It relates small earthquakes to much rarer large events, independent of spectral concerns, and makes further study of the characteristic process possible by permitting the recurrence statistics derived from much more numerous and populated small earthquake

sequences to be incorporated with large earthquake statistics as has been repeatedly called for (1, 20, 21, 28, 29). It also indicates that models of large characteristic earthquake recurrence and predictability can be tested and/or refined (28, 29, 83) by using the more numerous small earthquakes (54) and that it might prove practical to scale recurring small mainshocks and ensemble behavior to improve hazard assessment techniques.

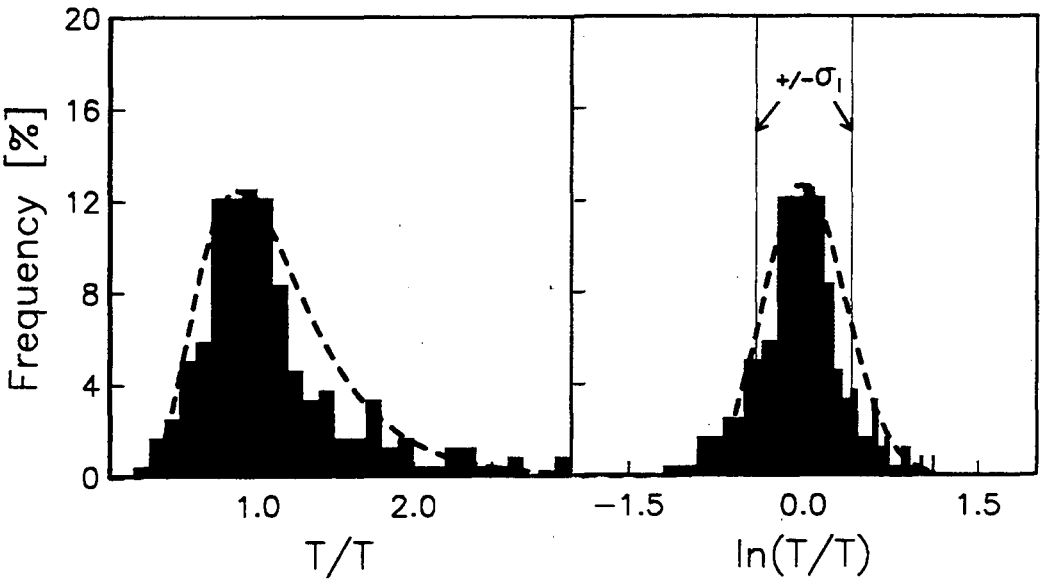

Fig. 4.3 (left) Relative frequency distribution of normalized recurrence intervals for 56 Parkfield characteristic microearthquake sequences (239 intervals). Data are fit by a lognormal distribution with an intrinsic uncertainty of 0.41. (Right) Same data showing frequency distribution of the natural log of the recurrence intervals. The distribution is approximately normal, and the intrinsic uncertainty of the distribution (i.e. one standard deviation) is indicated by σ_l.

Fig. 4.4. Slip-rate-normalized median seismic moment, M_o/V [dyne-Yr.], vs. average recurrence-time, T ($\cong \overline{T}$), for characteristic sequences along the San Andreas Fault system in California. Data sources: open hexagons are Parkfield microearthquake data (54), filled circles (62); filled squares (70) and (29); filled triangles (15). The dashed line is the least squares fit to all the data. The two thick solid lines are fits to sequences with $M_o/V < 10^{24}$. and $M_o/V > 10^{24}$. Theoretical slopes for constant stress drop events with circular (small events) and rectangular (large event) rupture geometries are shown as thin lines (lower and upper lines respectively). Short colored line segments represent gross uncertainties in recurrence-times expressed as intrinsic uncertainties, σ_I, of 0.2 and 0.5 (red and orange line segments respectively) about the circular rupture best fit. Uncertainties in M_o for events in characteristic sequences are typically within a factor of +/- $10^{0.75}$ of their nominal values (20). The characteristic Parkfield M6 sequence is indicated with an 'PRK M6'.

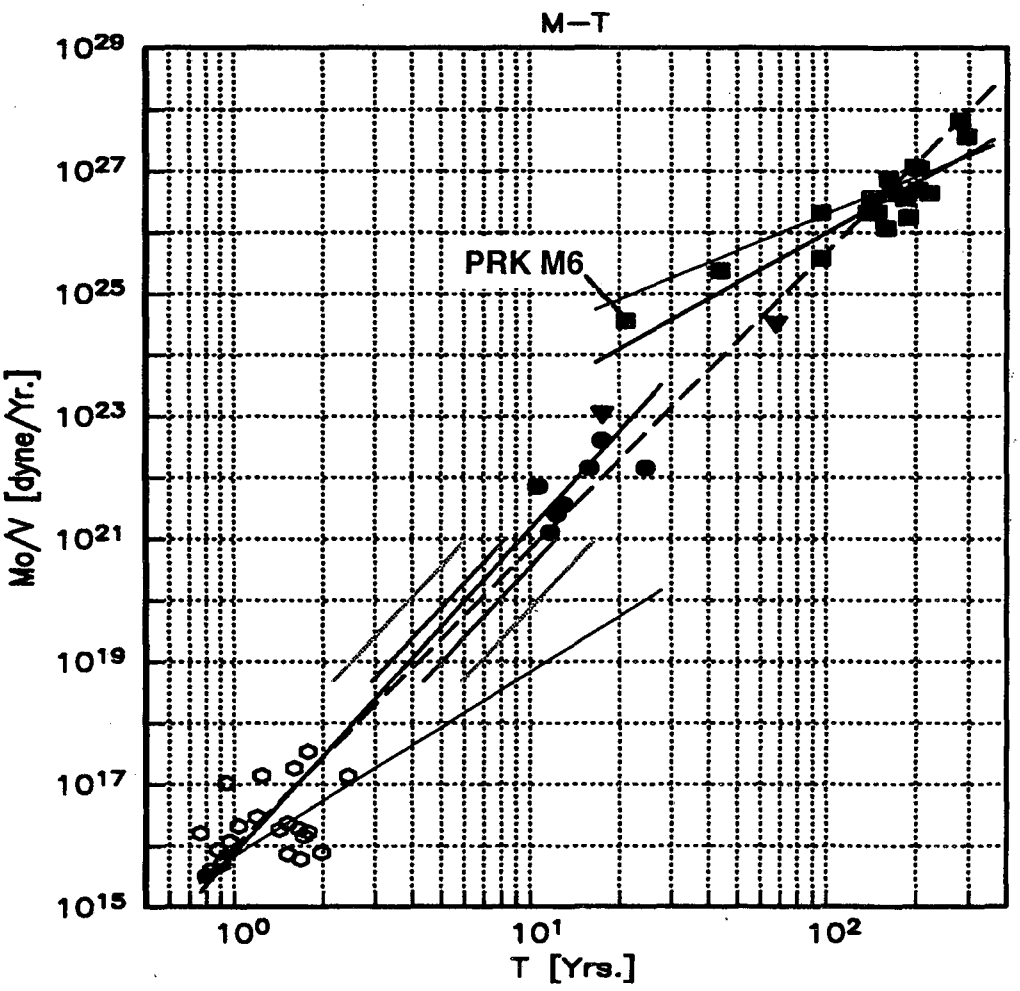
M—T
PRK M6
Mo/V [dyne/Yr.]
T [Yrs.]
10^29
10^27
10^25
10^23
10^21
10^19
10^17
10^15
10^0
10^1
10^2

To first order, the data in figure 4.4 define an empirical log-log-linear relationship,

$$\frac{M_o}{V} = KT^q \qquad \text{(e11)}$$

where (M_o/V) is the slip-rate-normalized seismic moment and K and q are empirically derived parameters 1.26×10^{16} and 4.82 respectively (dashed line). Subtle evidence for a slope change in the M-T curve (Fig. 4.4) at about $M_o/V \sim 10^{24}$, may be associated with rupture geometry and depth of the brittle-ductile transition at about 14 km depth, as previously suggested (1, 65). This change raises questions involving L and W rupture models which predict different characteristic dimensions for modeling the controlling fault stiffness, and which differ in whether or not the ductile region releases strain energy aseismically. Accepting the apparent change, we refine the M-T relation by modeling it as two lines with K and q values of 6.76×10^{15} and 5.1, and 3.65×10^{20} and 2.7 for sequences with M_o/V less than 10^{24} dyne-cm and greater than 10^{24} dyne-cm, respectively (Fig. 4.4 thick solid line fits).

IMPLICATIONS FOR THE M-T OBSERVATION

Non-constant stress drop:

The observed M-T relation differs significantly from that predicted for constant stress drop scaling (Fig. 4.4; thin lines). To see this consider that from (e1) and (e6),

$$M_o = GuA = GVTA \qquad \text{(e12)}$$

Equating (e2) and (e12),

$$M_o = GVTA = (1/C)(\Delta\sigma\Lambda)A \qquad \text{(e13)}$$

or

$$GVT=(1/C)(\Delta\sigma\Lambda). \qquad \text{(e14)}.$$

Using a circular crack to simulate small earthquake rupture, the characteristic dimension $\Lambda \sim L \sim W = a$ (78) where L and W are the length and width of the fault respectively, a is the radius of the circular crack, $C=C_S$ is a geometric constant and $A=\pi a^2$. For large earthquakes (modeled as infinitely long rectangular strike-slip faults) $C=C_I$, $A=LW$ (W=constant), and either $\Lambda=L$ (L-model (68)) or $\Lambda=W$ (W-model (66, 67)). Since C, G and V are constants, $\Delta\sigma$=constant requires from (e14) that Λ be proportional to T, i. e.,

$$[CGV/\Delta\sigma] = (\Lambda/T) = \text{const.} \qquad \text{(e15)}$$

so that for small earthquakes, (circular faults $A=\pi\Lambda^2$),

$$M_o=GVT\pi\Lambda^2. \qquad \text{(e16)}$$

Or, using (e14), (M_o/V) is proportional to T^3,

$$(M_o/V) \alpha T^3 \qquad \text{(e17)}.$$

For large earthquakes, (A=LW; W=constant),

$$M_o = GVTLW \qquad \text{(e18)}$$

so that using the L-model (Λ=L) and (e15),

$$M_o = GVT\Lambda W \quad \text{or} \quad (M_o/V) \alpha T^2 \qquad \text{(e19a)}.$$

For the W-model, ($u = VT \alpha \Lambda = W$ = constant),

$$M_o = GVTL\Lambda \quad \text{or} \quad (M_o/V) \alpha L \quad \text{(independent of T)} \qquad \text{(e19b)}.$$

It was derived empirically from Fig. 4.4 that for small earthquakes

$$M_o/V \propto T^{5.1} \qquad \text{(e20)}$$

and for large events,

$$M_o/V \propto T^{2.7} \qquad \text{(e21)}$$

This is in clear disagreement with the constant stress drop results of (e17) and (e19) and suggests instead that $\Delta\sigma$ is a function of M_o and T. A physical explanation for this dependence may lie in the interplay between actual asperity contact area and total rupture dimension (resulting in size dependent asperity strengths). Alternatively, the dependence may be an artifact of incorrect assumptions implicit in equations (e1 and e3), the identification of recurrence-times for moderate to large characteristic sequences, or in equations (e6). For example, constant stress drop can be preserved for the L-model if we allow, the ratio of seismic slip (u) to the sum of seismic and aseismic slips (VT) across an asperity to increase with seismic moment as,

$$\frac{u}{VT} = JM_o^r \qquad \text{(e22)}$$

where r = ((1/3) - ($1/q_s$)) = 0.137 and = ((1/2) - ($1/q_l$)) = 0.130 for small and large L-modeled earthquakes respectively. The physical constraint $\frac{u}{VT} \leq 1$ limits J for the largest earthquakes, J_l, to be $\leq 1.95 \times 10^{-4}$ and for small events, J_s, to be $\leq 1.32 \times 10^{-4}$. Hence accepting (e22), microearthquake asperities would need to experience about 50 times more aseismic slip than asperities of the largest events. Furthermore a break in the seismic to

aseismic slip ratio would need to exist between large and small events at $M_o \sim 10^{24}$. If indeed $\Delta\sigma$ were to remain constant (i.e. if (e22) holds) the implications would be significant since the premise u=VT (i.e. (e6)), fundamental to theoretical work on scaling (e.g. (73), (75)) and earthquake prediction (e.g. (29) and (62)), would no longer hold. Regardless of the physics, therefore, the M-T appears to require a rethinking of established beliefs regarding earthquake source parameters and mechanical conditions in the fault zone.

Source parameter scaling:

As an illustration of how the M-T might effect the scaling of earthquake source parameters consider the more plausible case where equations (e1 - e3), recurrence-time estimates of large characteristic sequences and equation (e6) are assumed valid. Then, equating (e11) and (e12),

$$\frac{M_o}{V} = KT^q = GTA \qquad \text{(e23).}$$

Solving for earthquake rupture area, A, and characteristic dimension, Λ,

$$A = \frac{KT^{(q-1)}}{G} = (\pi\Lambda^2) \text{ or } (\Lambda W) \text{ or } (L\Lambda) \qquad \text{(e24)}$$

and,

$$\Lambda = \left(\sqrt{\frac{K_S T^{(q_s-1)}}{G\pi}} \right) \text{ or } \frac{K_l T^{(q_l-1)}}{GW} \text{ or } \frac{K_l T^{(q_l-1)}}{GL} \qquad \text{(e25)}$$

for small ($q=q_S$, $K=K_s$) and large L- and W-modeled earthquakes, ($q=q_l$, $K=K_l$), respectively. In addition, since W=constant for large earthquakes, (e25) and (e6) indicate that $L \alpha T^{(q-1)} \alpha u$ for both L- and W-models,

$$L = \frac{K_l}{GW} T^{(q_l-1)} \text{ or } T = \left(\frac{GW}{K_l} L \right)^{\frac{1}{(q_l-1)}} \alpha\, u \qquad \text{(e26).}$$

A relationship between $\Delta\sigma$ and T can be obtained by equating (e2) and (e11),

$$M_o = (1/C)\Delta\sigma\Lambda A = VKT^q \qquad \text{(e27)}$$

and by solving for stress drop,

$$\Delta\sigma = \frac{VKC}{\Lambda A}T^q = VKCT^q\left(\frac{1}{\pi\Lambda^3} \text{ or } \frac{1}{\Lambda^2 W} \text{ or } \frac{1}{\Lambda^2 L}\right) \qquad \text{(e28).}$$

By substituting Λ from (e25) into (e28) we get,

$$\Delta\sigma = \left(VC_S G^{\frac{3}{2}}\sqrt{\frac{\pi}{K_S T^{(q_s-3)}}}\right) \text{ or } \left(\frac{VC_l G^2}{K_l T^{(q_l-2)}}W\right) \text{ or } \left(\frac{VC_l G^2}{K_l T^{(q_l-2)}}L\right). \qquad \text{(e29)}$$

for small, large L- and W- models. Alternatively, the W-model case can be written,

$$\Delta\sigma = \frac{VC_l G}{W}T \qquad \text{(e30)}$$

by substituting (e26) for L.

Constraints implied by source parameters:

Equations (e23 - e30) reduce to the constant stress drop case when q_s =3 and q_l = 2; however, the empirically derived values of q_s = 5.1 and q_l = 2.7 from (e20) and (e21) indicate in (e25) that slip, u (proportional to T), scales approximately with $\sqrt{\Lambda = a}$ for small earthquakes and with $\sqrt{\Lambda = L}$ for large events using either L- or W- models. This is in contrast to what is usually assumed -- that u scales linearly with Λ (the reference length for strain in (e3)). Since Λ strongly effects the controlling stiffness of the fault (G/Λ in (e3)) these results suggest, through (e28), that for small earthquakes and

large L-modeled events $\Delta\sigma \alpha 1/T$ or $\Delta\sigma \alpha \left(\frac{1}{M_o}\right)^{\frac{1}{q}}$ -- stress drop decreases with event size -- and that for large W-modeled earthquakes $\Delta\sigma \alpha T$ or $\Delta\sigma \alpha (M_o)^{\frac{1}{q}}$ -- stress drop increases with event size. This bears directly on the controversy regarding current conceptualizations of the L- (68) and W- (66,67) models of earthquake scaling since it indicates that the accepted models (which assume $\Delta\sigma$ = const.) are incorrect.

An important consequence of this is that the accepted moment-dimension relationships ($M_o \alpha a^3$ for small events and $M_o \alpha L^2$ and $M_o \alpha L$ for large L- and W-models respectively) are replaced by new approximate relationships ($M_o \alpha a^{2.5}$ for small events and $M_o \alpha L^{1.5}$ for large earthquakes using either the L- or W- models). If valid, these new relationships have important implications for understanding the physics underlying tectonic strain release (73), the estimation of high-frequency strong ground motion, and moment-magnitude scaling relationships (77).

Other implications of these constraints on source parameters include:

1.) increasing asperity strength with decreasing size.

2.) increasing normal stress with decreasing asperity size (this also argues for greater stick-slip behavior for small earthquakes).

3.) increasing stress drops with decreasing earthquake size (important for large earthquake nucleation models (69)) which approach intact rock strengths (a few kilobars) for very small events ($M_o \sim 10^{13}$).

4.) more rapidly increasing source corner frequencies with

decreasing event size than predicted using the constant stress drop assumption (e.g.. preliminary calculations using a standard method (78) indicate that the spectral source corner at $M_0 \sim 10^{19}$ (~ magnitude 2) ~ 140 Hz and 100 Hz for P and S respectively compared to expected values of from 7.6 to 35 Hz and 5.4 to 25 Hz for P and S using constant stress drops of 1 and 100 bars respectively).

5.) a regionally averaged reference asperity size (K/G) corresponding to T = 1yr. (i.e. where (e23) and (e11) have no dependence on exponent q) can be defined which represents the proportionality between recurrence-time, T (proportional to slip, u) and rupture area, A, in (e24). It is dependent on regional mechanical properties -- average asperity strengths, geometries, and rock rigidity -- and is expected to vary significantly with tectonic environment and depth. For small earthquakes well distributed about a fault, observed differences in (K/G) might be used to estimate variations in fault strengths or rock rigidity with depth or along strike.

Implications of M-T on occurrence patterns:

Elastic rebound theory (58) suggests that those sequences plotting left of the best fit line of Fig. 4.4 should, on average, experience longer recurrence-times in the near future while those to the right will experience shorter intervals. One might speculate that this effect is being observed for the Parkfield M6 sequence which currently is experiencing a prolonged inter-event recurrence-time. The M-T scaling also indicates that, in

addition to the 1/t decay and quasi-periodic recurrence patterns of event ensembles discussed earlier, other patterns of microearthquake activity should be observable in large earthquake seismicity -- given a long enough period of observation and comparable analyses resolutions. Examples include:

1.) Systematic spatial and temporal variability in the regularity of recurrence times (parameterized by σ_l).

2.) Systematic non-lognormal recurrence-time variability for individual sequences which in composite behave lognormally.

3.) Gaps in and/or shutdowns of characteristic sequences.

4.) Initiation of new repeating sequences.

5.) Commutative triggering between intra-cluster event-types during repetitions of mainshock ensembles.

6.) Incorporation of separate intra-cluster event types into a single event-type or degradation of single event types into multiple event types.

7.) Long recurrence-times compensated for by subsequently short recurrence-times.

8.) Many foreshock, aftershock and compound events being characteristic in location size and waveform, but with recurrence-times associated with the mainshock recurrence-times rather than independently quasi-periodic.

A MODEL FOR NON-LINEAR GR RELATIONSHIPS

The M-T adds a Fourier aspect to the GR relation through the size dependent quasi-periodicity of a large fraction of the seismicity. This phenomena has implications for physical interpretations of the GR and can provide an alternative explanation for observed variations in the GR slopes previously attributed to fault-specific earthquake behavior, temporal changes associated with nucleation, and scaling changes associated with the brittle-ductile transition. We have seen that characteristic sequences occur systematically over a wide range of seismic moments and recurrence-times and Fig. 4.5 shows that for repeating Parkfield microearthquakes, the frequency-size distribution of repeating events follows a GR-like distribution but with a greater B-value than a GR using all the microearthquakes. If we infer the same bias in the size distribution for large repeating sequences and a tendencey toward triggering between sequences in proximity, then a break in the fault-specific GR may exist at seismic moments whose corresponding recurrence-times, T, are comparable to the seismicity catalogue duration, τ.

To understand this windowing effect more clearly, consider modeling the fault-specific cumulative GR for one seismic cycle (where $V \cong$ const. is assumed), $Ne(M_o)$, as the superposition of two cumulative size distributions, $Ne1(M_o)$ and $Ne2(M_o)$, where $Ne1(M_o)$ represents the distribution of events which do not repeat (or are reactivated after anomalously long periods of dormancy) and $Ne2(M_o)$ represents the distribution of earthquakes that repeat quasi-periodically. If we take the cumulative number of sites of seismic activity over one seismic cycle to be $Ns(M_o)$ -- the number of non-repeating earthquakes plus the number of

sites of repeated activity counted once -- then,

$$Ne(Mo) = Ne1(Mo) + Ne2(Mo) = (1 - Fr)Ns(Mo) + Fr\int_{Mo} \frac{dNs(M)}{dM} R(M,t)\, dM \quad (e31)$$

where Fr is the fraction of seismic sites per seismic cycle which experience repeating activity and $R(M,\tau)$ is the repeating earthquake contribution (Here Fr is assumed to be constant with M_o). Because of the power-law distribution of fractures in the earth (75, 79), I model $Ns(M_o)$ similar to (e6),

$$Ns(M_o) = a_c M_o^{-B_s}. \quad (e32)$$

where a_c is taken over one complete seismic cycle. Then the probability density function of sites of activity producing events of size M_o is the derivative of (e32),

$$\frac{dNs(M_o)}{dM_o} = -B_s a_c M_o^{-(B_s+1)}. \quad (e33)$$

For repeating sites, the number of events recorded in the seismic catalogue with a given moment, $R(M,\tau)$, depends on the catalogue duration, τ,

$$R(M_o,\tau) = \tau/T \quad (e34)$$

where T is the recurrence-time of the repeating sequence. The M-T, (e11), gives the dependence of T on seismic moment,

$$T = \left(\frac{M_o}{KV}\right)^{\frac{1}{q}} \tag{e35}$$

so that,

$$R(M_o,\tau) = \tau\left(\frac{M_o}{KV}\right)^{-\frac{1}{q}}. \tag{e36}$$

and after normalizing for catalogue duration, τ, (e31) becomes,

$$\begin{aligned}\frac{N_e(M_o)}{\tau} &= \left[(1-F_r)\left(\frac{a_c}{\tau}\right)M_o^{-B_S}\right] - \left[B_S a_c F_r (KV)^{\frac{1}{q}} \int_{M_o} M^{-\left(B_S+1+\frac{1}{q}\right)} dM\right] \\ &= \left[(1-F_r)\left(\frac{a_c}{\tau}\right)M_o^{-B_S}\right] + \left[\frac{B_S a_c F_r (KV)^{\frac{1}{q}}}{\left(B_S+\frac{1}{q}\right)}\left(M_o^{-\left(B_S+\frac{1}{q}\right)} + C_1\right)\right] \\ &= \left[\left(\frac{1-F_r}{\tau}\right) + \frac{B_S F_r (KV)^{\frac{1}{q}}}{\left(B_S+\frac{1}{q}\right)} M_o^{-\frac{1}{q}}\right] a_c M_o^{-B_S} + C_2;\end{aligned} \tag{e37}$$

where, $$C_2 = C_1\left(\frac{B_S a_c F_r (KV)^{\frac{1}{q}}}{\left(B_S+\frac{1}{q}\right)}\right)$$

Here C_1 is a constant of integration and can be calibrated for one seismic cycle using $N_e(M_o=M_{max}) = 1$. The τ-normalized cumulative distribution of non-repeating sites, $N_{e1}(M_o)/\tau$ is a line in log-log space with slope -Bs and is independent of K and q. Superposed on this is $N_{e2}(M_o)/\tau$ which includes the integration constant and is dependent on K and q and in log-log space defines a bi-assyptotic function. For relatively small M_o this term

has a slope -(Bs +1/q) (q empirically determined earlier to be 5.1 for $M_o < 10^{24}$ and 2.7 for $M_o > 10^{24}$ dyne-cm) while for larger M_o the function approaches the asymptote $Ne2(M_o) = C_2$.

The M_o where $\tau = \left(\frac{M_o}{KV}\right)^{\frac{1}{q}}$ is called M_{crit} and is the point where the slope of the $Ne2(M_o)$ distribution equals the slope of the $Ne1(M_o)$ distribution. It is significant in that it defines the windowing effect of τ for sequences with phased periodicity and is analogous to the concept of a high pass filter corner. For phased sequences with M_o decreasing below M_{crit}, $Ne2(M_o)$ contributes systematically greater numbers of repeated events per site to $Ne(M_o)$ resulting in a greater effective B-value ($B=B_s+1/q$), while for phased sequences with M_o increasing above M_{crit} the contribution of $Ne2(M_o)$ to $Ne(M_o)$ rapidly becomes insignificant and B approaches B_s. Hence, if a significant fraction of seismically active sites repeat characteristically with phased periodicity and can be defined by a positively sloped M-T, a sharp change in effective B-value with M_o will result about $M_o = M_{crit}$ due to the filtering effect imposed by the catalogue window length.

The in-phase assumption is very restrictive and is not observed for sequences over the entire size range over a wide area, however, evidence of induced seismicity and triggering of nearby events on many scales (see Chapter III induced seismicity section) suggests it does occur in fault-specific situations. Hence, the in-phase effect for decreased B-values might be expected for τ values whose corresponding Mo

approaches the maximum likely event size on a specific fault segment. Observations of decreases in B-values are numerous, especially for fault specific cases (47, 76), and are otherwise inferred to result from characteristic behavior of the largest event on a fault (characteristic earthquake model). However, these results suggest that distributions similar to the characteristic earthquake model might result as an artifact of catalogue length.

Recent observations of increased B-values for large M_o have also been reported (84) and have been attributed to scaling and brittle-ductile transition depths. Attempts at modeling this break in GR linearity use L- and W- models which assume constant stress drop, self-similarity of physics and a tiling argument (73, 74, 75). Equation (e37), however, provides an alternative model which replaces these assumptions with an empirically based M-T and an estimate of the fractional partitioning of earthquakes into recurring and non-recurring events. If, as with the M-T in this chapter, the break in M-T scaling at the transition from small to large earthquakes corresponds to decreased q and increased K values, then the new q and K will enhance the contribution of Ne2(Mo) to Ne(Mo) and significantly raise the effective B-value for events with Mo > 10^{24} dyne-cm.

Equation (e37) also indicates that extrapolation of GR slopes using small earthquakes to estimate large event recurrence can seriously underestimate earthquake hazard when significant M-T seismicity exists. This is because the B-values for repeating events are steeper by (1/q) causing the extrapolation to intercept $N(M_o)$ =[1/(largest event recurrence-

time)] at a lower maximum M_o (much like the situation shown in Fig. 4.2A). Equation (e37) suggests a means of correcting for this, however, which involves removing the repeated earthquake contribution and extrapolating large earthquake recurrence based on the distribution of sites of seismic activity only -- (e32).

A note on non-stationarity, the recently reported increase and deepening of seismicity (and the decreasing fraction of clustered to total seismicity) at Parkfield (80) is indicative of a high degree of new fracturing or reactivation of long dormant fractures. The new and reactivated faults do not recur quasi-periodically and therefore do not follow the established M-T; as a result, their contribution to (e37) enters through the lower B-value $Ne1(M_o)$ term. In this way, the temporally decreasing B-values reported earlier can result from the activation of dormant faults and not from any increase in average fault dimension or from activation of a greater proportion of stronger deep faults as has been suggested (1) -- B_s can remain stationary while effective B decreased due to increased non-repeating seismicity. These non-stationary effects, too, can be corrected for using (e37) provided accurate time dependence for Fr and a can be determined. Such a correction should improve on current GR based hazard estimates which assume stationarity in all aspects of GR.

It is quite possible that in the derivation of (e37) the assumption Fr = constant may need to be replaced by $Fr = Fr(M_o)$ in which case both terms of (e31) would require integration over M. Furthermore, non-stationary conditions suggest Fr and a would more appropriately be modeled as time

varying. However, the general conclusion of this section -- that moment dependent recurrence-times of characteristic sequences can lead to variations of slope in the GR relationship similar to those attributed to other physical causes -- should still hold.

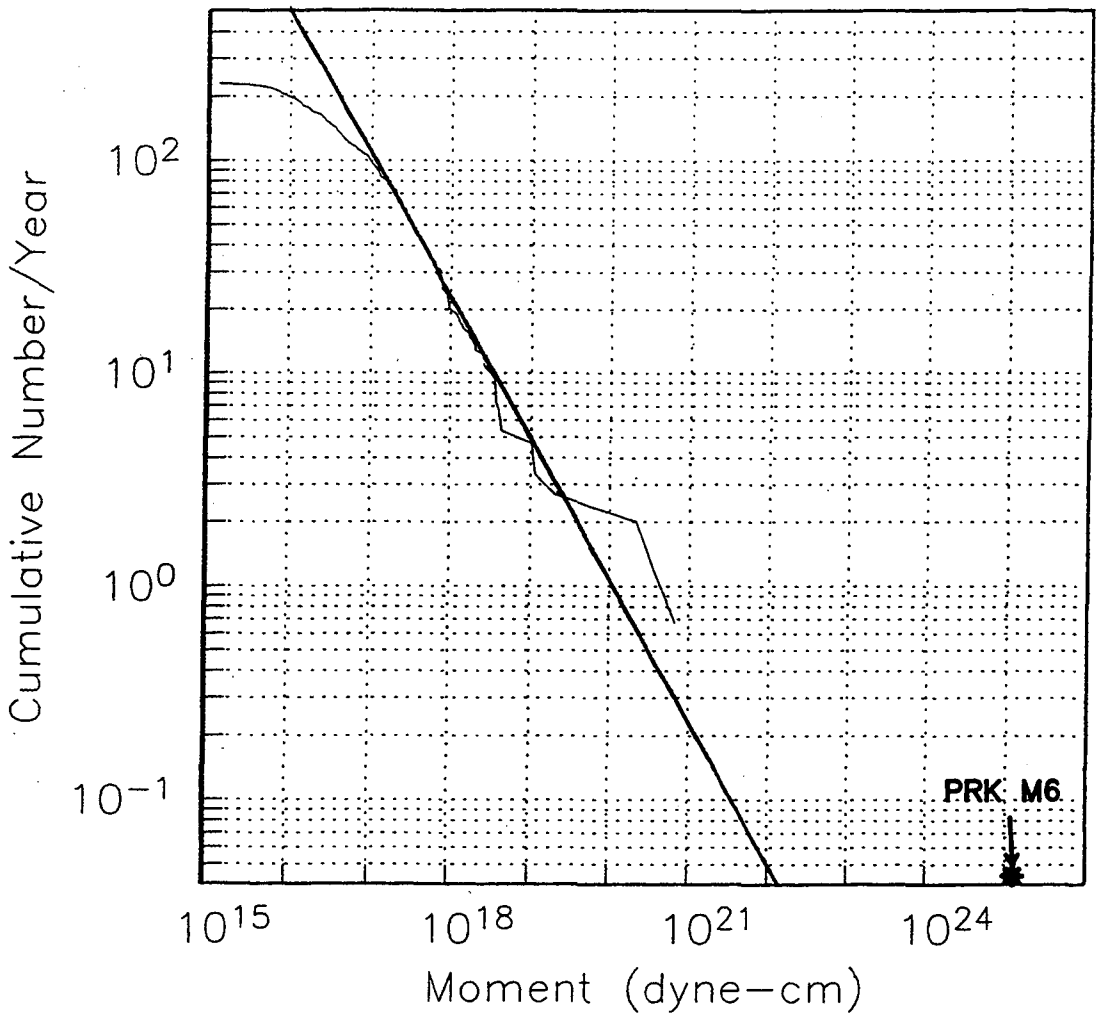

Fig. 4.5 Same as Fig. 4.2A using only data from the 68 currently identified characteristic sequences (357 events). The curve is normalized to 1679 events (full catalog) to simulate a GR composed of purely repeating sequences. The B-value for these events -- 0.72 -- is significantly larger than for the general population -- 0.58 -- and results in a linear extrapolation which underestimates the largest event (PRK M6) by more than the overall GR power-law. Hence, large B-values for small events can be at least partially explained by the repeating seismicity effect. shown in 4.2A. In other respects the distribution generally agrees with the GR distribution of the total microearthquake population.

CONCLUSIONS

Average recurrence-times of characteristic earthquake sequences along the San Andreas Fault system, ranging in seismic moments from ~10^{15} to ~10^{28} ($M_W \cong$ -0.5 to 8), are found to scale to the 5.1 and 2.7 power with slip rate normalized median moment for small and large earthquake sequences respectively. This scaling is inconsistent with that expected for a constant stress drop model with slip and moment release rate in equilibrium. The result has implications for fault zone mechanics, earthquake prediction and hazard estimates. Accepting the validity of (e6) also leads to unconventional relationships among source parameters (seismic moment, M_o; fault length, L; fault width, W; circular fault radius, a; seismic slip, u; average recurrence-time, T; static stress drop, $\Delta\sigma$; and fault rupture area, A) such as:

1) $M_o \alpha L^{\left(\frac{q}{q-1}\right)} \sim L^{1.5}$ and $M_o \alpha a^{\left(\frac{2q}{q-1}\right)} \sim a^{2.5}$ for large and small earthquakes respectively.

2) $u \alpha a^{\left(\frac{2}{q-1}\right)} \sim (a)^{0.5}$ and $u \alpha L^{\left(\frac{1}{q-1}\right)} \sim (L)^{0.5}$ for large and small events using either L or W-models.

3) $\Delta\sigma \alpha 1/T$ -- $\Delta\sigma \alpha \left(\frac{1}{M_o}\right)^{\frac{1}{q}}$. for small events and large events using the L-model and $\Delta\sigma \alpha T$ -- $\Delta\sigma \alpha (M_o)^{\frac{1}{q}}$ for large events using the W-model.

4) and $A \alpha T^{(q-1)}$ regardless of earthquake size.

where q_s = 5.1 and q_l = 2.7 are derived empirically for small and large

earthquakes respectively.

The M-T scaling relationship and the abundance of recurring Parkfield microearthquakes defines the recurrence process in a few years, providing a small-event base from which to study and scale to large SAF characteristic earthquakes. It also suggests a means of assessing, in a time predictable manner, the seismic hazards associated with recurring mainshock ensembles, and it provides an alternative explanation for observed variations in GR slope previously attributed to fault-specific conditions or brittle-ductile transition depths.

REFERENCES

1. C. H. Scholz, The Mechanics of Earthquakes and Faulting (Cambridge Univ. Press, 1990).

2. K. Aki, Bull. Earthquake Res. Inst., Tokyo Univ. 44, 23 (1966).

3. J. Brune, J. Geophys. Res. 75, 4997 (1970).

4. T. C. Hanks, Pure Appl. Geophys. 115, 441 (1977).

5. T.C. Hanks, Bull. Seismol. Soc. Am. 72, 1867 (1982).

6. E. L. Majer and T. V. McEvilly, Geophysics 44, 246 (1979).

7. A. E. Romero, Ph. D. Thesis University of California, Berkeley (1995).

8. K. Aki, J. Geophys. Res. 89, 5867 (1984).

9. A. Frankel, Bull. Seismol. Soc. Am. 72, 1379 (1982).

10. A. Frankel and L. Wennerberg, Bull. Seismol. Soc. Am. 76 2167 (1989).

11. J. Got and J. Fre'chet, Geophys. J. Int. 114, 325 (1993).

12. M. Antolik, R. M. Nadeau, R. C. Aster, T. V. McEvilly, Bull. Seismol. Soc. Am. in press (1995).

13. E. Cranswick, R. Wetmiller, J. Boatwright, ibid. 75 1535 (1985).

14. A. Frankel and R. W. Clayton, ibid. 72 1379 (1984); A. Frankel and R. W. Clayton, ibid. 91 6465 (1986).

15. J. Dieterich, J. Geophys. Res. 99 2601 (1994).

16. P. A. Reasenberg and L. M. Jones, Science 243, 1173 (1989).

17. L. M. Jones, Bull. Seismol. Soc. Am. 84, 892 (1994).

18. Based on Omori's observation of the decay of earthquakes following the 1891 Nobi Japan earthquake).

19. B. Gutenberg and C. F. Richter, Seismicity of the Earth and Associated Phenomena (Princeton University Press, Princeton, New Jersey, 1954).

20. D. P. Schwartz and K. J. Coppersmith, J. Geophys. Res. 89, 5681 (1984).

21. J. Wakefield, EOS 76, 169 (1995).

22. Y. Y. Kagan, Bull. Seismol. Soc. Am. 83, 7 (1993).

23. J. McCloskey and C. J. Bean, Science 266, 410 (1994).

24. Y. Y. Kagan, Geophys. J. Int. submitted (1995).

25. K. Sieh, Bull. Seismol. Soc. Am. 68, 1421 (1978); K. Sieh, J. Geophys. Res. 89, 7641 (1984); K. Sieh, M. Stuiver, D. Brillinger, J. Geophys. Res. 94, 603 (1989).

26. K. Sieh and P. L. Williams, J. Geophys. Res. 95, 6629 (1990).

27. D. P. Schwartz, K. J. Coppersmith, F. H. Swan III, P. Somerville, W. U. Savage, Earthquake Notes, 52, 71 (1981).

28. S. P. Nishenko and R. Buland, Bull. Seismol. Soc. Am. 77, 1382 (1987).

29. Working Group on California Earthquake Probabilities, U.S. Geol. Surv. Open-File Rept. 88 (1988); _____, U.S. Geol. Surv. Circ. 1053 (1990); _____, Calif. Div. Mines Geol. Spec. Pub. 42 (1992); _____, Bull. Seismol. Soc. Am. 85, 379 (1995).

30. S. K. Singh, M. Rodriguez, L. Esteva, Bull. Seismol. Soc. Am. 73, 1779 (1983).

31. T. Utsu, J. Fac. Sci. Hokkaido Univ. Ser. 73, No. 3 (1969); _____, Geophysics 30, 521 (1961); _____, J. Fac. Sci. Hokkaido Univ. Ser, 73, No. 4 (1970); _____, ibid. 3, No. 5 (1971); _____, ibid. 4, No. 1 (1972); _____, J. Phys. Earth 22, 71 (1974).

32. L. Jones and P. Molnar, J. Geophys. Res. 84, 3596 (1979).

33. L. M. Jones, Bull. Sesimo. Soc. Am. 75, 1669 (1985).

34. Y. Y. Kagan and D. D. Jackson, J. Geophys. Res. 96, 21419 (1991).

35. Y. Ben-Zion and J. R. Rice, J. Geophys. Res. in press (1995); J. R. Rice, EOS Trans. Amer. Geophys. Union, 75, 441 (1994).

36. R. Burridge and L. Knopoff, Bull. Seismol. Soc. AM. 57, 3411 (1967); L. Knopoff, T. Levshina, V. I. Keilis-Borok, C. Mattoni, preprint (1994); C. R. Myers, J. S. Langer, B. E. Shaw, preprint (1995).

37. T. C. Hanks, J. Geophys. Res. 84, 2235 (1979).

38. D. Andrews, ibid. 85, 3867 (1980).

39. K. Aki, Earthquake prediction, an International Review. M. Ewing Ser. 4, ed., 566 (1981).

40. S. Wesnousky, C. Scholz, K. Shimazaki, j. Geophys. Res. 88, 9331 (1983).

41. P. Segall and D. Pollard, Geol. Soc. Am. Bull. 94, 563 (1983)

42. T. Hirata, Pageoph 131, 157 (1989).

43. W. Bakun and T. V. McEvilly, J. Geophys. Res. 89 3051 (1984).

44. S. Suyehiro, T. Asada, M. Ohtake, Papers Meteorol. Geophys. 15, 71 (1964).

45. S.Wu, C. A. Cornell, S. R. Winterstein, Bull. Seismol. Soc. Am. 85, 1 (1995).

46. S. K. Singh, M. Rodriguez, L. Esteva, Bull. Seismol. Soc. Am. 73, 1779 (1983).

47. R. R. Youngs and K. J. Coppersmith, ibid. 75, 939 (1985).

48. C. Scholz, ibid. 58, 399 (1968a).

49. K. Mogi, Earthquake Prediction, an International Review. M. Ewing Ser. 4, 43 (1981).

50. R. A. Harris and P. Segall, J. Geophys. Res. 92, 7945 (1987).

51. K. Aki, ibid. 92, 1349 (1987).

52. (48)

53. L. R. Sykes, ibid. 75, 6598 (1970).

54. R. M. Nadeau and T. V. McEvilly, Seismol. Res. Lett. 66, 40 (1995)

55. E. Karageorgi, R. Clymer, T. V. McEvilly, Bull. Seismol. Soc. Am. 82. 1388 (1992).

56. E. Karageorgi and T. V. McEvilly, in preparation, (1995).

57. G. K. Gilbert, Science XXIX, 121 (1909).

58. H. F. Reid, The California Earthquake of April 18, 1906, Report of the Satake Earthquke Investigation Commission, 2, 1 (1910).

59. C. R. Allen, Proceedings of the Conference on Geologic Problems of the San Andreas Fault System. 11, 70 (1968).

60. R. E. Wallace Geol. Soc. Am. Bull. 81, 2875 (1970).

61. D. D. Jackson and Y. Y. Kagan, EOS Suppl. 76, S199 (1995).

62. W. L. Ellsworth, Characteristic earthquakes and long-term earthquake forecasts: Implications of central California seismicity, Urban disaster mitigation: The role of engineering and technology (Elsevier Science, Ltd., Oxford, U.K., 1995).

63. 29. Working Group on California Earthquake Probabilities, Bull. Seismol. Soc. Am. 85, 379 (1995).

64. (54).

65. K. Shimazaki, Earthquake Source Mechanics. AGU Geophys. Mono. 37, 209 (1986).

66. L. Knopoff Geopys. J. R.A.S. 1, 44 (1958).

67. A. Starr, Proc. Cambridge Philos. Soc. 24, 489 (1928).

68. C. Scholz, Bull. Seismol. Soc. Am. 72, 1 (1982a).

69. J. R. Rice, EOS Trans. Amer. Geophys. Union, 75, 441 (1994).

70. L. R. Sykes and S. P. Nishenko, J. Geophys. Res. 89, 5905 (1984).

71. J. G. Anderson and J. E. Luco, Bull. Seismol. Soc. AM. 73, 471 (1983).

72. B. Stump and L. R. Johnson, Bull. Seismol. Soc. Am. 67, 1489 (1977).

73. B. Romanowicz and J. B. Rundle, ibid. 83,1294 (1992).

74. J. F. Pacheco, C. Scholz, L. Sykes, Nature 355, 71 (1992).

75. J. B. Rundle, J. Geophys. Res. 94, 12337 (1989).

76. S. G. Wesnousky, Bull. Seismol. Soc. Am. 84, 1940 (1994).

77. T. C. Hanks, Pure Appl. Geophys. 115, 441 (1977); T. C. Hanks, J. Geophys. Res. 84, 2235 (1979); G. M. Atkinson and T. C. Hanks, Bull. Seismol. Soc. Am. 85, 825 (1995).

78. T. Sato and T. Hirasawa, J. Phys. Earth 21, 415 (1973).

79. G. C. P. King, Pure Appl. Geophys. 121, 762 (1983).

80. R. M. Nadeau, W. Foxall, T. V. McEvilly, Science 267, 503 (1995).

81. P. E. Malin, S. N. Blakeslee, M. G. Alvarez, and A. J. Martin, Science 244, 557 (1989); Y. Benzion and J. rice, J. Geophys. Res. 98, 14109 (1993).

82. T. Hanks and H. Kanamori, J. Geophys Res. 84, 2348 (1979).

83. R. M. Nadeau, W. Foxall, T. V. McEvilly, Seismol. Res. Lett., in prep. (1995).

84. J. F. Pacheco and L. Sykes, Bull. Seismol. Soc. Am. 82, 1306 (1992).

CHAPTER V

Monitoring Temporal Change in Seismicity and Wave Propagation.

INTRODUCTION

In this chapter, the monitoring potential of the Parkfield microearthquake data set is illustrated with results from studies of temporal change in seismicity patterns and in wave propagation characteristics. The patterns of Parkfield microearthquakes have changed markedly around the Parkfield M6 asperity, and this is evident in both GR statistics and seismicity rates. Some intriguing results are also presented on changes in relative slip rates inferred from the characteristic behavior of the microseismicity. The aspects of propagation considered include travel-time, vector wavefield polarization, and Δ coda Q.

SEISMICITY

The set of Parkfield microearthquakes (and its subset of characteristic subcluster sequences) provides very sensitive measures of change in seismicity, occurrence/recurrence patterns, and their statistics. As reported in previous chapters, various aspects of seismicity have shown strong non-stationary behavior since about 1992. The changes include a significant increase in microseismicity rate and a deepening in seismicity (Fig. 5.1a), an increased proportion of larger microearthquakes -- manifest as decreased B-values (Fig. 4.2c), a decreasing proportion of clustered seismicity to non-clustered seismicity (Fig. 3.7), and an increase in M3+

seismicity in the vicinity of Parkfield (33, 34). These changes correlate with the Vibroseis monitoring studies (24) (Fig. 5.1b) which sample the propagation medium about every 3 months. They also seem to correlate with some changes seen in the microseismicity occurrence patterns, including changes in the regularity and average duration of recurrence-times for some characteristic sequences. These variations, discussed next, suggest that changes take place deep and in the vicinity of the M6 nucleation region.

Patterns of cluster occurrence and characteristic subcluster recurrence-time show obvious changes beginning around 1992. A common observation, promising in terms of understanding physical fault-zone process, is illustrated in Fig. 5.1c, where the average recurrence-time of some characteristic sequences appears to exhibit greater scatter and shorter average duration in concert with significant changes in seismicity rate and distribution (Fig. 5.1a). An example of change in occurrence patterns is shown in Fig. 5.2 , where the occurrence/recurrence pattern of a 2-event-type cluster exhibits a step change in pattern and average recurrence interval. Initially the pattern for this sequence involved a series of same-day double events separated by intervals of ~640 days. The double events were separated spatially by about 10 m, with the first event being ~3-4 times larger than the second event. Somewhere between mid-1991 and early 1993 this pattern suddenly changed taking on a single-event-type recurrence pattern with the single event type essentially identical to the larger event type of the earlier pattern except for a ~25% increase in moment (almost as if the moments of the previous pairs were

combined), and a dramatically shortened recurrence interval ensued (now at ~285 days). This type of pattern change, though striking, less common and difficult to model mechanically using steady-state slip accumulation.

Fig. 5.1 [three pages] a.) 2-month running window of total seismicity (Solid curve) and ratio of deep to shallow events (dashed) for Fall 1987-1994 inclusive. b.) Relative travel-time delays of S-wave coda arrivals observed in the Vibroseis experiment for paths to several stations from VP3 (24). Dates of significant occurrences in seismicity (swarms and M4+ activity) are indicated. c.) Sample time lines of recurring sequences in the part of the study area experiencing significant temporal change in recurrence-times, (zone A in Fig. 5.1f). Contrast this with the regularity observed for the timelines of events in zones B and C (Fig. 5.1g). d.) Series of time evolution plots -- labeled A-D -- for recurrence statistics of combined sequences in the corresponding regions of the fault zone identified in Fig. 5.1f. Here the lognormal recurrence statistics of chapter IV are used as parameters for monitoring temporal stability in the duration and scatter of median normalized recurrence-times -- intrinsic uncertainty, σ_I; recurrence bias from average, μ_D; and number of intervals considered in the moving time window statistic, intvl. -- by moving 2.5 year analysis windows down the timelines. Values of σ_I and μ_D correspond to ordinate values shown at left and are dimensionless. e.) Time evolution plot for recurrence statistics of all 4 sequences combined. f.) Along fault seismicity section with superimposed P-velocity model. Letters A-D show the 4 areas where characteristic sequences contributing to the recurrence statistics of parts d.) and e.) are located. g.) Sample timelines of events in zones B and C illustrating the predominant regularity of recurrence-times for characteristic sequences in the NW portion of the fault zone.

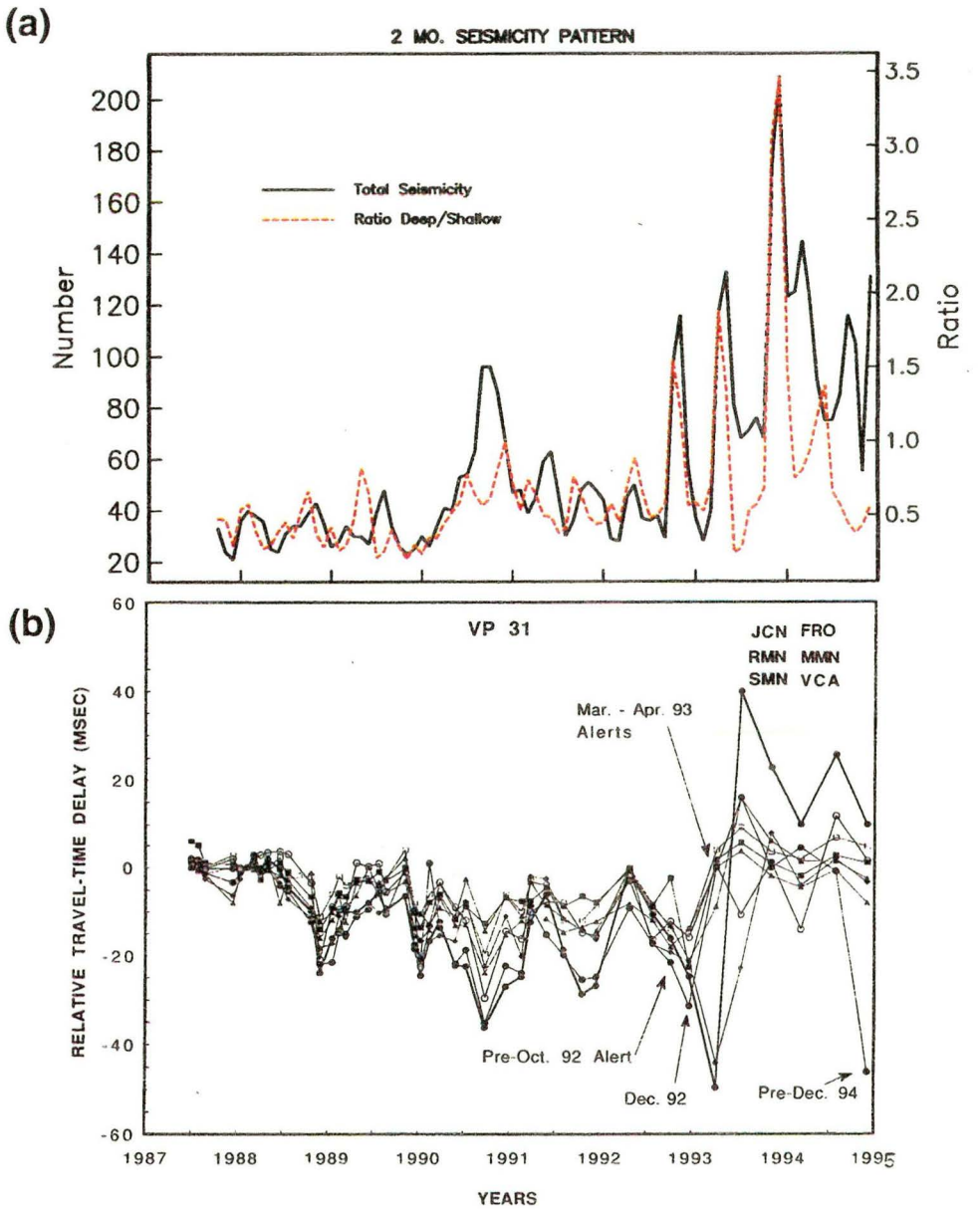
(a)
2 MO. SEISMICITY PATTERN
Number
Ratio
Total Seismicity
Ratio Deep/Shallow
(b)
VP 31
JCN FRO
RMN MMN
SMN VCA
Mar. - Apr. 93
Alerts
Pre-Oct. 92 Alert
Dec. 92
Pre-Dec. 94
RELATIVE TRAVEL-TIME DELAY (MSEC)
YEARS
(c)

(d)

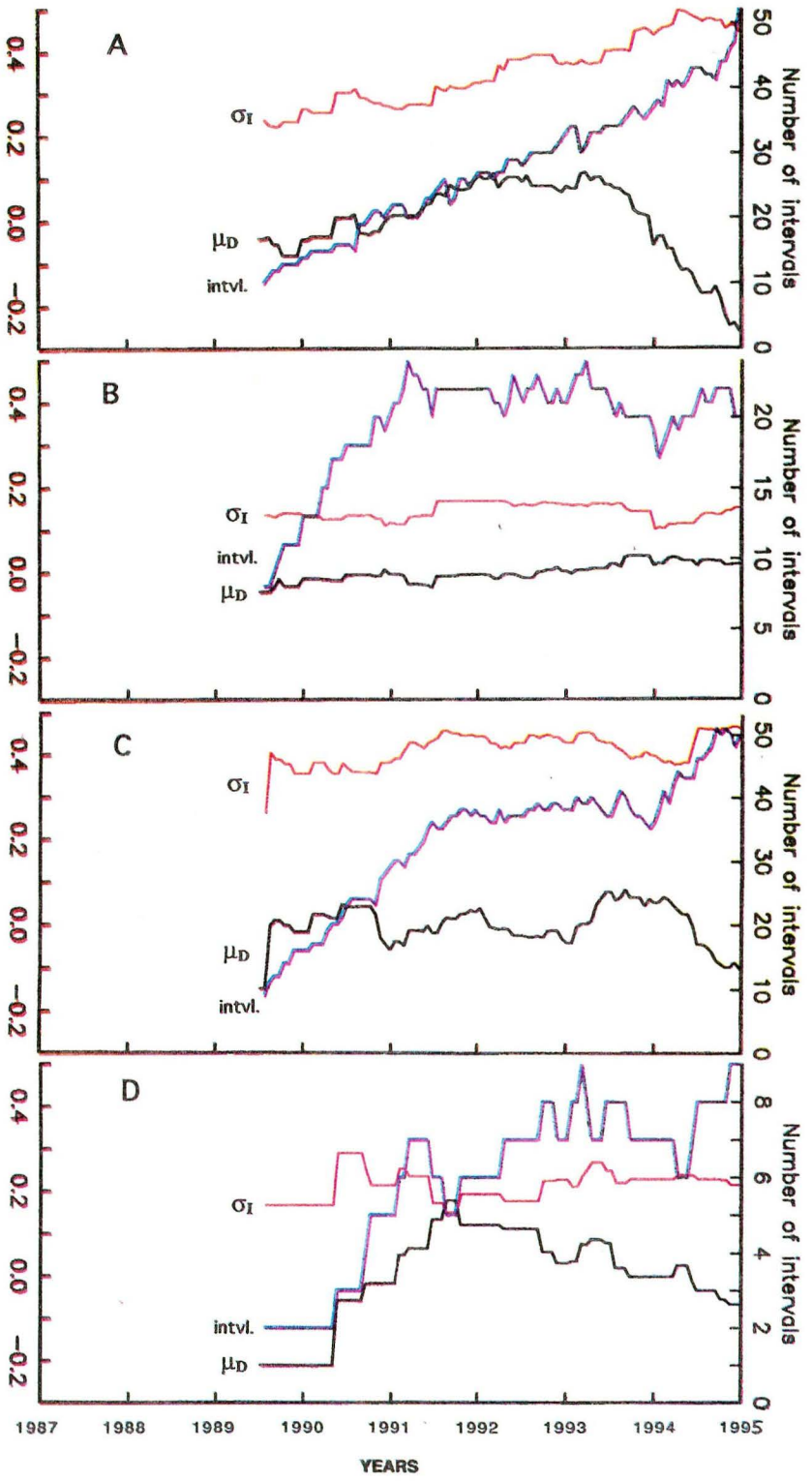
A
B
C
D
σI
μD
intvl.
0.4
0.2
0.0
−0.2
Number of intervals
1987
1988
1989
1990
1991
1992
1993
1994
1995
YEARS

(e)

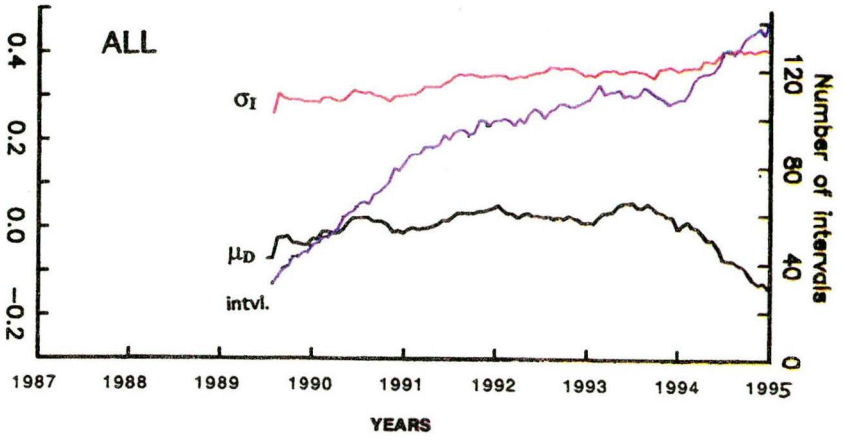
ALL
σI
μD
intvl.
0.4
0.2
0.0
−0.2
120
80
40
0
Number of intervals
1987
1988
1989
1990
1991
1992
1993
1994
1995
YEARS

(f)

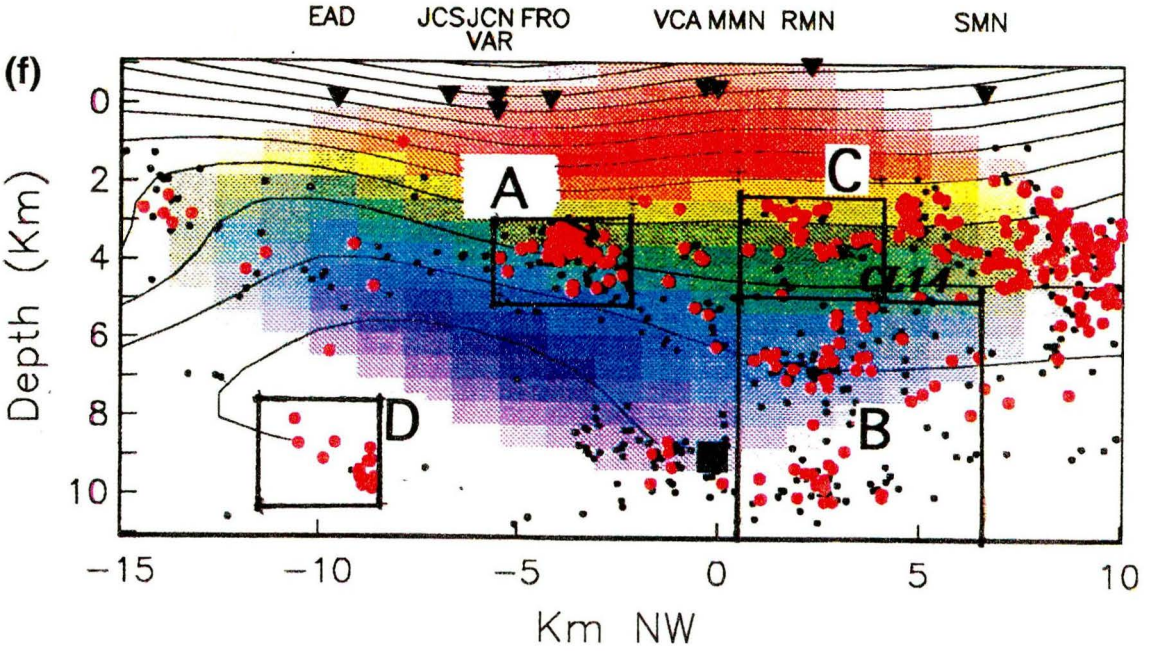
EAD
JCS
JCN
FRO
VAR
VCA
MMN
RMN
SMN
A
B
C
D
Depth (Km)
0
2
4
6
8
10
−15
−10
−5
0
5
10
Km NW

(g)

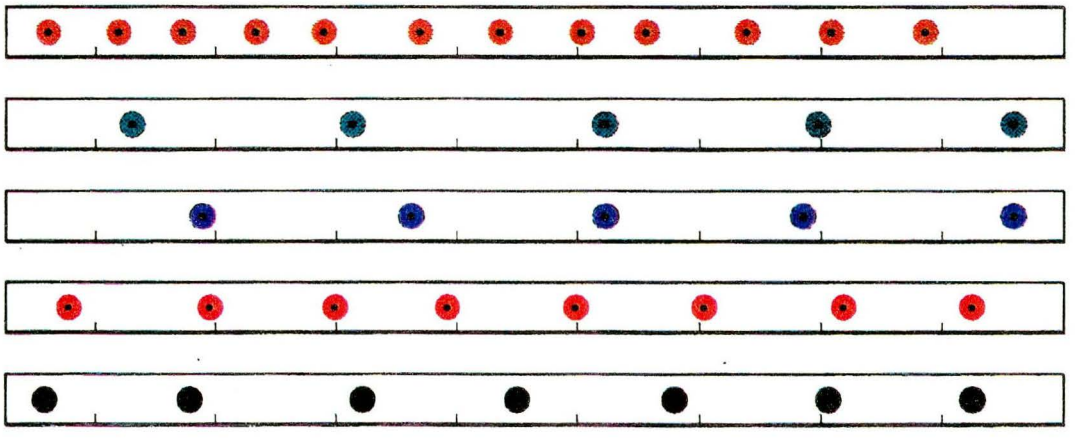

Fig. 5.2 Timeline and seismograms for a cluster experiencing a sudden change in its occurrence/recurrence behavior beginning around 1992. Timeline goes from 1987-1994 and shows that the first 6 events occur as doublets separated by ~640 day recurrence times. Numbers on the far right show relative peak amplitudes of the cluster events. Dates under each waveform give year and Julian day of event occurrence. The cluster is located in region A of Fig. 5.1f where the most noticeable seismicity changes are located and approximately where Karageorgi et. al. (24) observe temporal propagation changes using Vibroseis.

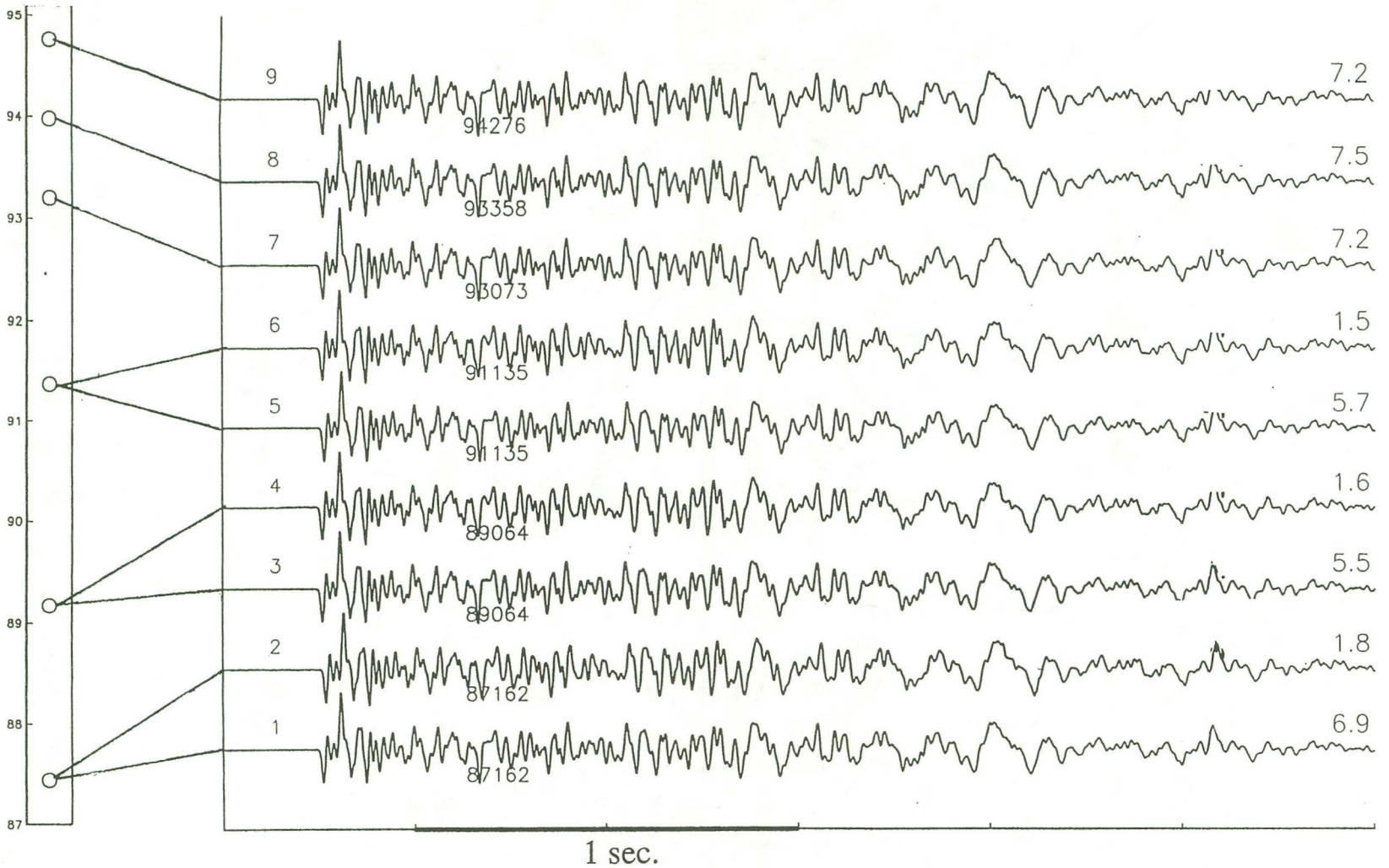
95
94
93
92
91
90
89
88
87
9
8
7
6
5
4
3
2
1
94276
93358
93073
91135
91135
89064
89064
87162
87162
7.2
7.5
7.2
1.5
5.7
1.6
5.5
1.8
6.9
1 sec.

The changes illustrated in Fig. 5.1c from a sample of characteristic sequences located in region A of Fig. 5.1f, involve a decrease in the average recurrence interval beginning around 1991-1992 along with a simultaneous increase in the irregularity of the recurrence intervals. These changes are not uniform from sequence to sequence, however, so to obtain a more stable estimate of the changing areal recurrence behavior the lognormal recurrence statistics discussed in chapter IV -- σ_l and μ_D -- are used to assess the gross non-stationarity of recurrence-times. In earthquake forecasting these statistics are assumed to be stationary, however, recurrence-times in localized regions vary in a non-stationary way.

In the analysis, median normalized recurrence statistics are first assembled for all characteristic sequences in a predefined area and occurring during the 8 year (1987-1994) analysis period (in Fig. 5.1d the analysis was performed for 4 different regions A-D individually and then collectively in Fig. 5.1e). The areal recurrence intervals are then organized chronologically and intervals whose terminating events lie within a specific time window (here chosen to be 2.5 years) are used to estimate μ_D and σ_l which are plotted at the leading edge of the analysis window (Fig. 5.1d and e). The choice of window length reflects a tradeoff between time resolution and obtaining an adequate sampling for stable estimates of σ_l and μ_D. The μ_D statistic for an unbiased sample of intervals should be zero; however, a temporally changing average recurrence interval will cause μ_D to be biased for 2.5 year windows. The bias reflects change in the areally averaged recurrence interval and since we are

working solely with characteristic events, this bias can be related to slip rate at depth using equations (e1) and (e6) of chapter IV. This allows us to infer that region A has experienced an average 10-20% increase in slip rate (i.e.. decrease in recurrence interval) since about 1991-2; while, slip rates in area B have remained essentially constant. σ_I values -- representing scatter of the recurrence statistic -- have also shown a marked increase in area A during the same time period with very little change in areas B-D. We also observe an increase in the number of total intervals over the 87-94 period (Note that since the HRSN did not fully come on line until January 1988, and since we use a 2.5 year analysis window, the portion of the curves before mid-1990 shown in 5.1d and e may reflect incomplete sampling).

REPEATING CHARACTERISTIC MICROEARTHQUAKES

The large numbers of well distributed Parkfield characteristic microearthquakes affords an unprecedented opportunity for monitoring temporal changes in elastic wave propagation parameters. Here earthquakes are used to illuminate the medium of interest (see (1, 2) for examples of similar studies using artificial sources). Previous studies used event pairs taken from spatially clustered earthquakes because they minimize uncertainties in source location and source variability. In addition, spatially clustered earthquakes also frequently cluster in time, thus providing localized groups of event pairs containing a mixture of both long and short time separations. Comparison pairs separated by very short time intervals can be used to determine the temporal resolution of a

particular technique since temporal changes in the propagation medium are assumed to vary little over short time spans (3, 4, 5). Results of chapter III, however, suggest that short time base pairs at Parkfield invariably involve two distinctly different event types in the same cluster (Fig. 3.6), which produce effects that remain significant even after corrections designed to minimize the source effects are used (5, 12) and despite the fact that the differing event type cluster members

are <20m apart and have maximum cross-correlation values >0.98. To illustrate this point, consider Fig. 5.3, where spectral ratios are shown for a data set of event pairs of the same and differing event types (see Figs. 3.1, 3.4, and related discussions). The centroid location of event type-1 differs from that of event type-3 by about 10 m -- a hypocenter separation of the same order as the hypocenter separation between same-type pairs. The P-wave spectral ratios in Fig. 5.3 suggests that, while same-type sources are practically identical (with ratios flat out beyond 80 Hz), differing, nearly co-located, event types have clearly different source attributes and which, in this case, differ oppositely in frequency content at the two stations, likely indicative of a change in directivity between the event types and not differences in source corner frequencies (7, 8).

The results presented in this chapter are, to a large extent, unaffected by these uncertainties (given rise to by mixing of event-types), since the microearthquakes used are same-event-type pairs which conform to the idealized characteristic earthquake criteria (6) -- occurrence on the same

asperity, similar rupture histories, similar sizes, quasi-periodic recurrence and with similar amounts of seismic slip. Under these conditions, the time-dependent changes observed in seismograms of characteristic event pairs are due primarily to temporal change in the propagation medium (assuming stationary recording system response).

Fig. 5.3 Vertical component P-wave spectral ratios at (a) VCA and (b) MMN for pairs of events from event types 1 and 3 within the same cluster (see text). Ratios are computed for a 0.5-sec window surrounding the P arrival. The type-1/type-1 and type-1/type-3 ratios have been shifted by a factor of 1/3 and 1/10 respectively for clarity. Only ratios between the same-type event pairs show flat (similar) spectra over the entire frequency band, indicative of identical source characteristics and very small differences in moment. The type-1/type-3 ratio shows a negative slope at VCA and a positive slope at MMN, indicating directivity differences between the two sources.

(a)

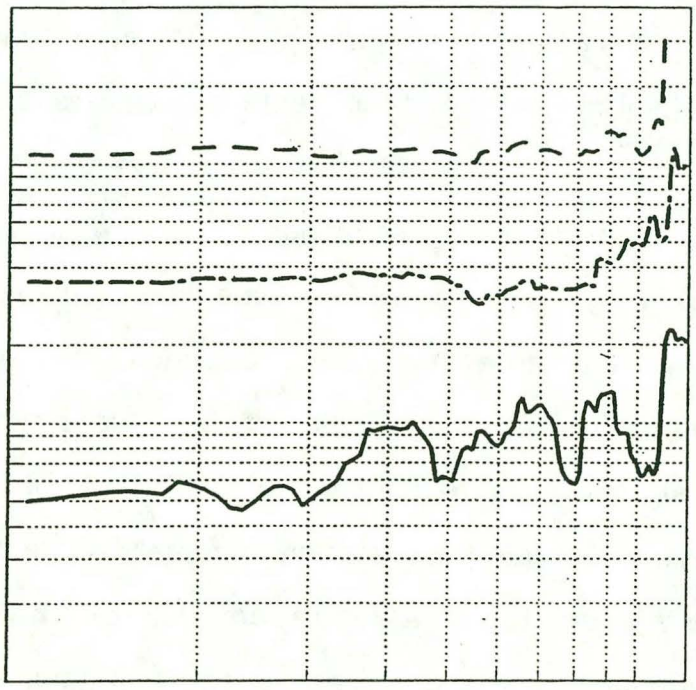

(b)

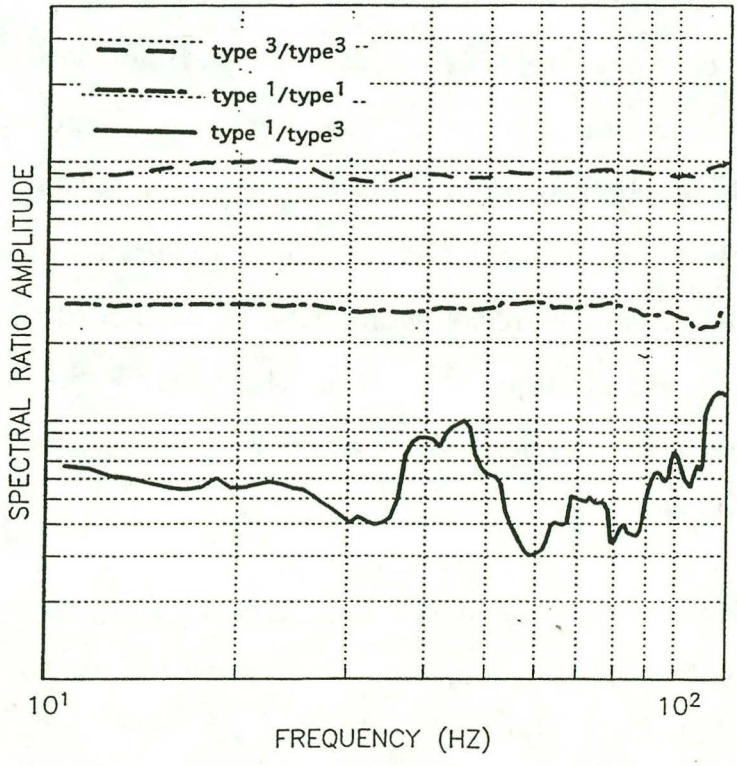
type 3/type3
type 1/type1
type 1/type3
SPECTRAL RATIO AMPLITUDE
10¹
10²
FREQUENCY (HZ)

Certain wave-propagation paths for same-type event pairs show temporal variability in seismograms comparable to or greater than the variability observed for seismograms from different-type event-pairs but having small time separations and which propagate along more stable paths. Fig. 5.4 illustrates this by displaying seismograms of 7 events from the same cluster used in Figures. 3.1 and 5.3. Same-type events separated by long time intervals are more stable on recordings from VCA than those recorded on FRO while pairs of different event types separated by short time intervals show comparable amounts of variability between the 2 stations. Hence, certain paths remain extremely stable over time (a fact which allows us to identify repetitions of the characteristic microearthquakes) while other paths show change in response to variations in stress or dilatant effects (9, 10, 21, 22, 23) -- possibly related to the nucleation of the expected Parkfield M6 -- or to site-specific variations. For surface instruments, and especially at high frequencies, site-specific changes are usually observed and can be correlated with effects of ground saturation, seasonal change or cultural noise (11,13). However, the borehole sensors of the HRSN greatly reduce these effects, a fact which is confirmed by the multiple observations of repeating sequences of virtually identical events whose waveforms have remained largely unaffected through time. This strengthens the argument that observed localized propagation changes are related to stress or strain changes at depth.

In sum, I have shown that the characteristic microearthquake source criteria provides virtually identical illumination sources with sufficient

repeatability to significantly improve the resolution in assessing temporal changes in wave-propagation characteristics over source selection criteria now commonly in use. This criteria largely overcomes tradeoffs and uncertainties associated with source location and rupture history. The stability observed along certain propagation paths contrasts with variability seen along others, suggesting localized temporal change, which I use in the remainder of this chapter to investigate localized temporal stability in travel-times, vector wave polarizations and Δ coda Q, at Parkfield.

Fig. 5.4 Select seismograms of 7 events from the same cluster, CL14, as that used in Fig. 5.3 (see chapter III; Fig. 3.3) and recorded at stations VCAz (stable path) and FRO2 (unstable path). The lower 3 waveforms (events 1, 2, and 3) of (a) and (b) each belong to different event types (types 1, 2 and 3, respectively) and occurred within 3 days of one another. The upper 5 waveforms (3-7) are from the same event type (event type -3 of Fig. 5.3) and occurred repeatedly with fairly long time base separations -- cumulatively spanning over 6 years. Note the relative seismogram instability of waveforms 3-7 at FRO compared to VCA. By contrast the relative variability between event types 1-3 -- with short time separations -- does not differ significantly between the two stations. (a) and (b) illustrate how propagation along some travel paths remains very stable over long periods of time (i.e.. events 3-7 at VCA) while others are stable only over short time intervals. Numbers at left are in time order of events, those at right are relative peak amplitudes.

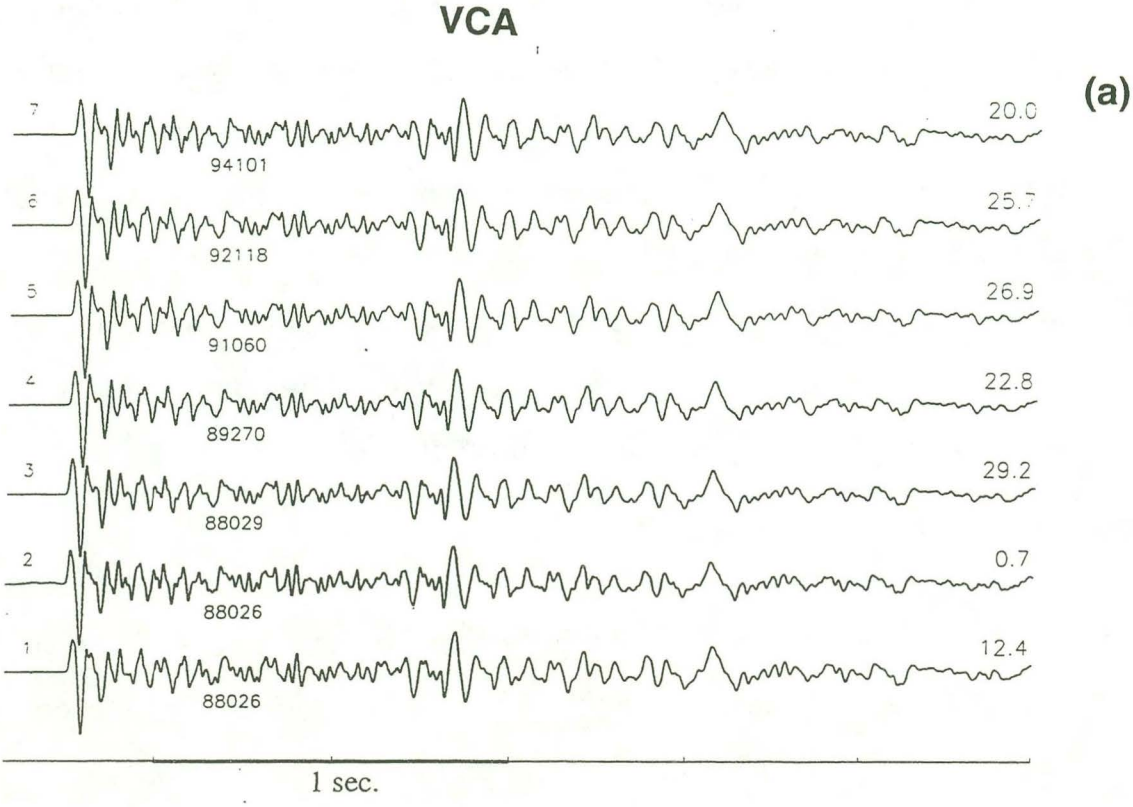
VCA
(a)
7
94101
20.0
6
92118
25.7
5
91060
26.9
4
89270
22.8
3
88029
29.2
2
88026
0.7
1
88026
12.4
1 sec.

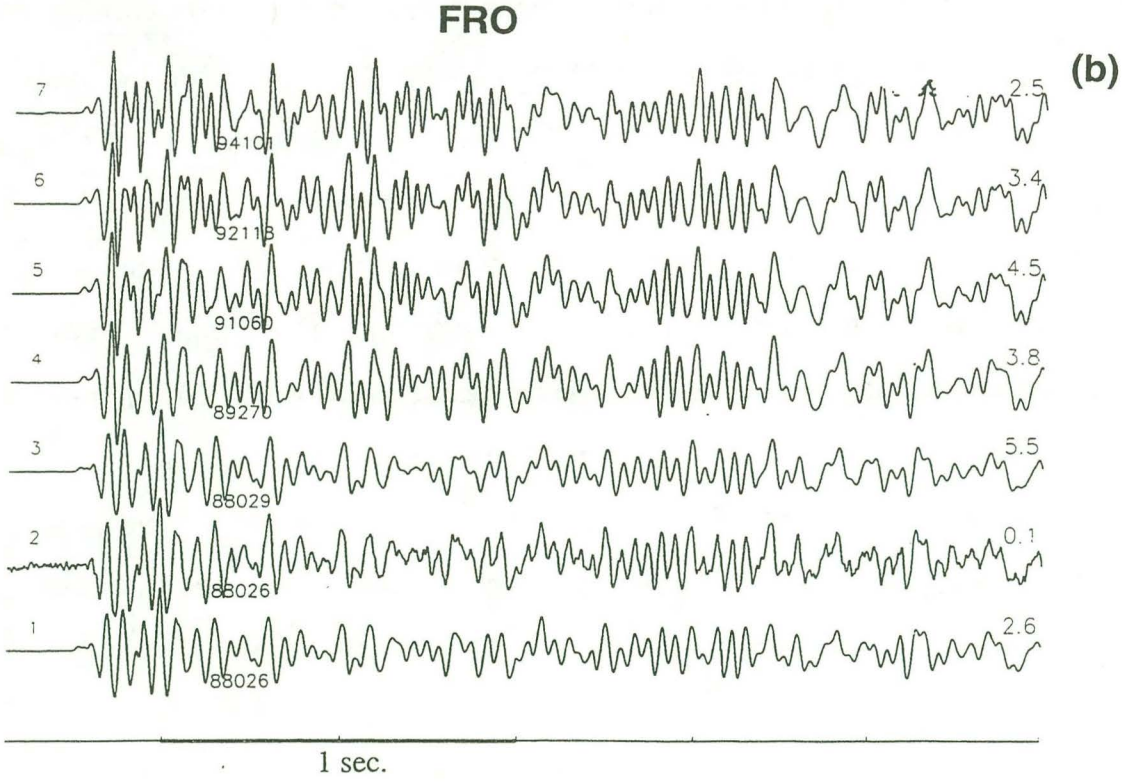
FRO
(b)
7
94101
2.5
6
92118
3.4
5
91060
4.5
4
89270
3.8
3
88029
5.5
2
88026
0.1
1
88026
2.6
1 sec.

TRAVEL TIMES

In chapter II we analyzed travel-time stability to a resolution of about +/- 2-4ms using a continuous cross-correlation analysis and mixed event-type clusters (see Fig. 2.11 and related discussion). Here I report on an expanded and more well-resolved version of that preliminary work. By integrating the high-resolution timing technique and continuous time delay analysis described in chapter II (Figs. 2.6 and 2.11) and by using only characteristic same-type event comparison pairs, the uncertainties in the continuous travel-time method can be significantly reduced. Briefly, following Poupinet et al. (37), a reference trace from one event for each cluster is cross-correlated with waveforms from every other cluster member to provide an initial alignment of the traces (Fig. 5.5a). A 0.5 second window is then stepped down the two traces in 16 ms increments, the lag of the correlation maximum gives the offset between corresponding time windows, and the relative time delays between the two waveforms are computed to sub-sample precision from the slope of the phase of the cross spectrum between the two traces (see Fig. 5.5b and c). The delay-times are then presented in trace time aligned on the P-phase and displayed in color (5.5d).

Fig. 5.6 illustrates the apparent gain in precision using the method, a potential resolution of order +/- 0.4ms (nearly an order of magnitude improvement over the cross-correlation results in chapter II). We assess the uncertainties in the subsample timing delays by computing relative delays about the P-phase for windows centered at each sample point of the first one-half cycle of the P arrival. The spread of the resulting

distribution of values gives a comparative measure of stability of the method. In Fig. 5.6 delays between same event type (a) and different event type (b) pairs illustrate the stability of the delay estimate for same-event-type pairs in contrast to a 3 to 4 times greater spread observed for delays between different-event-types even though all events satisfy the <20m separation and maximum cross-correlation of > 0.98 criteria.

Fig. 5.5 Illustration of the cross-spectral technique (37) for subsample precision travel-time analysis. In this illustration, steps a, b, and c are shown only for the P and S windows indicated. Time shift between moving time windows (a) are computed using the slope of the phase of the cross-spectrum (b) over a frequency band determined by high coherence (c). For a series of moving windows stepped down the waveform pairs, the resulting delay time series along the traces is displayed in color (d) (a different reference trace from those in (a) is shown).

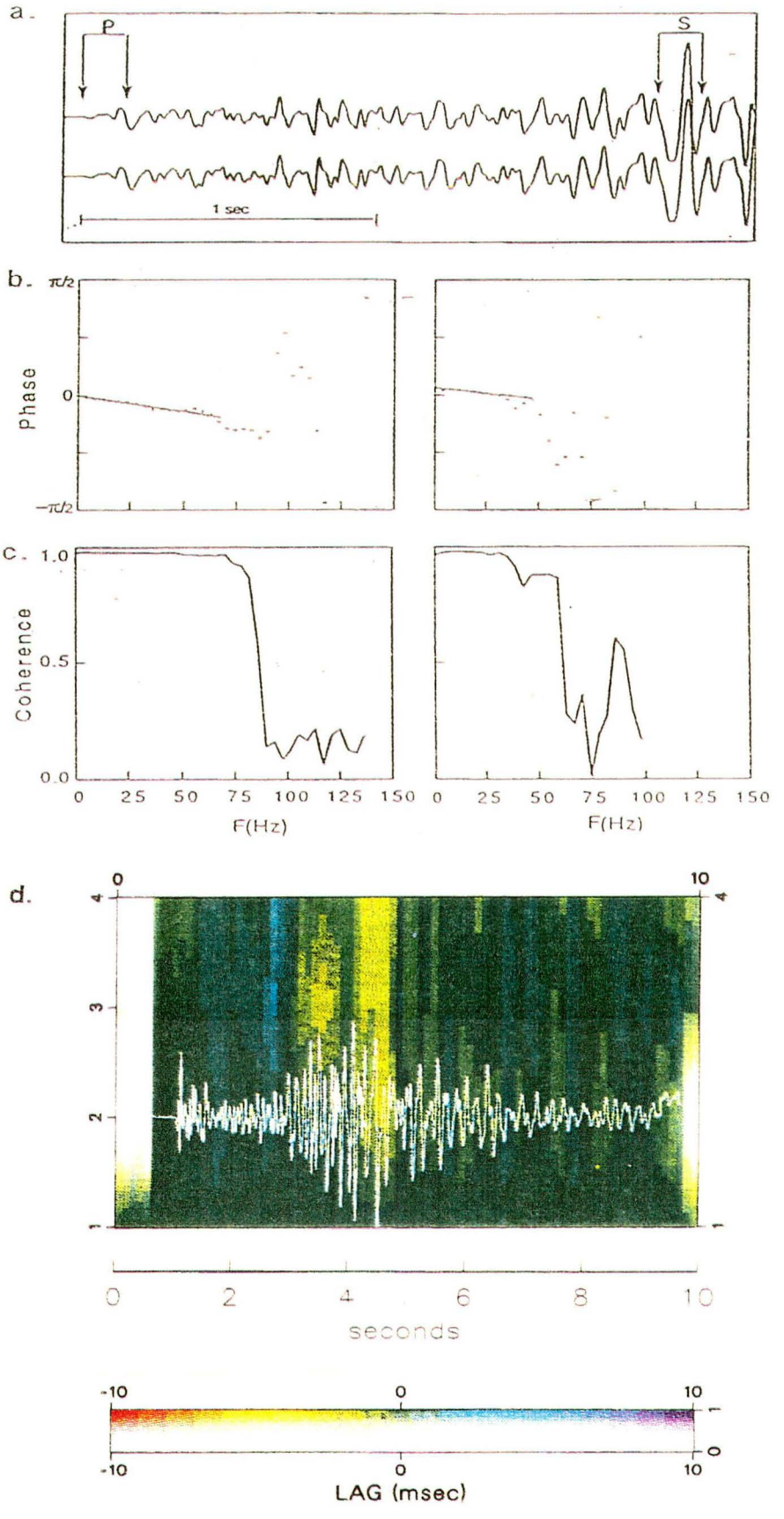
a.
P
S
1 sec
b.
π/2
Phase
0
−π/2
c.
1.0
Coherence
0.5
0.0
0 25 50 75 100 125 150
F(Hz)
0 25 50 75 100 125 150
F(Hz)
d.
0
10
4
3
2
1
0 2 4 6 8 10
seconds
-10 0 10
1
0
-10 0 10
LAG (msec)

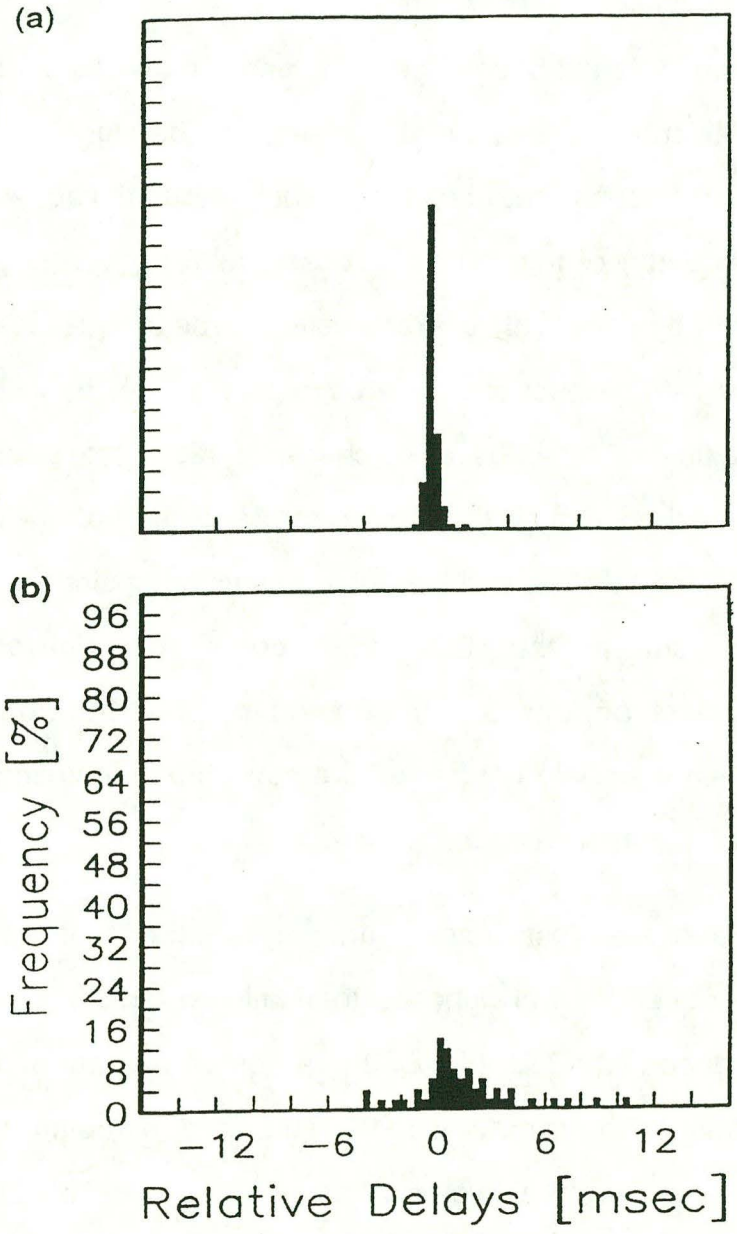

Fig. 5.6. P-time delay distribution for cross-spectral analysis windows centered on samples of the first 1/2 cycle of the P-arrival. (a) delay distribution between two type-3 events and (b) between a type-1 and type-3 event. Delay bins are 1/5 the sampling interval (i.e. 0.4ms).

Hence, the effects of different source locations and rupture histories, even within highly similar and localized event clusters, can be significant. The travel times are further complicated by the asynchronous timing (+/- 1 ms sample time uncertainty) of the HRSN. These problems can largely be overcome, however, by using only characteristic microearthquakes and by taking time delays with respect to a reference phase (e.g. P) instead of apparent absolute time. This is because characteristic microearthquakes are near-identical and co-located (at least to the resolution of our relative location method -- +/- 5 to 10m) and because (assuming stationarity of the asynchronous time shift for the 12 second records) the relative phase arrival times on seismograms are unaffected by asynchronous time wander (e.g. S-P times remain unaffected the asynchronous timing, while the individual P and S travel times can wander).

For this study, five well-distributed, multiple-member characteristic microearthquake sequences were chosen to illuminate regions of interest at Parkfield (sequences A to E in Fig. 5.7) in a search for change in both travel-time and polarization (next section). This study examines travel-time changes along the entire waveform between members of repeating characteristic earthquake sequences whose occurrence times span the beginning and end of a three year drought and two M4+ earthquakes.

Fig. 5.7 Map and cross-sections of seismicity showing the five characteristic sequences, A to E, used in both the travel-time and polarization studies. The 3-D Vp/Vs-velocity model (25), significant recent seismicity (red dots) and the 1966 M6 event (red asterisk) are shown.

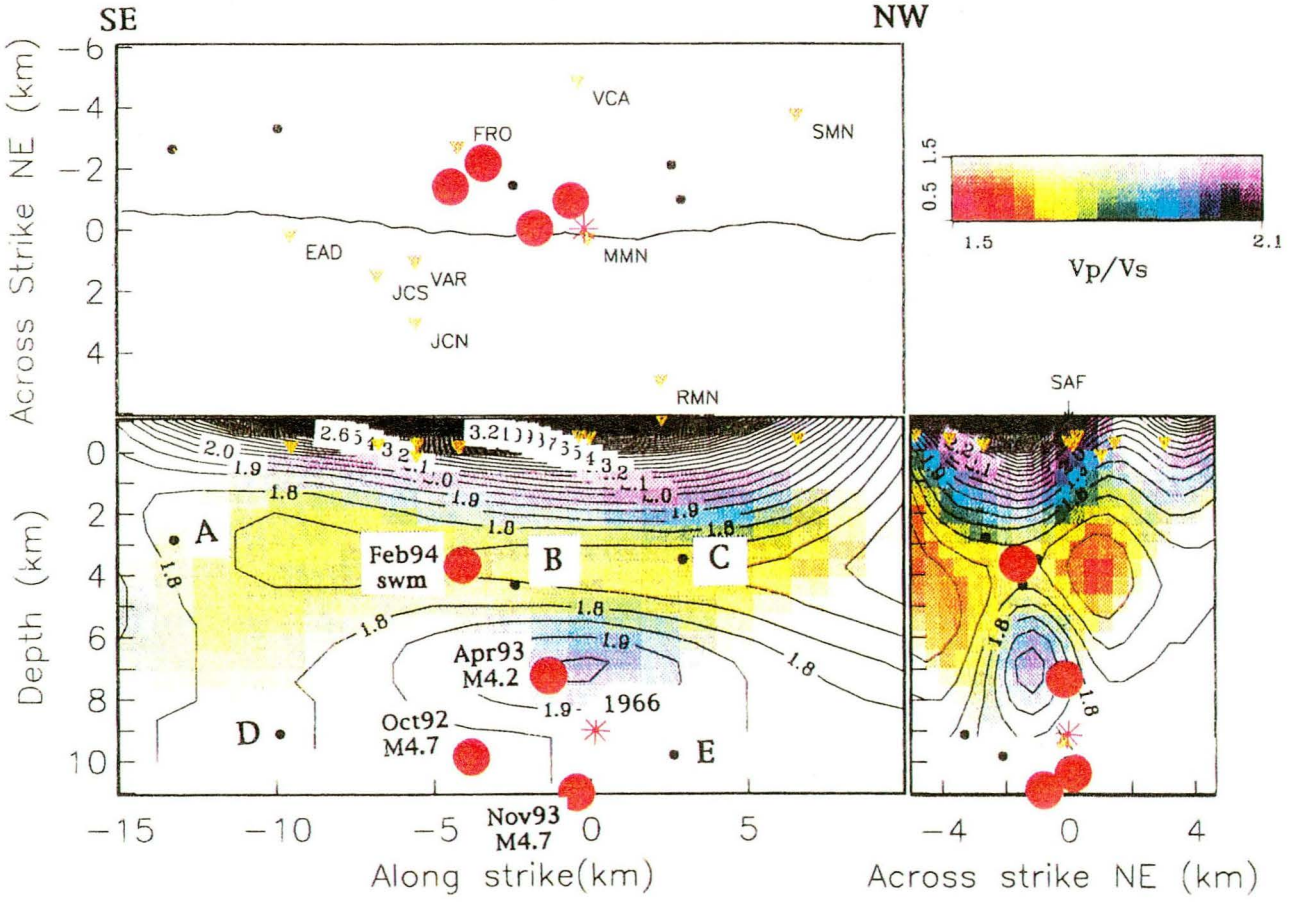
SE
NW
Across Strike NE (km)
Depth (km)
VCA
SMN
FRO
EAD
MMN
VAR
JCS
JCN
RMN
SAF
0.5 1.5
1.5
2.1
Vp/Vs
A
B
C
D
E
Feb94
swm
Apr93
M4.2
1966
Oct92
M4.7
Nov93
M4.7
Along strike(km)
Across strike NE (km)

Regions illuminated by sequences A through D showed little evidence of systematic change in travel time. Subtle scattered changes were observed however, indicating possible non-stationarity in the propagation velocities in those regions. Of the 5 illuminating sequences, E had the best S/N and sampled the proposed nucleation zone of the expected Parkfield M6 most heavily (Fig. 5.8a). Travel-time delays from that source do show modest systematic travel-time change (Fig.5.8b). Specifically, seismograms from the first 3 events in the sequence show essentially no variation in travel time to any stations, but paths to MMN, JCN and EAD -- those which sample the nucleation zone and locations of recent large earthquakes most directly -- exhibit significant travel time delays occurring especially between events 3 and 4 which bracket the large M4+ event in October of 1992 (Fig. 5.8b). This suggests that the stress changes associated with the M4.7 in Oct. of 1992 or just prior to the M4.2 in Apr. 1993 produced a net increase in local seismic velocities. The effect is small -- on the order of a few parts in 10^4 -- and since future changes may be no larger than this order, subtle source differences (even among characteristic events) may prove to be a limitation for the method. These variations are seen in a similar location as those reported using Vibroseis (1, 24).

Fig. 5.8 [3 pages] a.) Map and along-fault section views of study area with P ray-paths to the 7 stations whose seismograms where used in the travel time analysis of sequence E. Also shown are the sites of recent significant seismic activity (red dots) and Vp/Vs model (25) showing low Vp/Vs in the vicinity of expected nucleation region (area of blue-purple concentric elliptical contours) and the location of initiation of the 1966 main shock (red asterisk). b.) Timeline (1987 to 1994; bottom to top) showing occurrence times of the 4 characteristic events of sequence E and recent significant seismicity(red dots). Note, the M4.7 event of Oct. 1992 and the M4.2 of Apr. 1993 occurred between and just after the sampling events 3 and 4. Left panels of c.1) and c.2) show travel-time delay plots computed for 9 seconds of the event seismograms following P for sequence E, with 1 second of pre-event trace. A sample seismogram from event 2 of the sequence is superposed in white on the color displays. The chronological event numbers for events in the sequence are shown on the left, and color scales for lag times and polarization azimuth are as in Figs. 5.5 and 5.9 respectively. High color saturation indicates a strong cross-correlation between the reference event (event 1) and later occurring members of the cluster. Low saturation indicates low maximum cross-correlation values (e.g. the preevent and late portions of the plots shows white due to low coherency). The P-phase of the delay time series were aligned with subsample precision (+/- 0.4 ms) whereas in chapter II (Fig. 2.11) alignment was done visually to the nearest sample (+/- 2-4 ms). Also, in the earlier study, events were not restricted to be of the same-event-type and only ~4 sec of data were displayed. Note that two components of station VCA (i.e.. Z and H1) are displayed for comparison.

Right panels (see next section) are 3-component polarizations plots for 10 seconds of data, with the P and S phase arrivals indicated. The anomalous yellow-green shading of event 2 at VCA is an artifact of the H2 component recording at an anomalously low amplitude (~ x1/4) for that event. This problem was not recognized until the Polarization analysis was performed, and highlights another benefit in using vector waveforms of characteristic sequences for temporal change studies -- many previously unrecognized network glitches become apparent and are correctable.

(a)

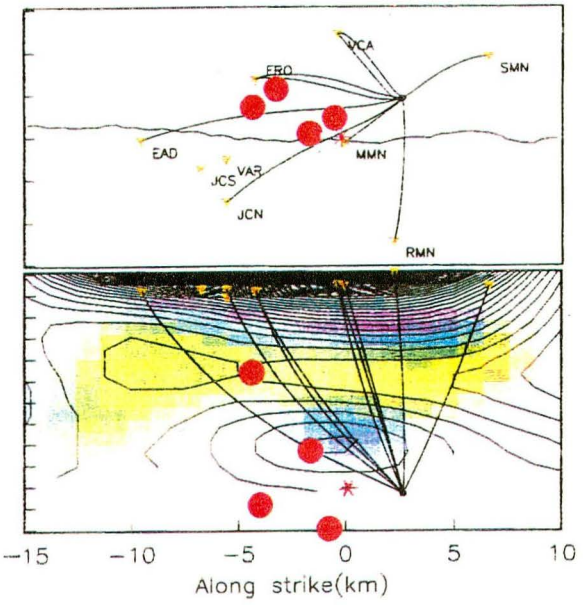
VCA
ERQ
SMN
EAD
MMN
JCS
VAR
JCN
RMN
−15
−10
−5
0
5
10
Along strike(km)

(b)

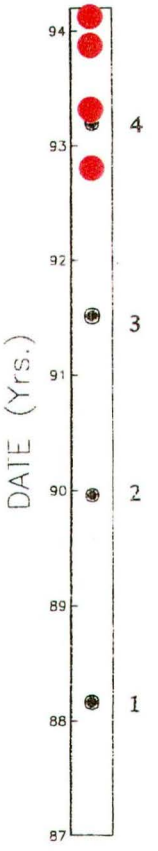
94
93
92
91
90
89
88
87
DATE (Yrs.)
4
3
2
1

(C.1)

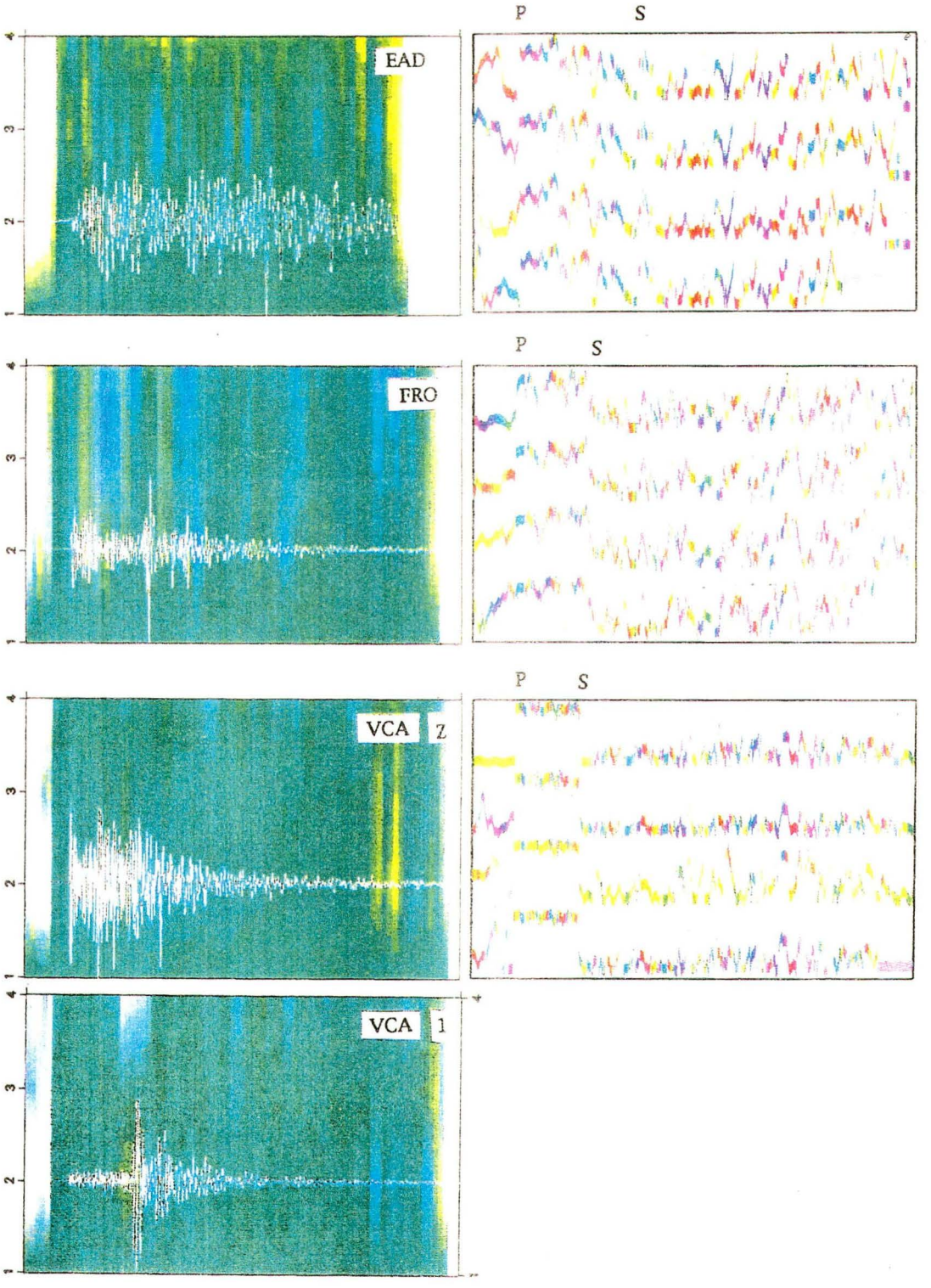

(C.2)

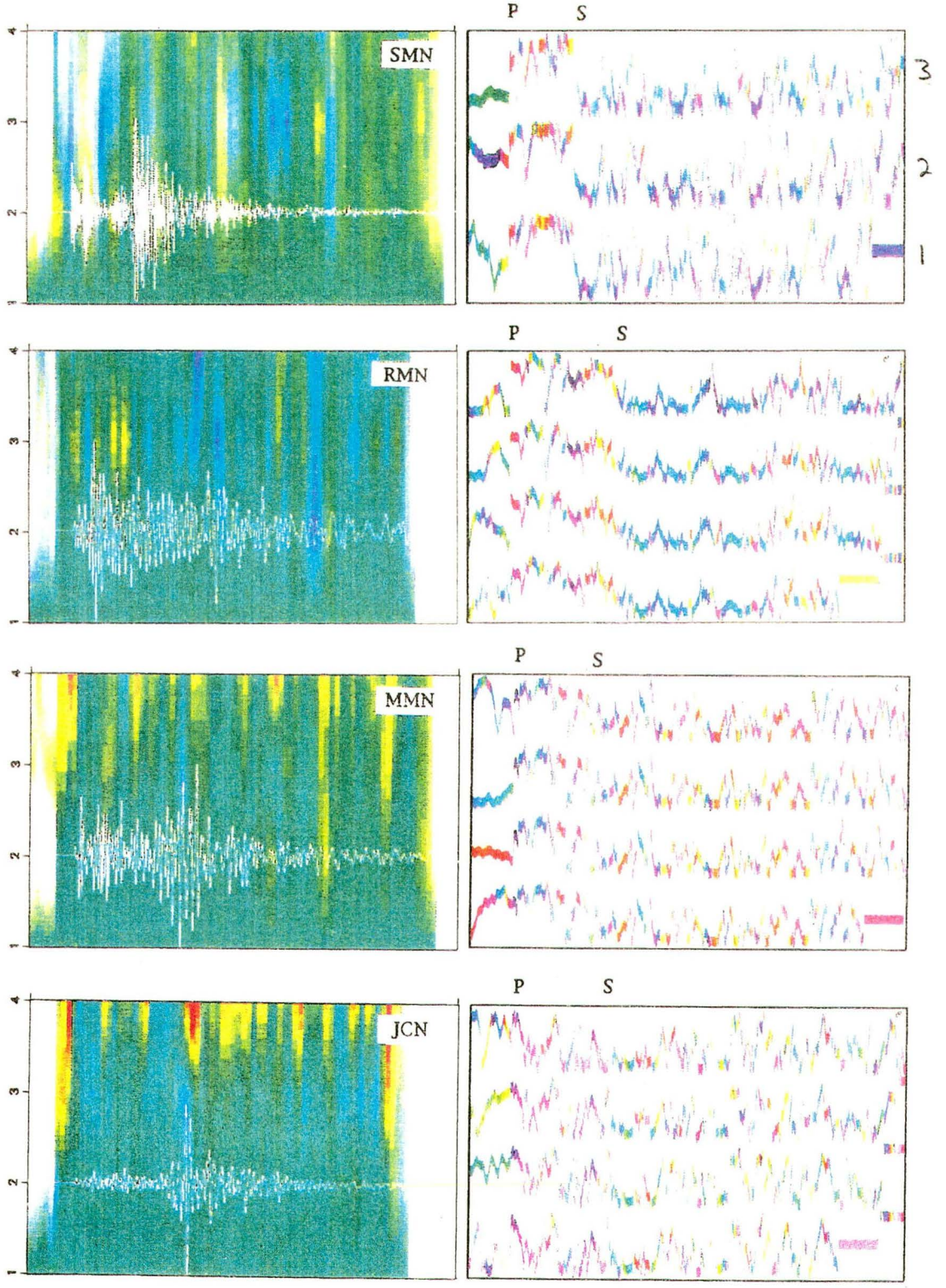

POLARIZATION

The instantaneous polarization of a vector waveform is a function of 3-D amplitudes and phase. Polarization is sensitive to factors affecting amplitudes and travel times of elastic wave energy in 3-D, including multipathing anisotropic attenuation, velocity anisotropy, single and multiple scattering, source mechanisms, and path specific propagation velocities and attenuation. Because of these multiple dependencies, waveform polarization is more likely to reveal temporal change in the medium than either travel times or attenuation alone. Polarization change, however, is the most difficult to interpret in terms of specific physical causes. Various researchers have shown that physically meaningful information regarding seismic propagation can be extracted from the S-wave train through modeling of S-wave alignment and birefringence caused by anisotropic velocity structure (13, 27, 28). Velocity anisotropy may be due to either intrinsic rock properties, subsurface crack density and orientation, or both.

We reported in chapter II (Fig. 2.14), that sudden 90 degree polarization changes in the microearthquake S-wave trains are commonly observed at Parkfield, suggestive of fault-aligned seismic anisotropy, someplace below the borehole sensors (~200m). Similar results have been reported for controlled-source studies in the area (1, 26). The inferred anisotropy has only been unambiguously observed for microearthquakes at the MMN site located directly on the San Andreas Fault (SAF) and in the nearby Varian well survey (26). The possibility remains that the polarization shifts may be explained in terms of interfering fault-guided waves (18, 29).

As with other propagation studies, progress with polarization has also been hampered by the uncertain tradeoffs between source location and mechanics (e.g. temporal changes at Anza and at Parkfield have been reported by (30, 31), but later work of (32) and this study show those results are likely to be based on incorrect phase identification or interpretation of arrival times due to contamination by tradeoffs. To avoid these problems, I use the previous set of 5 repeating sequences of characteristic microearthquakes and a modification of the polarization analysis used in chapter II (Figs. 2.13 and 2.14). The time-variable polarization characteristics are examined by comparing vector linearity traces which represent polarizations in trace time (Fig. 2.13). A 100 ms boxcar window is moved down the 3-component waveform in 2 ms steps. Vector linearity is computed from the 3-D particle motion. The resultant pseudo-vector is plotted on the color trace as a shaded and colored pixel at the center of the time window. The vertical axis represents the vertical projection of the linearity vector (incidence angle), while the color hue of the pixel reflects the vector azimuth in the horizontal plane. The color saturation represents the magnitude of the linearity. This type of display allows simultaneous investigation of wave type, scattering, propagation direction, and anisotropy. Near-vertical incidence (<30 degrees from the vertical) is expected for all direct arrivals given the array geometry and the velocity model of (25) (see raypaths in Fig. 5.8a)). Results are shown in Fig. 5.8 c.1 and c.2 (left panels).

Similar systematic variability to the travel-time data is present although difficult to see in these types of display due to the high degree of

polarization variation in the high-frequency data. Also, the polarizations are necessarily determined over a time window, limiting the time resolution of polarization change (Fig. 5.9). Nonetheless, the changes in birefringence reported elsewhere (30) of order several milliseconds per km travel path are not observed.

Fig. 5.9 [2 pages] a.) Series of polarization comparison plots for the same 2 earthquakes using analyses windows varying in length from 500 ms (top) down to 2ms (bottom) [see Fig. 2.13 for an explaination of the polarization plots]. b.) An expansion of the 2ms analyses for 1.5 sec about the S-wave train to enhance the temporal resolution (P and S phase arrivals are indicated by P and S respectively). Since window length acts as a high pass filter it can balance the tradeoff between frequency content and discrimination of multiple phase arrivals. The spectral content of the Parkfield microearthquake seismograms varies significantly among stations, so that optimal window lengths are station dependent. Smaller windows improve temporal resolution but remove low frequency energy so that the color display is no longer truly representative polarization as it is defined.

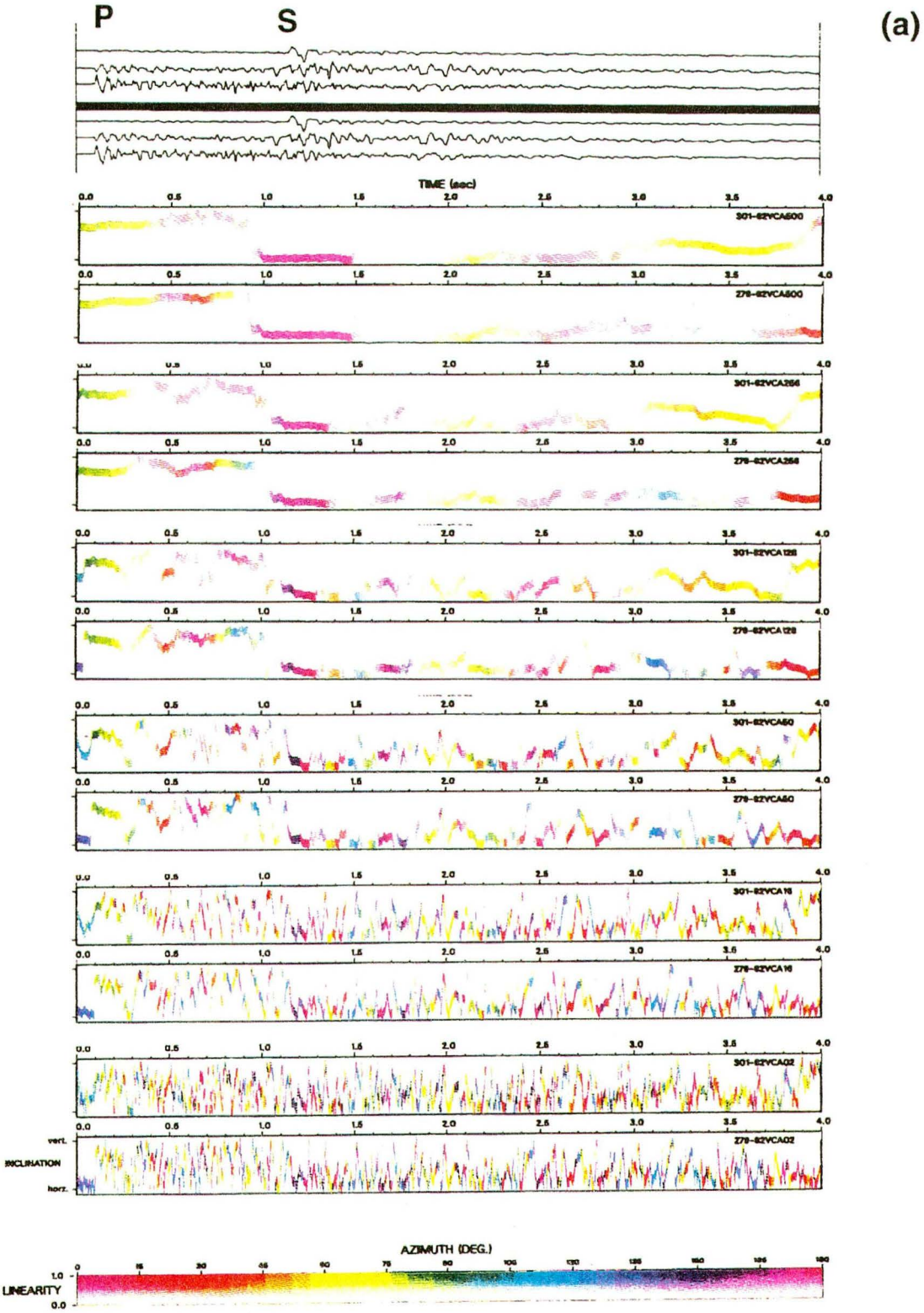
P
S
(a)
TIME (sec)
301-82VCA500
Z78-82VCA500
301-82VCA256
Z78-82VCA256
301-82VCA128
Z78-82VCA128
301-82VCA50
Z78-82VCA50
301-82VCA16
Z78-82VCA16
301-82VCA02
Z78-82VCA02
vert.
INCLINATION
horz.
AZIMUTH (DEG.)
LINEARITY
1.0
0.0

(b)

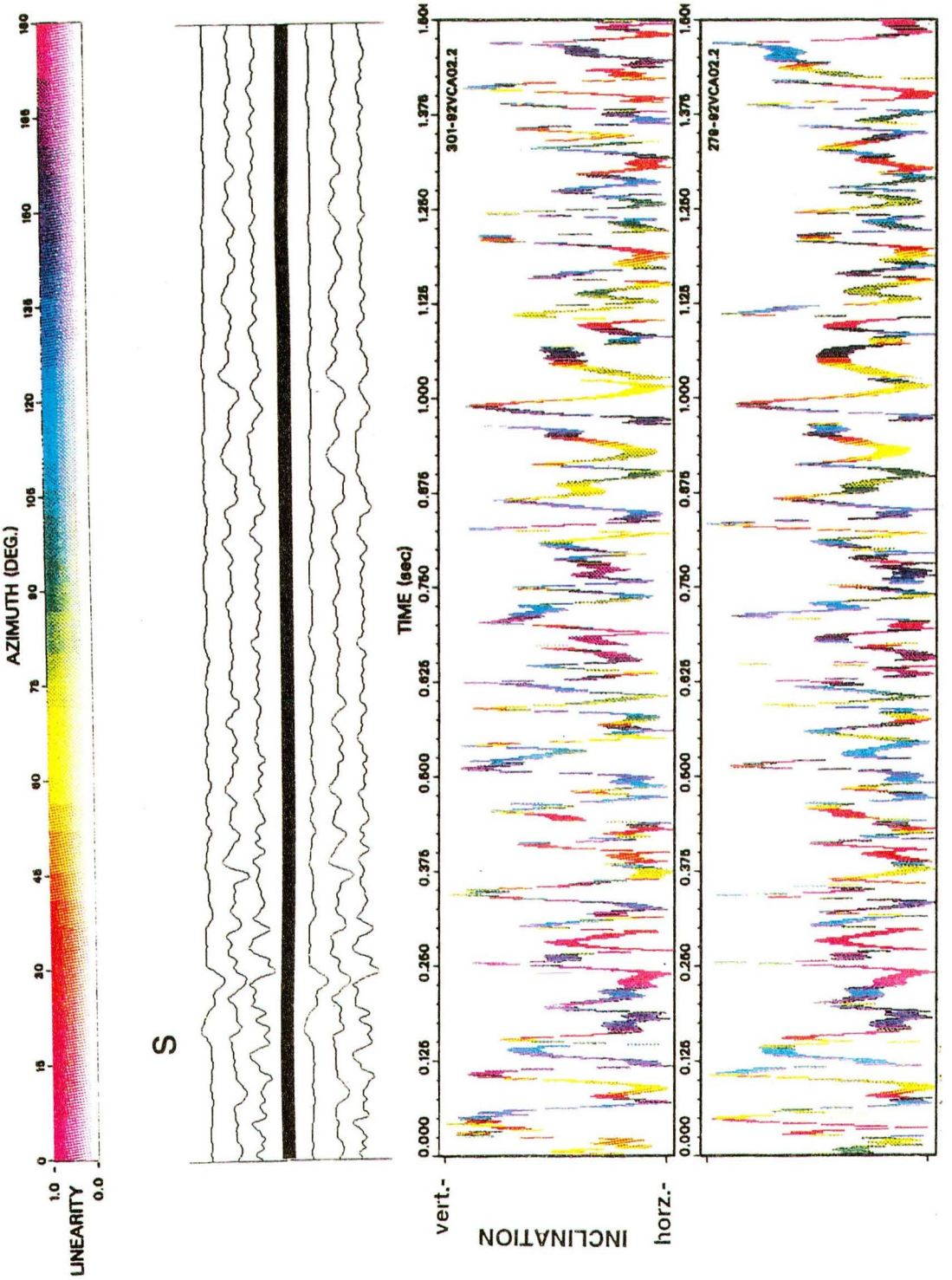
AZIMUTH (DEG.)
0
15
30
45
60
75
90
105
120
135
150
165
180
LINEARITY
1.0
0.0
S
TIME (sec)
0.000
0.125
0.250
0.375
0.500
0.625
0.750
0.875
1.000
1.125
1.250
1.375
1.500
301-92VCA02.2
278-92VCA02.2
vert.-
INCLINATION
horz.-

In conclusion, the 3-D wavefield at Parkfield shows remarkable coherence to very high frequency in its vector linearity attributes and the inherent sensitivity of this property to a multitude of propagation effects indicates that it could be perhaps the most sensitive and complete monitoring tool for wave propagation changes. While the display methodology used here has been developed and shows the potential power of the technique, we have not yet come up with an effective method for detecting and monitoring the subtleties of temporal variation in this complicated domain of vector linearity. No dramatic systematic or transient changes are readily visible in the data as processed for Fig. 5.8c. Further work in this area is necessary and will be pursued.

Δ CODA Q

This Δ coda Q study summarizes recent work done in collaboration with M. Antolik, R. C. Aster, and T. V. McEvilly (12) which applies an established similar event methodology (5) to characteristic microearthquakes at Parkfield recorded from 1987 through 1994 (For a summary of previous studies, see (5) and (14)). Recordings were used from four HRSN stations (Figs. 3.3 and 5.10) close to the epicenter of the 1966, M6 earthquake. Two of these stations (VCA, FRO) are installed in the Tertiary volcanic/Mesozoic granitic Salinian block to the southwest of the San Andreas fault, one (MMN) is located within the fault zone itself, and the fourth station (JCN) is in the Franciscan metamorphic complex to the northeast of the fault. This geometry provides good coverage of the Parkfield nucleation zone, including the region of high V_P/V_S and the Vibroseis anomaly (1). Differences in sub-surface geology between the

station locations significantly affect the high frequency content of the recorded seismograms. The principal objective of this study was to obtain high-resolution (on the order of a few percent) estimates of the time history of Q_C, especially at lower frequencies where most change has been noted in previous studies.

Fig. 5.10 Cross-section along the San Andreas fault showing depth distribution of clusters used in this study (red dots) superposed on the Vp/Vs model (25). Letters designated the clusters listed in Table 1. Background seismicity during the study period is shown by the small black dots. Also shown are the station locations (small triangles) and the 28 June, 1966 earthquake hypocenter (large triangle). Of particular interest is the region of high Vp/Vs ratio above the 1966 hypocenter (12). Taken from Antolik et al. (12).

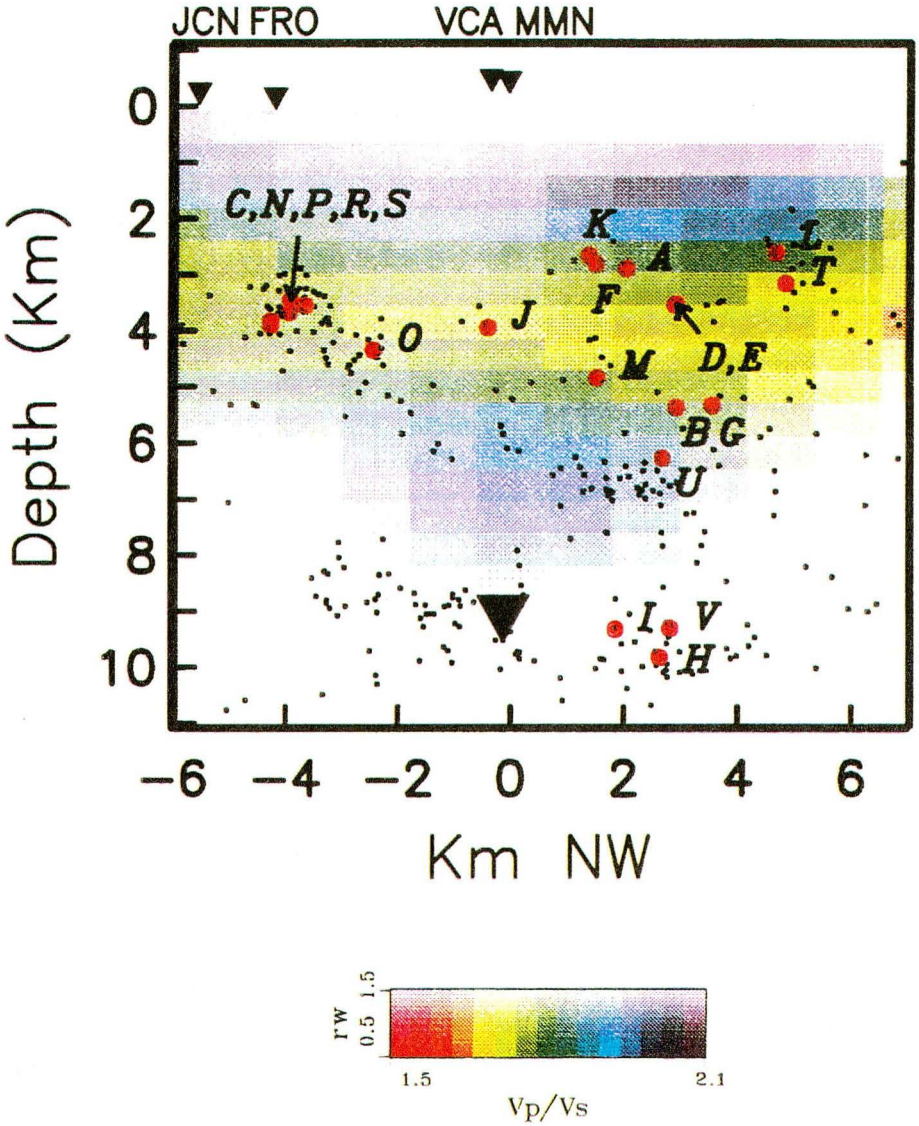
JCN FRO
VCA MMN
Depth (Km)
0
2
4
6
8
10
C,N,P,R,S
K
A
L
T
F
J
O
M
D,E
B
G
U
I
V
H
−6
−4
−2
0
2
4
6
Km NW
rw
0.5
1.5
1.5
2.1
Vp/Vs

Cluster	N_e	Lat (°N)	Lon (°W)	Depth (km)	First (y/d)	Last (y/d)	τ(d)	σ_τ(d)
A	6	35 58.61	120 32.49	3.298	1987/022	1992/352	539	87
B	5	35 57.89	120 31.94	5.363	1987/205	1993/219	441	125
C	5	35 55.26	120 28.73	3.448	1987/264	1992/217	445	102
D	5	35 58.03	120 31.75	3.537	1988/029	1993/124	481	90
E	7	35 58.04	120 31.75	3.527	1988/026	1993/359	360	201
F	6	35 57.52	120 31.06	2.804	1987/163	1993/289	580	383
G	5	35 58.20	120 32.15	5.328	1987/022	1993/349	629	174
H	4	35 57.50	120 32.14	9.815	1988/059	1993/070	612	35
I	4	35 57.19	120 31.79	9.316	1987/280	1993/331	747	297
J	4	35 56.69	120 30.28	3.939	1987/171	1992/329	661	129
K	4	35 57.43	120 31.05	2.653	1987/169	1992/296	651	147
L	5	35 58.59	120 32.72	2.608	1987/147	1993/161	552	316
M	4	35 57.44	120 31.18	4.832	1988/269	1993/192	584	134
N	4	35 55.15	120 28.54	3.829	1987/261	1994/046	586	453
O	5	35 55.82	120 29.45	4.34	1987/162	1993/358	596	191
P	3	35 57.74	120 31.30	3.266	1988/316	1993/164	837	196
R	3	35 55.38	120 28.84	3.544	1987/268	1992/319	939	239
S	4	35 55.14	120 28.56	3.893	1987/263	1994/026	773	207
T	3	35 58.76	120 32.67	3.152	1987/249	1992/206	892	131
U	4	35 57.69	120 31.95	6.259	1987/143	1993/185	745	326
V	3	35 57.59	120.32.20	9.299	1987/031	1992/357	1047	468

Table 1. Similar earthquake clusters used in study of Antolik et. al. (12) (see Fig. 5.10). τ is the mean interevent interval and σ_τ is its standard deviation.

The data set was chosen to span the approximately seven-year analysis period and consists of 21 multiplets of 3-7 events each (Table 1) (Fig. 5.10). Because of the requirement that all seismograms include sufficient coda following twice the S- wave travel time, all clusters are located within about 15 km of the chosen stations (HRSN records are only 12 seconds long). Due to station outages during some periods, not all clusters and events could be analyzed at each station. The resulting improvement in technique resolution introduced by careful source selection is illustrated in Fig. 5.11 for the characteristic event-types discussed in the repeating

characteristic microearthquakes section (this chapter). Fig. 5.11 shows a comparison analysis of ΔQ^{-1} between the event type-3 and type-1 pairs and between event pairs exclusively of event type-1 at station VCA. The amount of scatter in the individual estimates of ΔQ^{-1} using the event type-3/type-1 cluster event pairs is larger by about a factor of 2, particularly in the lower frequency bands. The remaining scatter among the measurements shown in Fig. 5.11b is likely due only to the very small interevent hypocenter separations or rupture histories between event type 1 events or could possibly represent a base noise level artifact inherent in the simplistic coda modeling assumptions.

Fig. 5.11. [2 pages] ΔQ^{-1} versus interevent time separation for event pairs from event types-1 and -3 at station VCA. (a) Pairs involving one member of event type-1 and one from event type-3 (b) Pairs from event type-1 alone. An example pair of seismograms is shown at top for each case. Symbols t_S and $2t_S$ indicate the S-phase pick and the beginning of the data window used in the determination of ΔQ^{-1} respectively. Note the slight differences in the waveforms for the two events in (a), and the resulting increased scatter in the ΔQ^{-1} measurements. From (12).

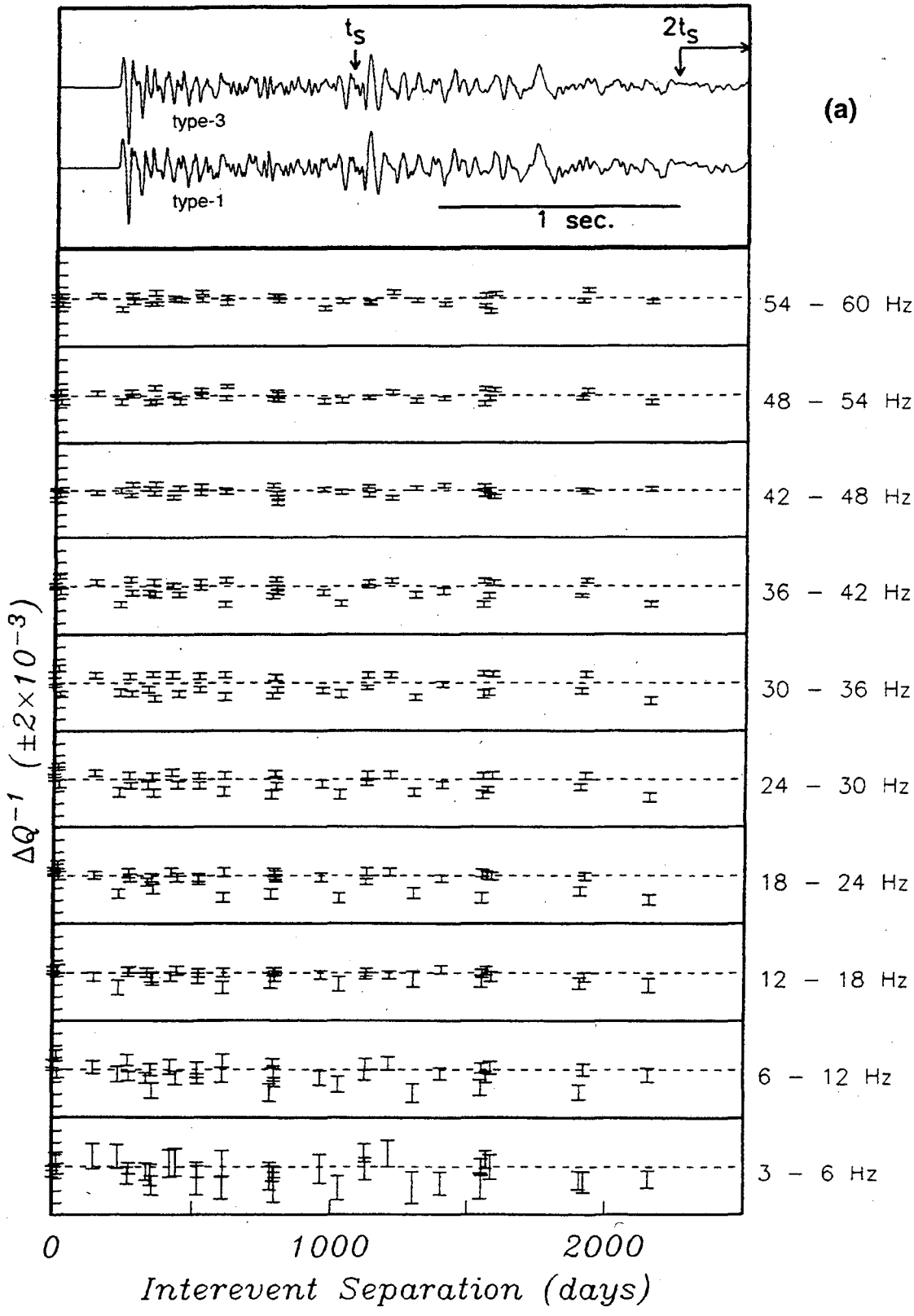
t_S
$2t_S$
type-3
type-1
1 sec.
(a)
54 – 60 Hz
48 – 54 Hz
42 – 48 Hz
36 – 42 Hz
30 – 36 Hz
24 – 30 Hz
18 – 24 Hz
12 – 18 Hz
6 – 12 Hz
3 – 6 Hz
ΔQ^{-1} ($\pm 2 \times 10^{-3}$)
0
1000
2000
Interevent Separation (days)

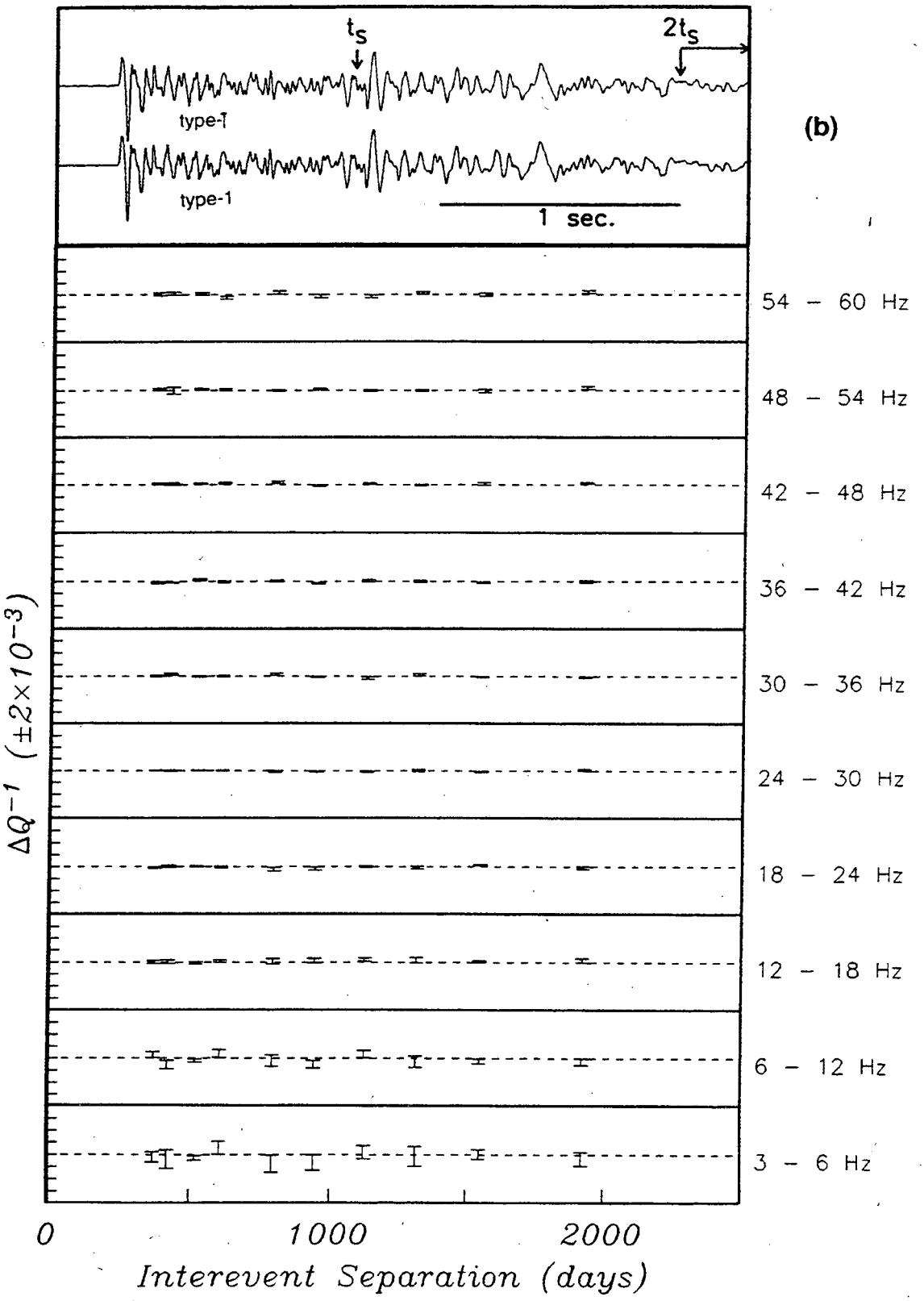
t_S
$2t_S$
type-1
type-1
1 sec.
(b)
54 – 60 Hz
48 – 54 Hz
42 – 48 Hz
36 – 42 Hz
30 – 36 Hz
24 – 30 Hz
18 – 24 Hz
12 – 18 Hz
6 – 12 Hz
3 – 6 Hz
ΔQ^{-1} ($\pm 2 \times 10^{-3}$)
0
1000
2000
Interevent Separation (days)

Discussion:

Due to the high degree of waveform similarity between all events in each cluster good interevent comparison parameters were obtained. Considering these estimates of ΔQ^{-1} as a set of interdependent constraints allows reconstruction of the unknown function $Q^{-1}(t)$ (minus a mean value) sampled at the time of each earthquake (details are given in (12)). Fig. 5.12 shows functional reconstructions for cluster O (Table 1; Fig. 5.10). This cluster incorporates five earthquakes spanning nearly the entire 7-year analysis period. In general, very little variability in Q_C^{-1} is observed at any of the stations. Q_C^{-1} is stable to approximately 2 parts in 10^4 throughout the time period. As each functional reconstruction provides a measure of the time history of Q_C^{-1}, we may search for systematic regional temporal variations in coda Q by combining the results from many individual time series (i.e. clusters) and all the stations (Fig. 5.13a and b). The combined plot for all of the stations and clusters, (Fig. 5.13b), shows that the 95% confidence bound rarely exceeds 30% variation, and is within 10% for the two lowest frequency bands. There is an onset of increased scatter in the measurements about mid-1990 which correlates well with changes beginning around this time in the patterns and rate of microseismicity (19, 20). Another time period of increased scatter begins in late 1992 (around the time of the M = 4.7 event) and continues through most of 1993. This is seen best at MMN and VCA. However, there are no regionally detectable anomalies in Q that are systematically increasing with time, or that could reasonably be interpreted as being precursory to the occurrence of an impending earthquake. We may be seeing effects more complex than simple systematic changes, or

the results of changes in small localized volumes.

This differential analysis (12) of the frequency-dependent coda decay, with conservative error estimates, showed that Q has been stable. The mean value of Q has not changed by more than about 5% at the 68% confidence level during the entire time interval in the frequency range 3-30 Hz, although the allowable variation can exceed 30% at the 95% level some frequency bands, particularly at higher frequencies where the reference values of Q are significantly greater. The reconstructed Q^{-1} time series are consistent with a zero change hypothesis. As these stability values for Q are derived using reference values appropriate for the relatively competent Salinian block SW of the fault, they are likely to be upper bounds, as the mapping of the measured parameter, ΔQ^{-1}, to ΔQ becomes increasingly sensitive when larger reference values of Q are used.

Although the short coda length available on these records (4-6 sec for most frequency bands) prevents even greater accuracy from being achieved in the determination of differential coda properties, it also limits the single-scattering coda footprint to sensing only the region in and immediately surrounding (within about 20 km) the presumed nucleation zone of the next Parkfield earthquake. Selecting the most highly similar sources for this type of high-precision temporal monitoring of the scattered wavefield was critical to achieving this level of resolution in differential Q measurements. In addition, the study confirmed the concern of earlier studies (5, 7, 15) that even small differences in source characteristics can

cause a significant degradation of parameter repeatability, even for events with hypocenter separations of as little as 10-20 m and with main phase maximum cross-correlations of > 0.98.

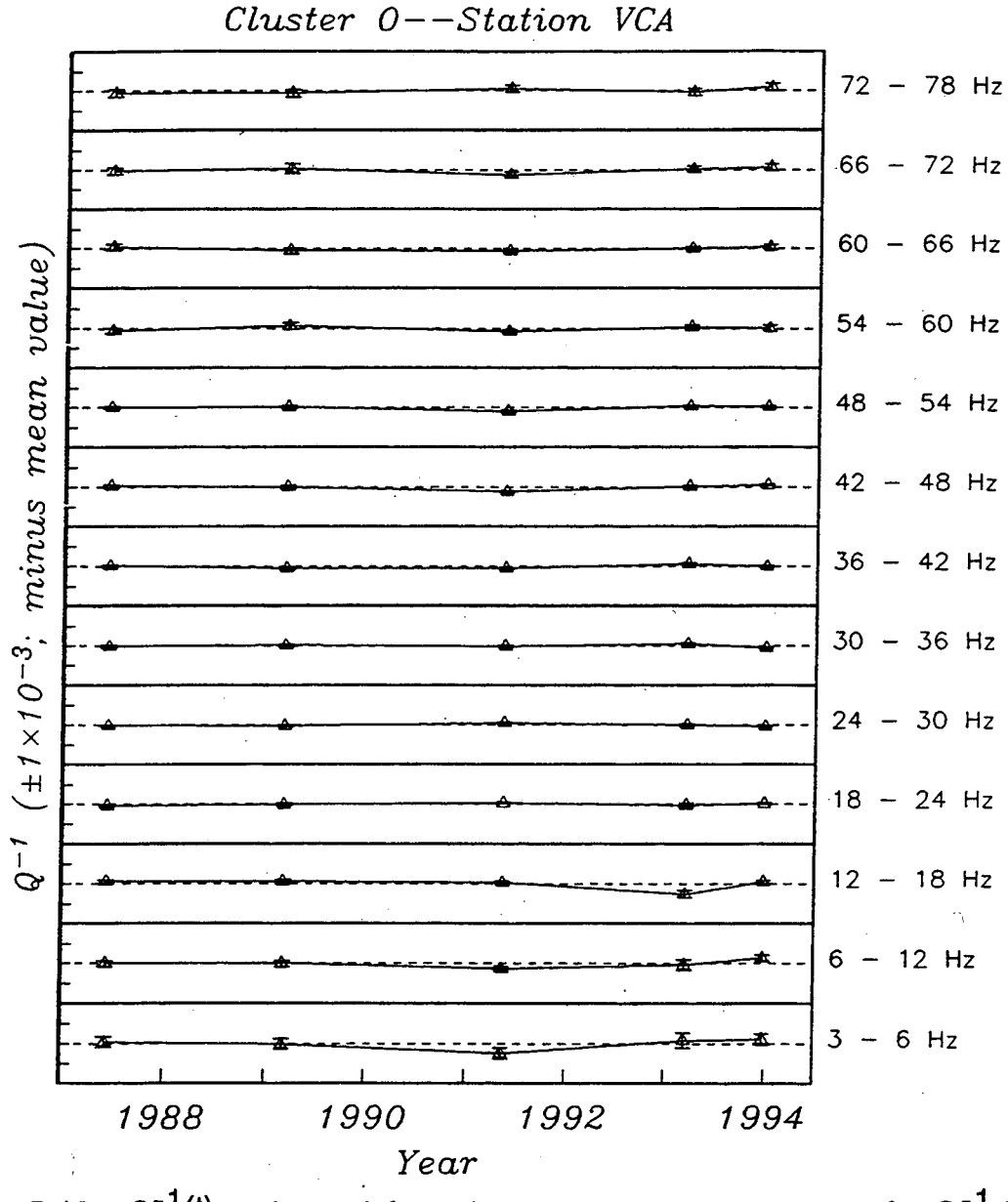

Fig. 5.12. $Q^{-1}(t)$ estimated from interevent measurements of ΔQ^{-1} in cluster O for Station VCA. The error bars for each point reflect two standard deviations. From (12).

Fig. 5.13 [2 pages] Q as a function of time obtained from combining functional reconstructions (e.g., Fig. 5.12) from all observed clusters. The mean value of Q is shown as the dashed line. Solid lines indicate 68% and 95% confidence bounds for deviations from the mean. Time points from individual function reconstructions are shown along with corresponding 1 error bars. Indicated at right are references values for Q (12) in each frequency band used to translate variation in ΔQ^{-1} into variation in Q. (a) VCA. (b) All stations. From (12).

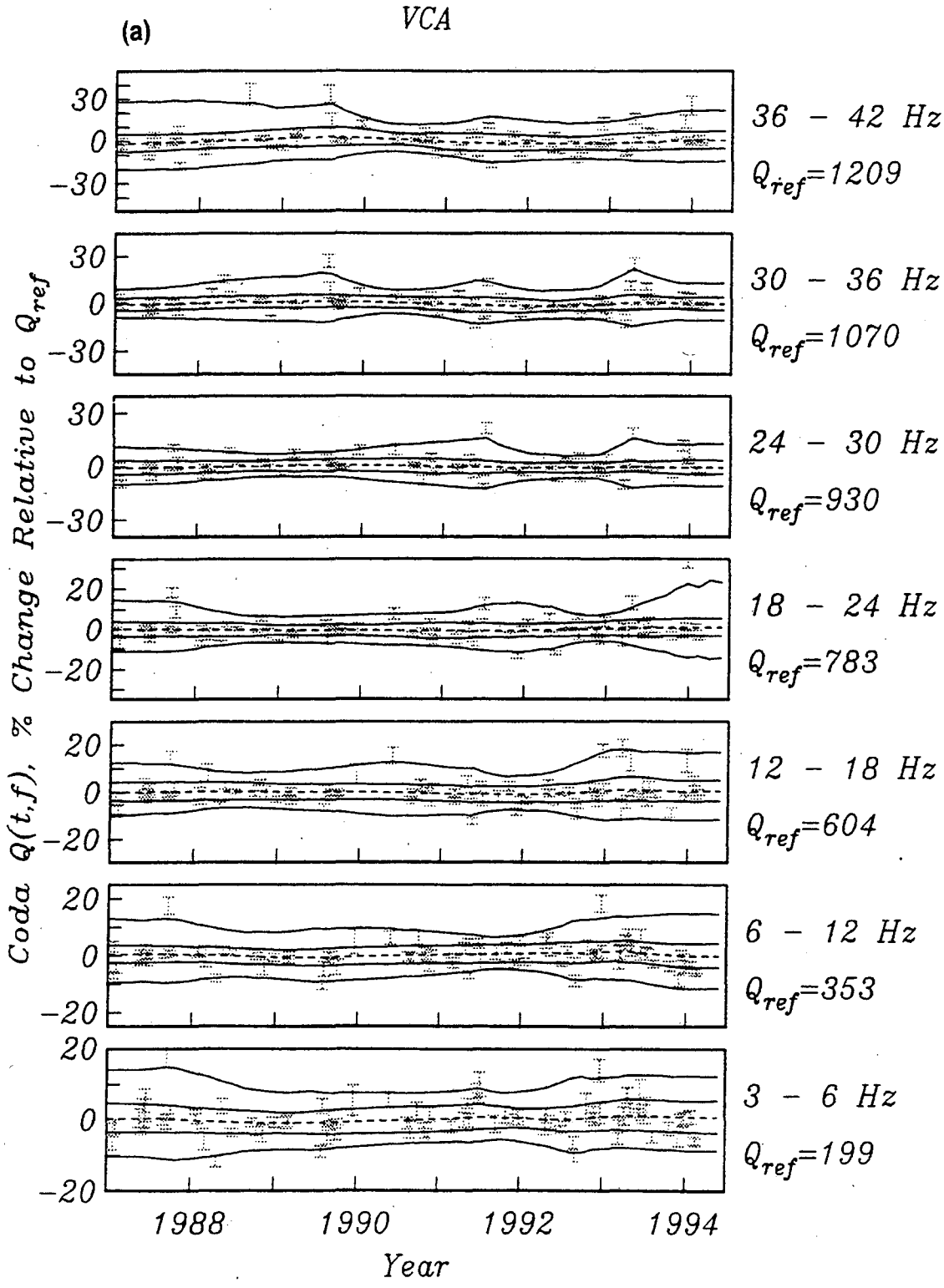
(a)
VCA
36 - 42 Hz
Q_{ref}=1209
30 - 36 Hz
Q_{ref}=1070
24 - 30 Hz
Q_{ref}=930
18 - 24 Hz
Q_{ref}=783
12 - 18 Hz
Q_{ref}=604
6 - 12 Hz
Q_{ref}=353
3 - 6 Hz
Q_{ref}=199
Coda Q(t,f), % Change Relative to Q_{ref}
Year
1988
1990
1992
1994

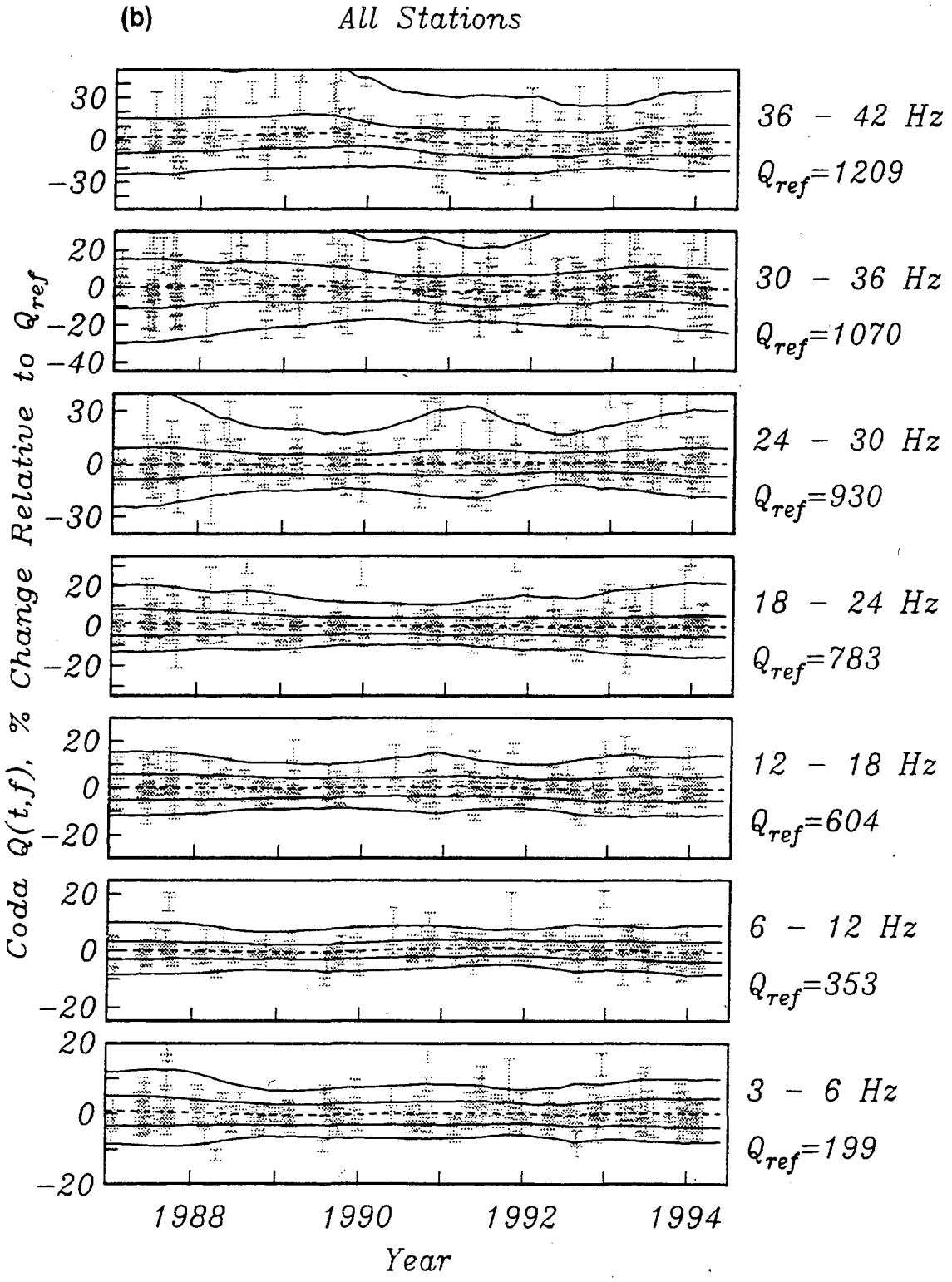
(b)
All Stations
36 - 42 Hz
Q_{ref}=1209
30 - 36 Hz
Q_{ref}=1070
24 - 30 Hz
Q_{ref}=930
18 - 24 Hz
Q_{ref}=783
12 - 18 Hz
Q_{ref}=604
6 - 12 Hz
Q_{ref}=353
3 - 6 Hz
Q_{ref}=199
Coda Q(t,f), % Change Relative to Q_{ref}
30
0
-30
20
0
-20
-40
1988
1990
1992
1994
Year

CONCLUSION

It is clear that microearthquake cluster sources and, especially, characteristic microearthquake sequences show much promise for monitoring temporal change in medium wave-propagation properties at previously unequaled resolution. Equally promising is the potential use of seismicity and cluster occurrence and recurrence patterns for monitoring change in the nucleation region, and the use of recurrence statistics from forecasting and prediction methodology to infer changes in slip rate at depth.

To date observations of changes in wave-propagation parameters of travel-time, polarizations and Δcoda Q show only small to insignificant changes, in the same region but smaller than those seen in the Vibroseis monitoring study at Parkfield. However as seen in Fig. 51a-f, intrinsic uncertainty, σ_I, has increased and average recurrence intervals, μ_D, have decreased with time presumably in response to the recent increase in M4+ earthquake activity and perhaps the approach of the expected M6 event. We also note a difference in σ_I and its rate of change as a function of depth and proximity to the M6 asperity. Furthermore, σ_I appears to be smaller in areas of less concentrated seismicity. These observations suggest that regularity in recurrence-times are significantly influenced by both inter-cluster triggering and variations in cluster locations in depth and along strike.

These observations suggest two things. First, the apparent sensitivity of μ_D and σ_I to changing conditions in the fault zone could make them useful

parameters for monitoring fault-zone process. Second, the temporal variability of the recurrence statistics would suggest greater uncertainty in currently used prediction models if, as suggested in chapter IV, the recurrence behavior of characteristic microearthquakes scales to large damaging events. The

systematics of the variability with time, however, may suggest a way to partially compensate for this non-stationarity.

The increase in average size, rate, and depth of seismicity and the non-stationary rate of characteristic recurrence, intra-cluster occurrence and recurrence patterns, decreasing B-values, decreasing proportion of clustered to non-clustered activity, slip at depth and increased M4+ activity within the last 2-3 years strongly suggest that the dynamic process in the Parkfield asperity has changed. It would be most satisfying if we are actually seeing a deterioration of the Parkfield Asperity, in a long-sought demonstration of precursory behavior to the expected M6 event there.

REFERENCES

1. E. Karageorgi, R. Clymer, T. V. McEvilly, Bull. Seismol. Soc. Am. 82, 1388 (1992).

2. T. V. McEvilly and L. R. Johnson, ibid. 64, 343 (1974).

3. M. Hellweg, P. Spudich, J. B. Fletcher, L. M. Baker, J. Geophys. Res. (in press) (1995).

4. J. S. Haase, P. M. Shearer, R. C. Aster, Bull. Seismol. Soc. Am. 85, 194 (1995).

5. R. C. Aster, G. Slad, J. Henton, ibid. (in press).

6. D. D. Jackson and Y. Y. Kagan, EOS 76, S199 (1995).

7. J. Got and J. Frechet, Geophys. J. Int. 114, 325 (1993).

8. W. H. Bakun, R. Stewart, C. Bufe, Bull. Seismol. Soc. Am. 68, 1253 (1978).

9. K. Mogi, Pageoph. 117, 1172 (1979); K. Mogi, Earthquake Prediction, an International Review. Ewing Ser. 4, 43 (1981); K. Mogi, J. Seismol. Soc. Japan (2) 35, 145 (1982).

10. S. Crampin and R. Evans, Geophys. J. R. astr. Soc. 76, 147 (1984).

11. S. Blakeslee and P. Malin, Bull. Seism. Soc. Am. 81,332 (1991).

12. M. Antolik, R. M. Nadeau, R. C. Aster, T. V. McEvilly, ibid. (in press) (1995).

13. R. Aster and P. Shearer, ibid. 81, 1081 (1991).

14. M. Wyss et al., Evaluation of Proposed Earthquake precursors, AGU special publication, Washington, C. C., 94 (1991).

15. J. Got, G. Poupinet, J. Frechet, Pageoph. 134, 195 (1990).

16. K. Aki and B. Chouet, J. Geophys. Res. 80, 3322 (1975).

17. S. Blakeslee, P. Malin, M. Alvarez, Geophys. Res. Lett. 16, 332 (1989).

18. Y-G. Li, P. Leary, Bull. Seism. Soc. Am. 80, 1254 (1990); Y. Ben-Zion and P. Malin, Science 251, 1592 (1991).

19. P. Malin and M. Alvarez, Science 256,1005 (1992).

20. R. M. Nadeau, W. Foxall, T. V. McEvilly, Science 267, 503 (1995).

21. A. Nur, Bull. Seismol. Soc. Am. 62,1217 (1972); A. Nur, Geology 2, 217 (1974).

22. C. H. Scholz, Pageoph. 126, 701 (1988).

23. C. H. Scholz, L. R. Sykes, Y. P. Aggarwal, Science 181, 803 (1973); J. H. Whitcomb, J. D. Garmony, D. L. Anderson, Science 180, 632 (1973).

24. E. Karageorgi, T. V. McEvilly, Bull. Seismol. Soc. Am (in preparation).

25. A. Michelini and T. V. McEvilly, Bull. Seismol. Soc. Am. 81, 524 (1991).

26. T. M. Daley and T. V. McEvilly, ibid. 80, 857 (1990).

27. S. Crampin, R. Evans, B. K. Atkinson, Geophys. J. T. astr. Soc. 76, 147 (1984).

28. D. Winterstien, Geophysics: The Leading Edge of Exploration, Sept., 21 (1992).

29. Y-G Li, K. Aki, D. Adams, A. Hasemi, W. H. K. Lee, J. Geophys. Res. 99, 11705 (1994).

30. Y. Liu and S. Crampin, Seismol. Res. Lett. 63, 76 (1992).

31. S. Crampin, D. C. Booth, R. Evans, S. Peacock, J. Fletcher, J. Geophys. Res. (in press) (1990).

32. R. C. Aster, P. M. Shearer, J. Berger, J. Geophys. Res. 95, 12449 (1990).

33. National Earthquake Prediction Evaluation Council Working Group, U. S. Geol. Surv. Circ. 1116 (1994).

34. Review Meeting of Parkfield Data, July 1994-December 1994 plus Review from 1985, internal circulation.

35. D. P. Schwartz and K. J. Coppersmith, J. Geophys. Res. 89, 5681 (1984).

36. M.-J. Fremont and S. D. Malone, J. Geophys. Res. 92, 10223 (1987).

37. G. Poupinet, W. L. Ellsworth, J. Frechet, J. Geophys. Res. 89, 5719 (1984).

CHAPTER VI

Summary, Recommendations and Conclusions

SUMMARY

It was the intent of this dissertation to demonstrate the potential of microearthquake clusters for resolving many issues in earthquake seismology. Generally microearthquakes are treated differently from large earthquakes because their small size makes it impossible to observe directly important source parameters, or to estimate confidently these parameters from recorded seismograms. Furthermore, the large uncertainty in microearthquake locations relative to their rupture dimensions makes it difficult to observe detailed patterns in the microseismicity. As a result, many of the characteristics of microearthquakes at meter scale remain a mystery.

To help overcome these limitations, the high-resolution seismic network at Parkfield was installed and has been recording highly discriminating and temporally stable seismograms since 1987. These high-quality recordings allow for the application of high-resolution location and waveform analysis methods, and their use on Parkfield microearthquakes has yielded new and detailed observations which have important implications for seismology and processes underway in active, seismogenic fault zones.

The characterization of waveform similarity and the determination of precise relative locations show that the microseismicity is localized at

some 300 sites (or clusters) having about 20m dimensions and which cumulatively occupy less than 1% of the area within the seismogenic zone. The distribution of recurrence intervals between events in clusters is bimodal with a short interval mode peaked at less than 2 minutes and falling off as the inverse of the recurrence-time and a lognormal mode distributed about an average recurrence interval of 0.8 year.

Detailed analyses of the high resolution seismograms frequently show systematic differences between groups of events within clusters (i.e. subclustering) which relate to the bimodality of the recurrence-interval distribution. Within subcluster groups, events are essentially characteristic -- earthquakes with nearly identical size, locations, waveforms, and frequently with quasi-periodic recurrence -- and their recurrence-time distributions essentially define the lognormal mode. Events within clusters but belonging to different subclusters tend to occur sympathetically so that their separations in occurrence time are short and define the mode of 1/t decay.

The characteristic subcluster sequences are widely distributed and can serve as repeating illumination sources for monitoring changes in wave-propagation characteristics with a resolution and spatio-temporal coverage previously unattainable. The cluster and characteristic subcluster phenomena also provide a secondary monitoring technique through their patterns of occurrence and recurrence. These patterns often show systematic variations which complement observations of change in seismicity rates and frequency-size distributions. Furthermore, the

changes in average recurrence intervals of characteristic sequences can be used to estimate local changes in slip rates at depth, and variations of 10-20% are inferred.

The characteristic recurrence of events within subclusters and the 1/t decay of triggered seismicity among subclusters mimics the foreshock, aftershock and characteristic behavior of large damaging events and their recurrence-times appear to scale with seismic moment. This scaling suggests that the physics responsible for recurring microearthquake activity is not fundamentally different from that of larger repeating events, and that the behavior of large damaging earthquakes might be more easily understood by studying the more common small earthquakes which have shorter average recurrence times. In addition, by assuming a balance between long term cumulative seismic slip and cumulative strain loading, many previously unresolved microearthquake source parameters can be estimated. Comparison of these estimates with values from larger events leads to an unconventional interpretation of the physics of earthquakes (e.g., size-dependent stress drops) that explains puzzling observations of microearthquakes such as unusually high source corner frequencies, near collocation of adjacent rupture, and anomalously long recurrence intervals. This scaling suggests neither the L nor W relation of slip to fault length is generally correct, and that frequency-size statistics are dependent on the catalogue duration, and on non-stationary effects in either seismicity rates or the fraction of repeating to non-repeating events.

RECOMMENDATIONS

Many specific findings reported in this work are new and require more comprehensive analyses for confirmation and exploitation. It seems particularly worthwhile to continue exploring the microearthquake clustering phenomenon. Future work needs to focus on refining existing analysis techniques, grooming and standardizing the Parkfield and other potentially usable microearthquake data sets, and on designing studies to answer specific outstanding questions.

To achieve these goals, I recommend further automation of the relative location and relative moment determination methods and cluster and subcluster identification techniques. This will allow researchers to take better advantage of the large population of events and event sequences which continue to grow at Parkfield and elsewhere. Recasting the relative locations in terms of S-P inversion and using automation and location stacking should overcome problems with asynchronous timing and increase spatial resolution from 5-10m to ~1 meter. As our past practice at Berkeley has been to use consistent station sets in the relative location process, an algorithm needs to be devised to correct for heterogeneity in station coverage while retaining the method's precision. With these improvements and by extending the relative location method to nearby clusters we should be able to get a better resolved picture of event interactions. Incorporation of the surface strain data collected at Parkfield with observations of seismicity and slip rates of characteristic sequences are also needed, as are refinements to moment tensor inversion schemes to help provide consistent information on the orientations of the rupture

planes, earthquake size and other source parameters.

Two improvements in the data archive are also recommended to help realize the full potential of the microearthquake data set. First, events missing due to the early practice of overwriting same minute earthquakes need to be recovered from the original field tapes. Second, many of the events in 1992-1993 have serious waveform wrap around at clipping due conversion from 4-byte to 2-byte integers and these should be corrected.

Near-term studies should focus on two main topics. First, the methods used to assess temporal change in travel time and polarizations need to be applied on a more complete data set (tens of clusters comprised of hundreds of characteristic events). Several investigations are natural extensions of this work: tomographic imaging of travel time change; a depth section of along-strike polarization; methods for discriminating fault-zone guided-waves from slow S-waves; and changes in patterns of intra-cluster occurrence.

Second, work needs to focus on rigorous delineation of the scaling relationships outlined in chapter IV and on exploring the implications with in stress drop, rupture area and other pertinent source parameters in order to justify the further treatment of microearthquakes as a time-collapsed, small-scale version of large damaging earthquakes and their sequences. If successful, many aspects of microearthquake behavior could be projected to the large earthquake scale for testing of existing occurrence and prediction models and to better understand the complex processes of

large earthquake nucleation, with implications for seismic hazards.

CONCLUSIONS

In this dissertation I have presented an early look at the localized nature of the microearthquake process at Parkfield , its characteristic and triggered-seismicity behavior, its scaling to large damaging events, and the implications this scaling has for source and fault-zone dynamic models. I have also shown how the scaling of patterns of recurrence and triggered seismicity can be used to test and refine models of earthquake frequency-size scaling and earthquake prediction. I have presented monitoring results which benefit greatly from the features of characteristic recurrence, and I have introduced the concept of recurrence- and occurrence-pattern behavior into the seismic monitoring arsenal. These studies illustrate the enormous potential for deeper seismological understanding in microearthquakes recorded by high-resolution networks and analyzed with modern techniques.

LAWRENCE BERKELEY NATIONAL LABORATORY
UNIVERSITY OF CALIFORNIA
TECHNICAL & ELECTRONIC INFORMATION DEPARTMENT
BERKELEY, CALIFORNIA 94720